

**Investigating fs/ps CARS for Quantifying Pressure in Reacting Flow
Environments**

by

Mohamed Anwar Akkari

A thesis submitted in partial fulfillment of the
requirements for the degree of

Master of Science
in
Mechanical and Aerospace Engineering

Thesis Committee:
Dr. Harsha Chelliah, Chair
Dr. Chloe Dedic
Dr. Thomas Ward

University of Virginia
December 2023

Abstract

Femtosecond/picosecond coherent anti-Stokes Raman scattering (fs/ps CARS) was investigated for quantifying in-stream pressure fluctuations in reacting flows. Accurate quantification of pressure fluctuations can provide insight into coupling between flow kinetic energy and molecular internal energy for high-speed reacting flows. For the current work, ro-vibrational (Q-branch) fs/ps CARS was investigated to optimize pressure sensitivity.

This study addresses two primary challenges. First, improvements to the CARS spectral model were made to accommodate the effects of various collisional partners. Experimental results from literature over a broad range of gas temperatures were used to refine the Modified Exponential Gap (MEG) model. Second, the impact of experimental uncertainties including laser bandwidth and stability were investigated by exploring the fs/ps CARS response at controlled pressures. Experimental measurements were conducted in a static pressure cell containing controlled gas mixtures (N_2 , O_2 , CH_4 , and CO_2). The pressure and species dependence of the fs/ps CARS response for various gas mixtures was investigated and reported. Various features in the measured fs/ps Q-branch CARS spectra for N_2 and CO_2 and N_2 and CH_4 are used to deduce an empirical pressure dependence. The recorded fs/ps Q-branch CARS spectra for N_2 and O_2 were compared to spectral simula-

tions. A simple spectral analysis technique was introduced to mitigate the impact of excitation variability. This approach was validated across various N_2/O_2 mixtures and holds promise as a foundational method for pressure measurements in dynamic combustion environments.

*Dedicated to my parents, my family, and a unified Ummah,
with hopes for brighter days ahead.*

*“And whoever is an ally of Allāh and His Messenger and those who have believed
- indeed, the party of Allāh - they will be the predominant.”*

(Al-Quran, Surah Al-Maidah: Verse 56)

*“But seek, through that which Allāh has given you, the home of the Hereafter;
and [yet], do not forget your share of the world. And do good as Allāh has done
good to you. And desire not corruption in the land. Indeed, Allāh does not like
corrupters.”*

(Al-Quran, Surah Al-Qasas: Verse 77)

*“I would rather have questions that can't be answered than answers that can't be
questioned.”*

Dr. Richard P. Feynman

Acknowledgments

As I contemplate the conclusion of my academic journey, a myriad of emotions—satisfaction, hope, and a tinge of wistful joy—surrounds me. Foremost, I extend my heartfelt gratitude to God, the guiding force that has remained a constant presence during this challenging yet deeply rewarding pursuit. My family has consistently provided unwavering support as I navigated difficult life choices. I am particularly appreciative of my mother, whose belief in me provided the impetus for my journey from a rural village in Tunisia to Yale University. Throughout my undergraduate studies, I gained early exposure to scientific research, laying the foundation for fruitful work during my graduate career at the University of Virginia. I am gratified that I could fulfill my childhood dream of delving into scientific investigation, particularly in the realm of advanced physics. This experience has not only shaped my academic trajectory but has also instilled in me a profound sense of resilience and determination.

A special appreciation goes to my advisor, Dr. Chloe Dedic. Being a part of her lab was a privilege that allowed me to contribute in a small part to the scientific advancement of this burgeoning field. I am sincerely grateful for your support in navigating experimental intricacies, engaging in theoretical discussions, and benefiting from your brilliant mind. Your words of encouragement during

challenging times resonate deeply, and I eagerly anticipate the prospect of crossing paths again, perhaps to extend the work I have initiated.

Finally, I would like to express my gratitude to Zach Morris and Ryan Thompson for their invaluable support during the data collection process. Additionally, I am thankful to the members of the Aerospace Research Laboratory and Reacting Flow Laboratory for their assistance, no matter how minor. To everyone, your support will be remembered.

Table of Contents

Abstract	i
Dedication	iii
Acknowledgments	v
List of Tables	x
List of Figures	xi
1 Introduction	1
1.1 Motivation	1
1.2 Quantifying pressure for high-speed flows: Traditional Techniques	3
1.2.1 Pitot Tubes	3
1.2.2 Pressure Transducers	4
1.3 Quantifying pressure for high-speed flows: Optical Techniques	5
1.3.1 Unsteady Pressure Sensitive Paint (uPSP)	6
1.3.2 Filtered Rayleigh scattering (FRS)	7
1.3.3 Laser-induced Fluorescence (LIF)	8
1.3.4 Interferometry	9
1.3.5 Tunable Diode Laser-Absorption Spectroscopy (TDLAS)	10
1.4 Using Coherent anti-Stokes Raman Scattering (CARS) for Quantifying Pressure in high-speed flow	11
1.4.1 Frequency Domain CARS	12
1.4.2 Time Domain Hybrid fs/ps CARS	12
1.5 Research Objectives	17
1.6 Thesis Outline	18

2	Theoretical and Experimental Approach	19
2.1	Hybrid fs/ps CARS	19
2.2	SHBC Design	23
2.3	Experimental Setup	26
2.3.1	Optical Layout	26
2.3.2	High-Pressure Gas Cell	28
2.4	CARS Spectral Modeling	29
2.5	Collisional Line Broadening and Linewidth Models	32
2.5.1	Modeling Overview	34
2.5.2	Modified Exponential Gap (MEG) Model	35
2.6	Pressure Broadening	37
2.7	Proposed Dual-Probe CARS Setup	38
2.8	Chapter Summary	41
3	Impact of Gas Pressure on Q-branch fs/ps CARS	42
3.1	Expanding the Collisional Linewidth Model for fs/ps CARS Simulations	42
3.1.1	N ₂ -N ₂	43
3.1.2	O ₂ -O ₂	55
3.1.3	N ₂ -O ₂	59
3.1.4	N ₂ -H ₂	62
3.1.5	Total N ₂ Collisional Linewidths	65
3.2	Ro-vibrational fs/ps CARS Sensitivity to Pressure and Species Concentration	66
3.3	fs/ps CARS Simulations Across a 1D Flame	72
3.4	Chapter Summary	73
4	Experimental Characterization of Q-branch fs/ps CARS at Elevated Pressures	75
4.1	Experimental Considerations	75
4.1.1	Measurement Resolution	75
4.1.2	Signal Attenuation	77

4.2	Experimental Approach	79
4.2.1	Pressure Sensitivity: Probe Delay Discussion	80
4.2.2	Signal Intensity: Raman Dephasing Discussion	80
4.3	Results: Spectral Analysis Considerations	85
4.3.1	Background Correction	85
4.3.2	Shot-to-Shot Fluctuations in Raman Excitation	87
4.3.3	Excitation Variation at Elevated Pressures	90
4.4	Results: N ₂ -O ₂ Gas Mixtures	94
4.5	Results: N ₂ -CH ₄ Gas Mixtures	101
4.6	Results: N ₂ -CO ₂ Gas Mixtures	102
4.7	Chapter Summary	106
5	Conclusions	107
5.1	Summary	107
5.2	Future Work	110
	Bibliography	112

List of Tables

2.1	Raman shifts of the various species of interest	20
2.2	Spontaneous Raman scattering parameters of relevant crystals	39
2.3	KGW output wavelengths	40
3.1	N ₂ -N ₂ linewidth datasets used in this work	45
3.2	MEG-PF model parameters summary for N ₂ -N ₂ collisions	54
3.3	O ₂ -O ₂ linewidth datasets used in this work	56
3.4	MEG model parameters summary for O ₂ -O ₂ collisions	58
3.5	N ₂ -O ₂ linewidth datasets used in this work	60
3.6	MEG model parameters summary for N ₂ -O ₂ collisions ($a = 1.5$)	62
3.7	N ₂ -H ₂ linewidth datasets used in this work	63
4.1	List of excitation parameters tested for a given set of probe parameters	97

List of Figures

1.1	Mirage III right-side profile displaying Pitot tube [1]	3
1.2	Detail of transducer section in a high-pressure shock tube showing PCB-113A23 piezoelectric pressure transducers [2]	5
1.3	Pressure Sensitive Paint (PSP) fundamental principle [3]	6
1.4	FRS geometry for a gas jet experiment implemented by Doll <i>et. al</i> [4]	7
1.5	Experimental setup for supersonic jet presented by Chang <i>et. al</i> [5]	8
1.6	Schematic of the TCF based MZI used in the experimental setup presented by Li <i>et al.</i> [6]	9
1.7	Experimental set up of the TDLAS presented by Jousten <i>et al.</i> [7] .	10
1.8	CARSFIT spectra presented by Woodmansee <i>et. al</i> at $p = 0.97$ atm (a) and $p = 0.1$ atm (b) [8]	12
1.9	Calculated decay of the spectrally integrated fs/ps rotational CARS signal by Kearney and Danehy [9]	13
1.10	Simulated CARS spectra for a Mach 2.7 nozzle at 90 torr (black solid line) and 76 torr (green dashed line) by Dedic <i>et. al</i> [10]	14
1.11	Sample Single-Shot CARS Fits within a Supersonic-Coaxial Jet. Temperature Measured (left) and pressure Measured (right)	15
1.12	Comparison of (a) VCARS Pressure Sensitivity and (b) RCARS (by Dedic <i>et. al</i> [10])	16
2.1	CARS phase-matching scheme	20
2.2	Timing diagram for fs/ps CARS.	21

2.3	Excitation profile: $\lambda_{pump} = 670$ nm, $\lambda_{Stokes} = 800$ nm @ $p_{Ar} \sim 1$ bar	22
2.4	Broadband energy-level CARS diagrams for N ₂ , O ₂ , CO ₂ and CH ₄ .	23
2.5	SHBC optical layout	25
2.6	Experimentally measured SHBC probe profile with a Gaussian fit .	26
2.7	Experimental schematic of hybrid fs/ps CARS system in pressure cell. WP: waveplate, SHG: second-harmonic-generation crystal, BS: beamsplitter, EMCCD: electron-multiplied charge-coupled device camera.	27
2.8	Pressure cell 3D view and flange cross section	28
3.1	Initial MEG model parameter optimization (α , β , δ , and m) with fixed: $n = -0.5$, $a = 1.5$, and $T_0 = 295$ K	47
3.2	Optimized β , with the rest of the parameters fixed	48
3.3	Examples of MEG-PF linewidth fits at cold and ambient temperatures	50
3.4	Examples of MEG-PF linewidth fits at mid-range temperatures . .	51
3.5	Examples of MEG-PF linewidth fits at elevated temperatures . . .	52
3.6	Disagreement between experimental data and MEG-PF in a sample of linewidth datasets	53
3.7	List of MEG parameters and the associated disagreement between experimental data and MEG model for the entire compilation of datasets	54
3.8	Disagreement plot comparison between fixed a vs. floating a in the NLSQ optimization	57
3.9	MEG linewidth fits for Hölzer <i>et al.</i> and Miller <i>et al.</i> measurements ($a = 1.67$)	59
3.10	List of MEG parameters and the associated errors for the full dataset	61
3.11	MEG linewidth fits for the full dataset	61

3.12	List of MEG parameters and the associated disagreement using Bohlin <i>et al.</i> measurements	64
3.13	MEG linewidth fits for Bohlin <i>et al.</i> measurements	65
3.14	Vibrational Q-branch of N_2 and O_2 Raman spectra simulated at a sample of low- and high-pressures (a: at $\tau = 5$ ps — b: at $\tau = 45$ ps)	67
3.15	VCARS summed peak ratio ($\frac{I_{O_2}}{I_{N_2}}$) vs. pressure and probe delay for a constant N_2 - O_2 mixture at $T = 295$ K	68
3.16	Variation of relative intensity CARS signal ($\frac{I_{O_2}}{I_{N_2}}$) for a probe delay sample (5, 20, 30, 45 and 90 ps)	69
3.17	VCARS summed peak ratio variation ($\frac{I_{O_2}}{I_{N_2}}$) vs. pressure and probe delay for a constant N_2 - O_2 mixture at $T = 1100$ K	70
3.18	$\frac{I_{O_2}}{I_{N_2}}$ variation for a selection of N_2 - O_2 compositions	71
3.19	Vibrational CARS Raman Spectra of N_2 and O_2 at Various Locations in a Quasi One-Dimensional CH_4 /Air Diffusion Flame at $p = 2.5$ atm	73
4.1	Raman Q-Branch N_2 spectra measured at variable λ_0	76
4.2	Calculated Experimental Resolutions	76
4.3	Measured ND Filter Transmission Centered at $\lambda = 375$ nm	78
4.4	Excitation Intensity Variation at Variable ϕ TFP Adjustment	79
4.5	Experimentally-measured time-dependent response of fs/ps CARS for air	81
4.6	Experimentally-measured time-dependent response of fs/ps CARS for a N_2 - CH_4 mixture (80% CH_4)	82
4.7	Experimentally-measured time-dependent response of fs/ps CARS for an N_2 - CO_2 mixture (10% CO_2)	83

4.8	Experimental N ₂ -O ₂ CARS Spectra Baseline at a Selection of Pressures (1.11-10.01 bar)	86
4.9	Post-Processing Background Correction For an N ₂ -O ₂ Mixture at a Selection of Pressures (1.11-10.01 bar)	87
4.10	Experimental Excitation Profile: Pump-Stokes Convolution	88
4.11	N ₂ vs. O ₂ Excitation	89
4.12	Air Mixture Time Scans and Averaged Spectra Near $\tau_{probe} = 0$ ps, Recorded at Pressures: 1, 3 and 7 bar (Early November 2023)	91
4.13	Air Mixture Time Scans and Averaged Spectra Near $\tau_{probe} = 0$ ps, Recorded at Pressures: 1 and 4 bar (Mid November 2023)	92
4.14	Air Mixture Time Scans and Averaged Spectra Near $\tau_{probe} = 0$ ps, Recorded at Pressures: 1 and 4 bar (July 2023)	93
4.15	Q-branch Raman spectra of a N ₂ -O ₂ gas mixture ($x_{O_2} = 0.21$, $x_{N_2} = 0.79$)	94
4.16	Experimental intensity ratio $\frac{I_{O_2}}{I_{N_2}}$ measured at absolute pressures from 1–11 bar and four ps probe delays.	95
4.17	Pressure dependence using $\frac{I_{O_2}}{I_{N_2}}$ for an air mixture	97
4.18	Experimental $\frac{I_{O_2}}{I_{N_2}}$ Pressure Dependence vs. Simulation Using Excitation Parameters from Table 4.1 for Air	98
4.19	Simulated pressure dependence for variable N ₂ -O ₂ Gas mixture using the scaled $\frac{I_{O_2}}{I_{N_2}}$ ratio and variable probe parameters ($\lambda = 400$ nm)	99
4.20	Simulated pressure dependence for variable N ₂ -O ₂ Gas mixture using the non-scaled $\frac{I_{O_2}}{I_{N_2}}$ ratio	100
4.21	Pressure dependence in variable concentration N ₂ -O ₂ gas mixtures using the scaled $\frac{I_{O_2}}{I_{N_2}}$ Ratio	101

4.22	Experimental pressure dependence for one N ₂ -CH ₄ gas mixture using the scaled $\frac{I_{N_2}}{I_{CH_4}}$ ratio at two late probe delays	102
4.23	Q-branch Raman spectra of a N ₂ -CO ₂ gas mixture ($x_{CO_2} = 0.1$, $x_{N_2} = 0.9$) at $\tau = 35$ ps spectra	103
4.24	Experimental pressure dependence for one N ₂ -CO ₂ gas mixture using the non-scaled $\frac{I_{CO_2 \nu-}}{I_{CO_2 \nu+}}$ Fermi dyads ratio at $\tau = 35$ ps	104
4.25	Experimental pressure dependence for two N ₂ -CO ₂ gas mixture using the non-scaled $\frac{I_{CO_2 \nu+}}{I_{N_2}}$ ratio at $\tau = 35$ ps	105
5.1	Evolution of the optical spectrum along a Hollow-Core Fiber pumped with an input fs pulse centered at $\lambda = 1550$ nm (From Dr. Paschotta, RP Photonics AG [11])	109
5.2	Preliminary Multi-Probe Generation Experimental Setup	110

1 Introduction

1.1 Motivation

By the early 1960s, the scientific community had managed to assemble a comprehensive understanding of airflow mechanics for speeds reaching approximately Mach 3 [12]. This achievement was made possible through advancements in theoretical models and empirical data collection culminating in a groundbreaking development—the North American X-15, one of the first hypersonic aircraft [13]. However, as the demand for even higher speeds burgeoned, significant design challenges began to emerge, primarily due to the lack of understanding of aerodynamic challenges beyond Mach 3 [13]. It became increasingly evident that a pivotal requirement in bridging this knowledge gap lay in the precise quantification of the in-flow pressure field. This accurate pressure quantification is important for several reasons:

1. Optimizing aerodynamic performance: This encompasses enhancing lift generation, diminishing drag forces, and augmenting maneuverability. Achieving these goals was vital for the development of high-speed aircraft capable of seamlessly traversing the upper reaches of the Earth’s atmosphere.
2. Ensuring structural integrity: This allows engineers to design aircraft that could distribute the extreme loads experienced during high-speed flight across

wings, fuselage, and control surfaces. This not only bolstered the durability of these vehicles but also contributed to their safety.

3. Improving stability and control: By offering insight on the optimal positioning of control surfaces, which ensure maintaining aircraft control at supersonic and hypersonic velocities.
4. Enhancing fuel efficiency: Understanding turbulent combustion behavior at highly compressible conditions, including understanding fluid/chemistry interactions, will lead to improvements in engine performance of high-speed aircraft.
5. Reducing noise and vibrations: By mitigating the adverse effects of acoustic interference on both the aircraft, its occupants, and the surrounding environment.

Air-breathing and rocket-powered high-speed aircraft exhibit either high-pressure reacting flows or local pressure fluctuations due to compressibility effects. Understanding these effects can offer insights into the interplay between flow kinetic energy and internal molecular energy. This improved understanding can lead to advances in high-speed propulsion system design and is crucial for the development of efficient, durable, and robust high-speed aerospace systems such as rocket-powered and scramjet engines.

1.2 Quantifying pressure for high-speed flows: Traditional Techniques

1.2.1 Pitot Tubes

An early instrument employed for pressure measurement is the Pitot tube, invented in the 18th century by Henri Pitot. Functioning on the principle of transforming the kinetic energy of a gas, determined by fluid speed, into potential energy that is subsequently quantified as pressure, Pitot tubes have played a pivotal role in fluid dynamics. Nevertheless, these instruments necessitate meticulous calibration and are vulnerable to inaccuracies due to fluctuations in fluid density affecting velocity measurements, thereby impacting pressure readings. Additional limitations include the potential for altitude/temperature effects, blockage, contamination, and icing. Notably, the tragic incident of the Air France Flight 447 underscores the detrimental consequences of ice crystals obstructing the Pitot tubes.



Figure 1.1: Mirage III right-side profile displaying Pitot tube [1]

1.2.2 Pressure Transducers

Another instrument employed in measuring pressure in high-speed flow applications are pressure transducers. An exemplar of such transducers is the piezoelectric pressure transducer (illustrated in Fig. 1.2), which relies on the conversion of physical pressure into an electrical signal, that can be easily measured and analyzed. The selection of an appropriate pressure transducer is indispensable in ensuring the reliability and precision of data in scenarios involving high-speed flows. Nonetheless, the techniques employed for on-body pressure measurements encounter several challenges. Notably, there are constraints related to low spatial resolution and limited coverage, impeding the ability to capture localized fluctuations in the pressure field. Issues such as limitations in response time and dynamic range can introduce inaccuracies, particularly when attempting to record rapidly changing pressure conditions. Furthermore, some pressure transducers exhibit sensitivity to variations in temperature, necessitating continuous calibration. Failure to maintain or account for temperature conditions can result in inaccuracies in pressure readings. Moreover, the performance of these transducers may be compromised if they are not compatible with all existing reactive species, many of which are challenging to identify or quantify.

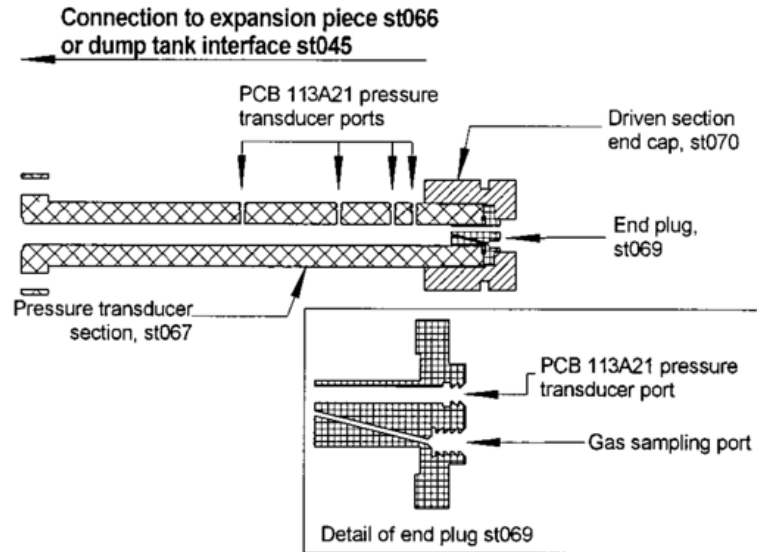


Figure 1.2: Detail of transducer section in a high-pressure shock tube showing PCB-113A23 piezoelectric pressure transducers [2]

1.3 Quantifying pressure for high-speed flows: Optical Techniques

Laser-based diagnostics have advanced significantly in the last few decades offering the ability to analyze compressible flows in a far more robust and accurate manner compared to conventional unreliable sensor-based methods without perturbing the flowfield. Some of the techniques used for pressure measurement are incoherent, path-averaged, time-averaged or indirect methods.

1.3.1 Unsteady Pressure Sensitive Paint (uPSP)

More recently, unsteady Pressure Sensitive Paint (PSP) has been considered for measuring pressures on surfaces, particularly within the context of NASA's Artemis Moon Landing program. The viability of this technique has been tested on NASA's Space Launch System rocket for the program [14]. The basic idea behind PSP is to use a ceramic substrate coated by a luminescent layer of fluorescent molecules embedded in an oxygen permeable binder as illustrated in Fig 1.3. Tracking the changes in fluorescence intensity can be related to changes in the oxygen partial pressure. Although, this technique has higher spatial resolution and coverage compared to transducers and Pitot tubes, it suffers from low Signal-to-Noise Ratio (SNR) due to interference from the paint, the UV excitation lamp and cameras [14, 15].

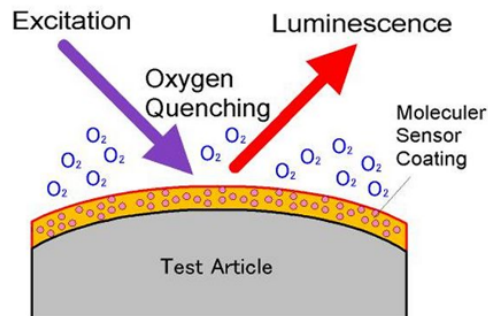


Figure 1.3: Pressure Sensitive Paint (PSP) fundamental principle [3]

1.3.2 Filtered Rayleigh scattering (FRS)

Filtered Rayleigh scattering (FRS) is a non-intrusive technique employed for measuring pressure in fluid flows, as documented in [16], [4], and [17]. This method relies on the scattering of light by gas molecules, primarily nitrogen, within the flow. The intensity of the scattered light is linked to pressure, gas density, temperature, and bulk velocity. Extracting the pressure field poses a challenge due to the coupling of these quantities, necessitating the application of complex mathematical theories and uncertainty analyses, as detailed in [4]. Moreover, FRS encounters challenges related to changes in optical efficiency throughout the experiments and suffers from a low signal-to-noise ratio (SNR) due to external noises and ambient light interfering with the weak FRS signal. Notably, this technique exhibits a low dynamic range, limiting its efficacy in detecting high-pressure gradients.

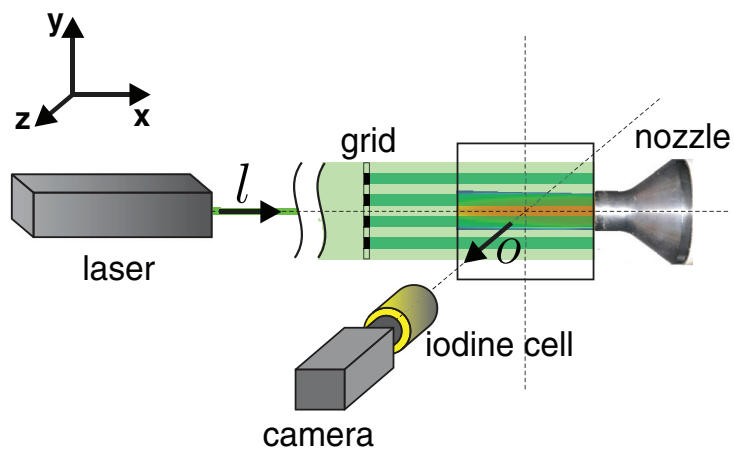


Figure 1.4: FRS geometry for a gas jet experiment implemented by Doll *et. al* [4]

1.3.3 Laser-induced Fluorescence (LIF)

Other noteworthy optical pressure measurement techniques include planar laser-induced fluorescence (PLIF) and OH laser-induced fluorescence (OH-LIF) [5]. Chang *et. al* demonstrated simultaneous, single-point LIF measurements of velocity, temperature, and pressure using the fluorescence spectra of OH in a supersonic axisymmetric free jet, produced by the exhausted products from a high-pressure, stoichiometric CH₄-air combustion chamber as illustrated in the experimental setup in Fig. 1.5. Specifically, pressure is inferred from the collisional broadening observed in the OH spectra. In this instance, the measurement suffered from low pressure sensitivity as Doppler broadening dominated collisional broadening by a factor of 3 to 7 [5] even though pressures measured are between 0.5 and 1.5 atm.

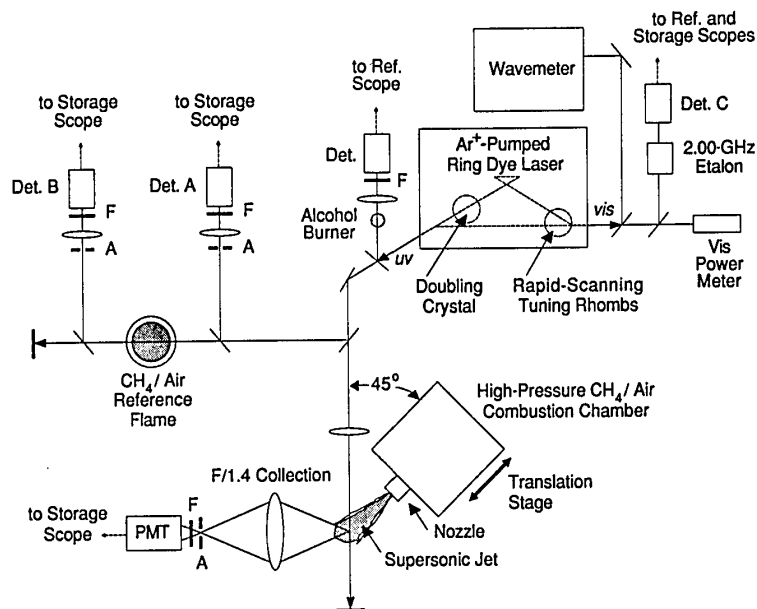


Figure 1.5: Experimental setup for supersonic jet presented by Chang *et. al* [5]

In general, these fluorescence techniques are incoherent and face challenges related to the limited fluorescence lifetime, low SNR, and interference scattering from the walls of the test section and entrained particulates such as dust, dirt, and condensed ice crystals. These factors substantially diminish the strength of the fluorescence signal.

1.3.4 Interferometry

Mach-Zehnder [6] and Fabry-Perot interferometry [18] have been previously applied for pressure measurement by analyzing the interference pattern created after light passes through an interferometer. Li *et al.* used a micro-channel based twin-core fiber (TCF) in-line Mach-Zehnder interferometer (MZI) for detecting gas pressure in a cell ranging from 0.2 to 2 MPa.

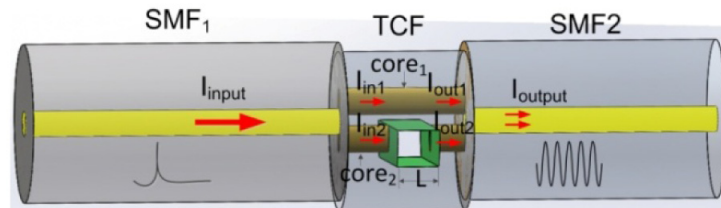


Figure 1.6: Schematic of the TCF based MZI used in the experimental setup presented by Li *et al.* [6]

Nevertheless, these methods are renowned for requiring costly equipment, intricate implementation, and precise calibration. The accuracy of interferometric measurements is highly influenced by the quality of optical surfaces and the reflectivity of materials, and the quality of the machining of the interferometer (i.e.

fs laser micro-machining) thereby introducing additional layers of complexity and making them too expensive to apply for practical applications.

1.3.5 Tunable Diode Laser-Absorption Spectroscopy (TDLAS)

Tunable diode laser-absorption spectroscopy (TDLAS) [7] is utilized for pressure quantification, with varying methodologies. One such application by Jousten *et al.* involves correlating the absorption of light at the R(12) transition of CO₂ (at 4987.3 cm^{-1}) with gas partial pressures within a vacuum.

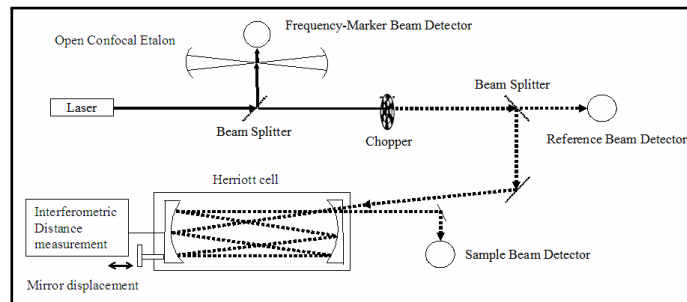


Figure 1.7: Experimental set up of the TDLAS presented by Jousten *et al.* [7]

However, TDLAS pressure measurements are susceptible to inaccuracies due to temperature changes. This sensitivity arises from the impact of temperature variations on absorbance spectra. Compensating for temperature effects is challenging as pressure, temperature, and collisional effects can broaden the absorption lines of gases, complicating spectral interpretation and introducing uncertainties. Additionally, measurement accuracy relies heavily on the selection of the absorption line and the overall experimental setup. Factors such as the precision of the spectral database and calibration further influence the accuracy of TDLAS measurements.

Finally TDLAS is a line-of-sight technique, making it unsuitable for studying local fluctuations of pressure.

1.4 Using Coherent anti-Stokes Raman Scattering (CARS) for Quantifying Pressure in high-speed flow

Coherent anti-Stokes Raman scattering (CARS) spectroscopy is a powerful technique used extensively for quantifying temperature and species concentration in gas-phase reacting systems [19] [20] [21]. CARS leverages the Raman effect, where three incident electric fields interact with an ensemble of molecules, resulting in inelastic light scattering at a frequency shift that corresponds to the difference in rotational and vibrational levels of the molecules. In CARS, two synchronized coherent laser beams are typically used for generating a Raman coherence, and a third beam is used to probe the coherence to create a coherent signal beam that contains thermodynamic information on temperature, species and pressure pertaining to the molecular sample. This synchronization enhances sensitivity, making CARS suitable for detecting weak Raman signals at even low gas densities. By varying the beam wavelengths and analyzing the unique spectra of chemical mixtures, CARS can identify molecules and sample their population distribution across internal energy levels.

1.4.1 Frequency Domain CARS

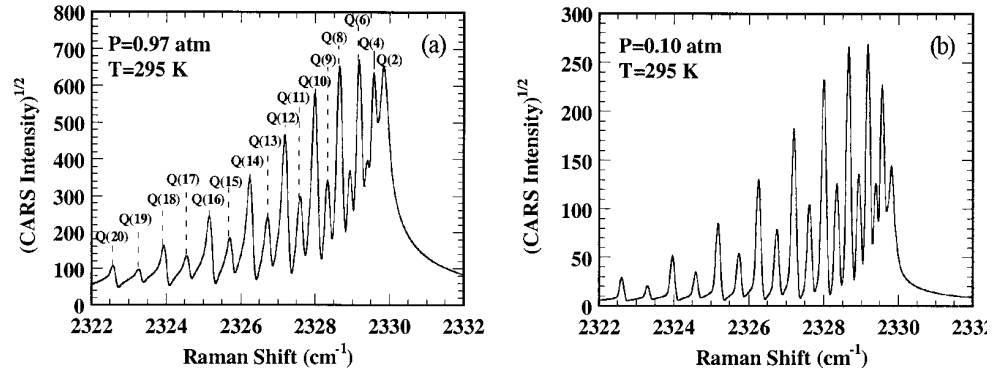


Figure 1.8: CARSFIT spectra presented by Woodmansee *et. al* at $p = 0.97$ atm (a) and $p = 0.1$ atm (b) [8]

Detecting pressure changes has been demonstrated using dual-pump nanosecond CARS: in a small-scale pressure cell [22], a heated pressure vessel [23] and in an underexpanded sonic jet flow [8]. The earliest frequency domain pressure measurement by Woodmansee *et. al* relies on tracking the effect of pressure on the rotational linewidths of N_2 . This technique has shown good agreement with transducers for pressures above 0.1 and up to 5.0 atm. However, this technique displays a lack of sensitivity to pressure under 0.1 atm because the thermal Doppler broadening effects dominate over the collisional pressure broadening effects.

1.4.2 Time Domain Hybrid fs/ps CARS

Lately, hybrid femtosecond-picosecond CARS rose to the forefront of quantitative combustion diagnostics due to its capability of accurately quantifying temperature

by suppressing non-resonant background signal [24] and achieving greater spatio-temporal precision when compared with the aforementioned techniques [25–27]. Using this technique at the kHz-rate measurements offers enhanced temporal resolution allowing for an instantaneous precise capture of highly dynamic reacting flows.

1.4.2.1 Hybrid fs/ps Rotational CARS for Pressure Detection

Using broadband excitation at appropriate probe delays. Fs/ps pure-rotational CARS can be used to accurately quantify pressure using collisional dephasing (τ_J) of rotational Raman transitions [9]. This technique is sensitive to low-to-moderate pressures in the range of several torr to a few atmospheres typical for plasma diagnostics or supersonic ground-test facilities. Kearney and Danehy [9] applied this technique in a room-temperature gas cell for pressures ranging from 0.4 to 3 atm and probe delays ranging from 16 to 298 ps as illustrated in Fig. 1.9.

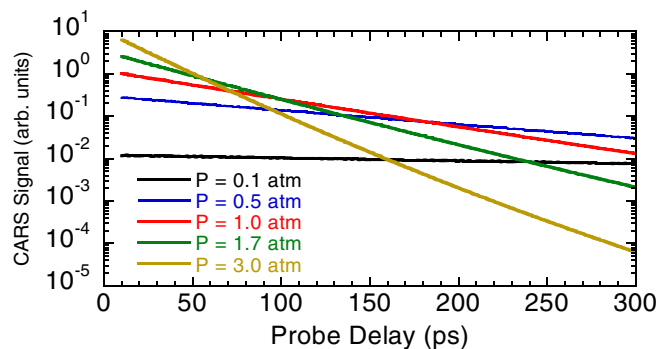


Figure 1.9: Calculated decay of the spectrally integrated fs/ps rotational CARS signal by Kearney and Danehy [9]

Additionally, Dedic *et. al* [10] presented a demonstration of pressure measurements using hybrid fs/ps rotational CARS in the range of 40–100 Torr for three supersonic flow facilities. Fig. 1.10 shows pressure sensitivity at three late probe delays of (a) 490 ps, (b) 980 ps, and (c) 1470 ps.

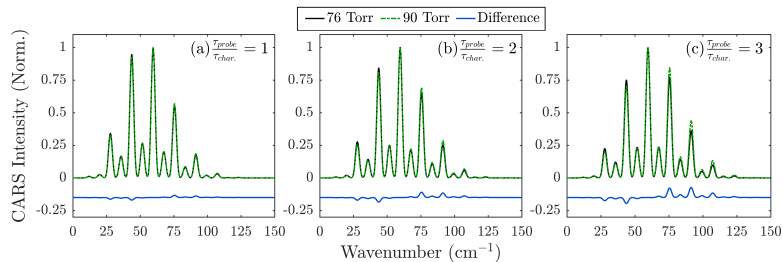


Figure 1.10: Simulated CARS spectra for a Mach 2.7 nozzle at 90 torr (black solid line) and 76 torr (green dashed line) by Dedic *et. al* [10]

Due to the high electric field strengths available with fs laser excitation, this method may also be applied to measure pressure and temperature profiles along a 1D 5-mm long domain, as was demonstrated in a non-reacting underexpanded sonic jet. Those measurements were conducted in the steady barrel-shock region, upstream of the Mach disk [28]. Fig. 1.11 shows a sample single-shot CARS fits within the jet implemented by Retter and coworkers. The temperature profile was measured at $\tau = 0$ ps and pressure at $\tau = 200, 400, 600$ and 1000 ps (right) in five axial locations at 2.97, 6.04, 7.9, 11.5, and 13.4 mm are included.

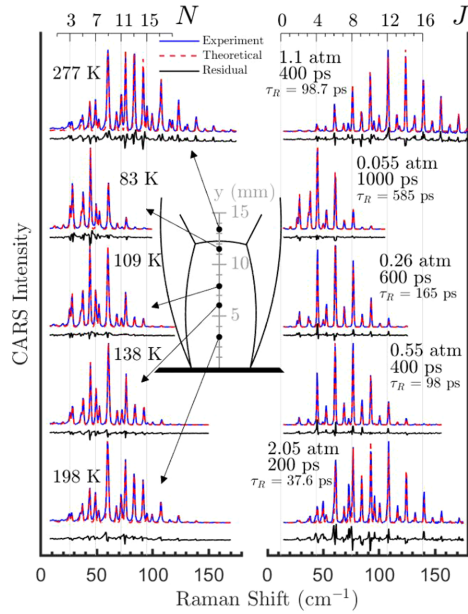


Figure 1.11: Sample Single-Shot CARS Fits within a Supersonic-Coaxial Jet. Temperature Measured (left) and pressure Measured (right)

However, the hybrid time–frequency domain rotational fs/ps CARS technique presents several challenges such as the long dephasing time, low signal, lack of sensitivity for species with low dipole moment (i.e. CO_2) and large uncertainties at low pressures [28]. Furthermore, it is not yet demonstrated for reacting flows where uncertainty in collisional partners introduces considerable uncertainty in pressure measurements.

1.4.2.2 Hybrid fs/ps Vibrational CARS for Pressure Detection

In this work, Q-branch CARS (VACARS) is investigated as an alternative to overcome challenges in using S-branch CARS (RCARS). This is because S-branch

CARS does not exist for some combustion species and often suffers from low intensity. In contrast, Q-branch CARS is more intense (orders of magnitude higher) and can be used by leveraging the relative decay of overlapping transitions of spectrally isolated species. VCARS exhibits larger changes in spectral features as pressure is varied compared to RCARS at significantly lower probe delays. This is demonstrated in Fig. 1.12 where a large change in relative VCARS signal is shown for a 10% change in pressure at $\tau = 40$ ps whereas RCARS shows a smaller magnitude change in signal for a 15% change in pressure that can only be detected after a long probe delay of $\tau = 1470$ ps.

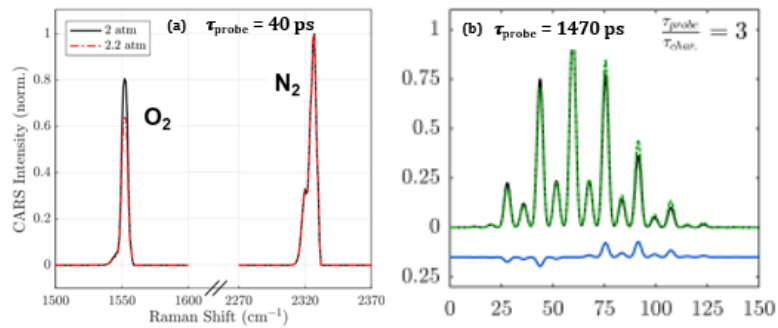


Figure 1.12: Comparison of (a) VCARS Pressure Sensitivity and (b) RCARS (by Dedic *et. al* [10])

This work also proposes simultaneous measurement of temperature (T), species (x_i) and pressure (p), employing dual-probe VCARS at two different delays with respect to the excitation pulses: one early probe insensitive to collisions allowing for an accurate measure for T and x_i , and another late probe sensitive to molecular collisions allowing for an accurate measure of (p). The proposed scheme will be discussed in Chapter 2 and it entails using the most efficient outputs of a Ra-

man shifting crystal (KGW). This multi-color generation can be used to create high-energy ps probe pulses of varying time delays, enabling measurement of T , x_i , and p , while the detection of the frequency-separated annulus-shaped signals will be accomplished using a single spectrometer/camera. The use of two probes simultaneously is necessary for making single-shot measurements of pressure in a fluctuating flowfield.

1.5 Research Objectives

Given the need for an accurate quantification of pressure in addition to temperature to study compressible reacting flows, the global objective for this thesis is to design a fs/ps CARS measurement methodology for detecting in-stream pressure fluctuations in a reacting flow. This goal will be tackled by:

1. Improving spectral modeling for fs/ps CARS accounting for species-dependent pressure broadening effects.
2. Investigating Q-branch pressure/species response using spectral simulations as well as experimentally in a controlled, high pressure binary and tertiary mixtures using hybrid fs/ps CARS by employing a newly implemented narrowband ps probe pulse.
3. Devising a novel method for extracting gas flow pressure using hybrid fs/ps CARS that virtually eliminates issues related to quantifying excitation uncertainties.

1.6 Thesis Outline

The following is a brief summary of the topics covered in this thesis.

- Chapter 2 will provide an overview of relevant CARS theory and the experimental methods employed.
- Chapter 3 will investigate the impact of gas pressure on fs/ps CARS using spectral simulations of N_2 and O_2 and will discuss the optimization of a collisional linewidth model for a broad range of temperatures (80-240K) and three species collisions.
- Chapter 4 will discuss the experimental setup, results, analysis procedure and discussion exploring the hybrid fs/ps CARS response in a static pressure cell.
- Chapter 5 will conclude with a summary of research and future vision regarding potential progress on this topic.

2 Theoretical and Experimental Approach

2.1 Hybrid fs/ps CARS

Hybrid femtosecond/picosecond CARS is a nonlinear four-wave mixing spectroscopic technique that combines the advantages of both femtosecond and picosecond laser pulses to achieve broadband excitation, sufficient spectral resolution, nonresonant background suppression, and the possibility of one-dimensional instantaneous sampling. Two femtosecond pulses, termed pump and Stokes, provide high peak power broadband excitation of the Raman transition. A picosecond probe pulse is simultaneously employed to allow for a well-resolved observation of various spectral features. The interaction of the three beams produces a coherent wave at a frequency determined by the principle of energy conservation given by Eq. 2.1:

$$\omega_{pump} - \omega_{Stokes} + \omega_{probe} = \omega_{CARS}. \quad (2.1)$$

This setup is deployed at a repetition rate of 1 kHz. In order to target various species, the pump beam wavelength is adjusted in the range of 670–715 nm to detect various molecular transitions of interest (Table 2.1) while Stokes is held constant at 800 nm. Multiple species may be excited simultaneously using the bandwidth of the 60 fs pulses such as O_2 - CO_2 and O_2 - N_2 mixtures. A frequency-narrowed ps probe is deployed for spectrally-resolved detection.

Table 2.1: Raman shifts of the various species of interest

Species	Raman Shift
N_2	$2335 \text{ cm}^{-1} (v_1)$
O_2	$1556 \text{ cm}^{-1} (v_1)$
CH_4	$2915 \text{ cm}^{-1} (v_1)$
	$3017 \text{ cm}^{-1} (v_3)$
CO_2	$1283 \text{ cm}^{-1} (v^-)$
	$1388 \text{ cm}^{-1} (v^+)$

In order to produce a well separated CARS beam and ensure that wave mixing only occurs at a small measurement location, co-linearity must be avoided while obeying the principle of conservation of momentum as Eq. (2.2) outlines:

$$\mathbf{k}_{pump} - \mathbf{k}_{Stokes} + \mathbf{k}_{probe} = \mathbf{k}_{CARS}, \quad (2.2)$$

where $k = \frac{2\pi}{\lambda}$ represents the wave vector. In this work, a folded BOXCARS phase-matching configuration with a $\sim 5^\circ$ crossing angle between pump and Stokes beams is employed as shown in the following figure 2.1:

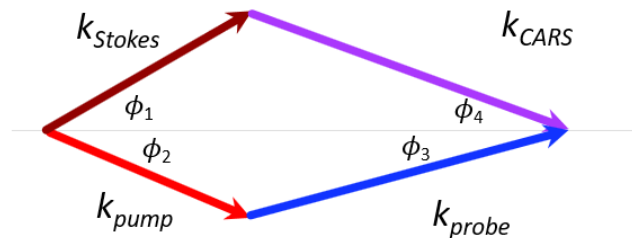


Figure 2.1: CARS phase-matching scheme

The ps probe pulse is introduced at a time delay of $\tau_{probe} = 5-45$ ps with respect to pump/Stokes (Fig. 2.2) to sample the Raman response before and after molecular collisions become significant.

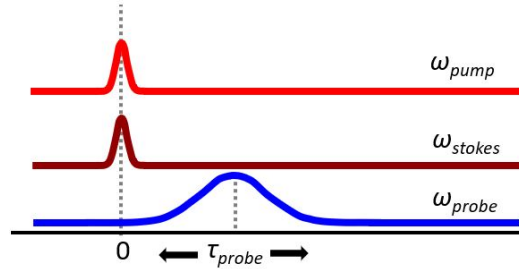


Figure 2.2: Timing diagram for fs/ps CARS.

With pump and Stokes pulses introduced at time $t = 0$ ps and probe pulse introduced at a delay (τ_{probe}), the time-domain Raman-resonant CARS polarization is a function of probe pulse electric field, E_3 , and the molecular Raman response function, $R(t)$, which carries information about pressure. In this thesis, the CARS signal is scaled by the nonresonant background spectra acquired at $\tau_{probe} = 0$ ps within an Argon environment at near-atmospheric pressure. This aims to account for the non-uniform excitation of the various species [29, 30]. After quantifying the excitation bandwidth ($\Delta\nu \sim 500 \text{ cm}^{-1}$), the fs pump frequency is chosen such that multiple species are targeted as shown in 2.3. In some cases, for example when an $\text{N}_2\text{-CH}_4$ is examined, the excitation is not exactly centered between the two species allowing for more stimulation of N_2 compared to CH_4 molecules. This aims to account for the difference in relative concentration as well as the initial dephasing times ($\tau_{CARS, \text{N}_2} \sim 7$ ps and $\tau_{CARS, \text{CH}_4} \sim 45$ ps) ensuring an adequate

SNR at late probe delays and low pressures.

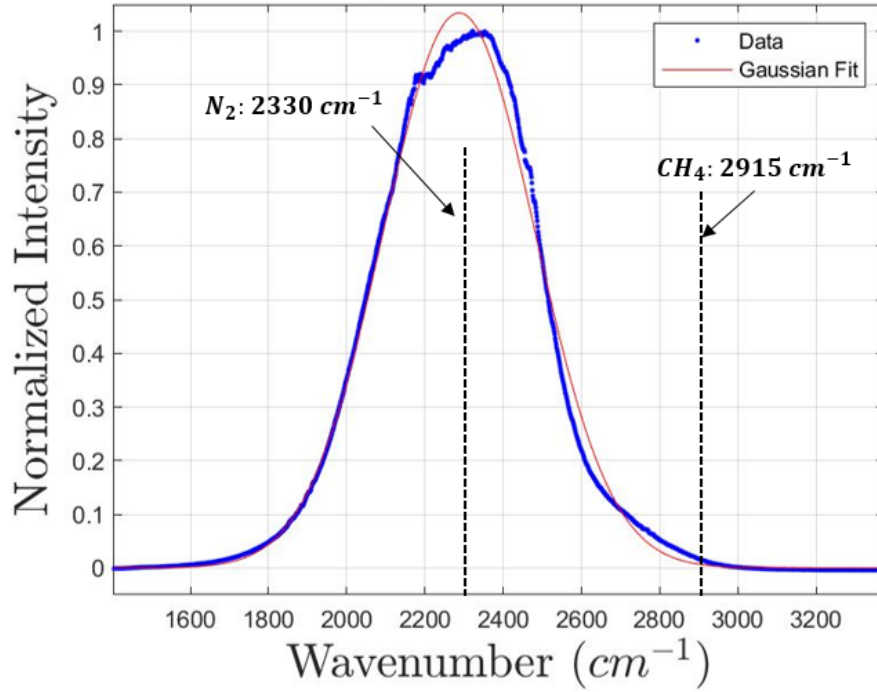


Figure 2.3: Excitation profile: $\lambda_{pump} = 670$ nm, $\lambda_{Stokes} = 800$ nm @ $p_{Ar} \sim 1$ bar

Various gas mixtures are studied to provide a preliminary understanding of spectral variations at different pressures of interest. This is achieved in the vicinity of N₂-O₂, N₂-CO₂-O₂ and N₂-CH₄ resonances, as summarized in the energy diagrams shown in Figure 2.4.

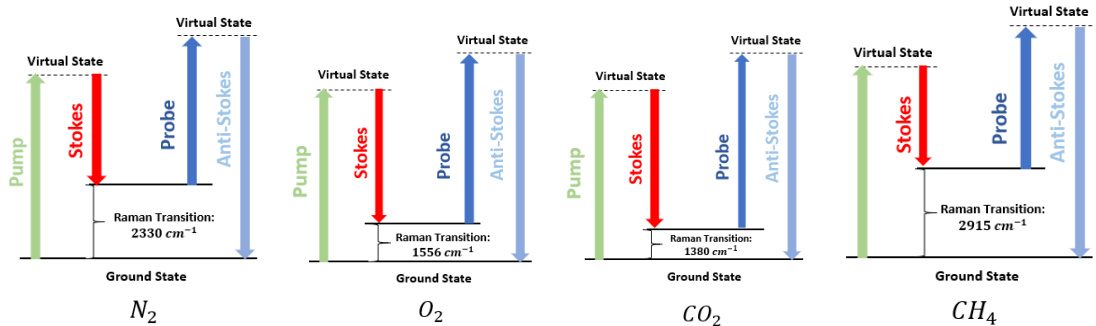


Figure 2.4: Broadband energy-level CARS diagrams for N_2 , O_2 , CO_2 and CH_4 .

2.2 SHBC Design

To create the ps pulse necessary for the CARS experiment, two ideas are considered. A 4-f pulse shaper, used previously, selects a small frequency range of the input broadband pulse using an adjustable slit placed at the Fourier plane of the pulse shaper. However, this method leads to a significant compromise in output energy with an efficiency of only $\sim 1\%$. This low-energy output issue is addressed by designing a more efficient pulse shaper: a second harmonic bandwidth compressor (SHBC) [31]. This lab-scale system efficiency can approach that of commercial system, reaching an efficiency of $\sim 20 - 30\%$.

The main mechanism of the SHBC relies on delivering two equally but inversely chirped pulses to a non-linear medium. This produces a frequency doubled output 2ω in addition to a residual pulse of the same input frequency ω which can be almost entirely eliminated using precise alignment.

The SHBC (Fig. 2.5) is assembled on a 24" x 24" breadboard and integrated into the laser main table in place of the previously used 4-f pulse shaper. The

system takes an 800 nm fs pulse, directs it through a halfwaveplate towards a 50-50 beamsplitter. The reflected beam passes through a pulse stretcher comprising a blazed pulse compression diffraction grating (Spectrogon, 1200 g/mm), a cylindrical lens ($f = 200mm$), and a back mirror fixed at a $1f$ distance from the lens. The mirror and lens attach to a rail with a micrometer for adjustable lens-grating distance ($f - x$). The transmitted beam goes through an identical stretcher with the lens-grating distance adjusted to ($f + x$). These adjustments achieve opposite chirping for equal pulse stretching. Using the same grating minimizes groove variation stemming from manufacturing uncertainty and optimizes space utilization before the system is moved to the main laser table.

The outputs from the stretchers are then directed to a non-linear medium: a type I beta barium borate crystal (EKSPA Optics, p/n BBO-605H Crystal) with the dimensions: $10 \times 10 \times 2mm$. The BBO is cut and polished with the effective non-linearity phase angles of $\phi = 29.2^\circ$ and $\theta = 90^\circ$ and mounted in 1" ring holder inside a rotation mount. Each beam compression is adjusted iteratively to ensure optimal high-power narrowband output following the second harmonic generation process. In addition to equal in magnitude and opposite in sign chirp produced in each leg, temporal overlap must be satisfied and it was achieved using a 2" delay stage on one of the legs. ensuring spatial overlap is enhanced using a Galilean Telescope to ensure tight focusing into the center of the BBO.

Once a sufficiently-high conversion efficiency is achieved (20%), the output pulse bandwidth is slightly modified using a systematic adjustment of the SHBC pulse stretchers. Producing a narrowband pulse to ensure adequate spectral res-

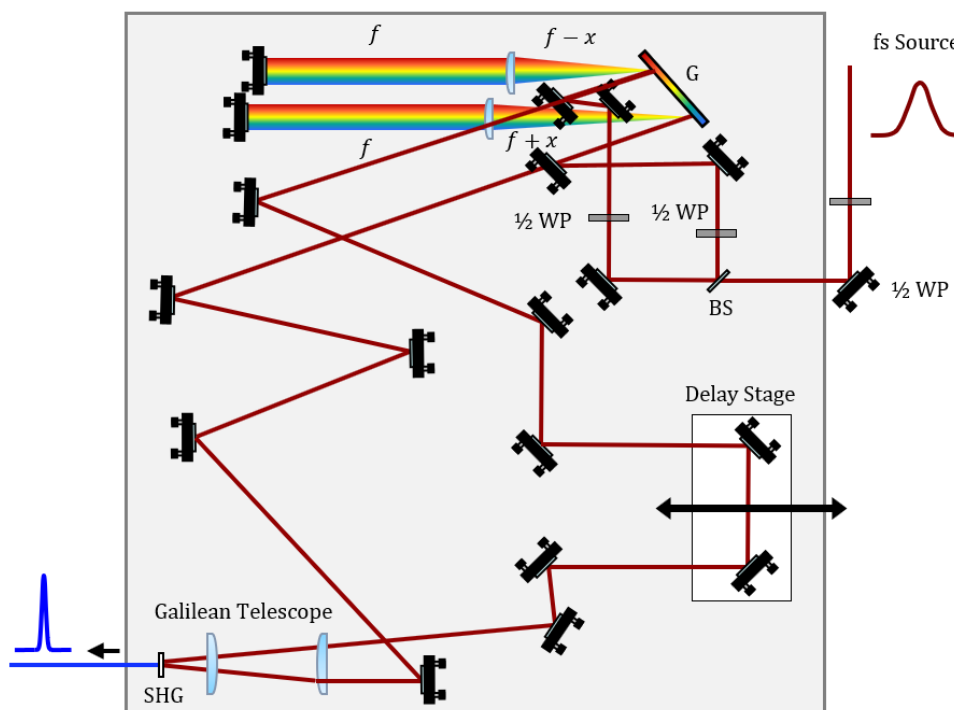


Figure 2.5: SHBC optical layout

olution is demonstrated in the following time and frequency domain plots (Fig. 2.6 measured by performing a -15 to 15 ps time scan of the probe pulse within an non-resonant Argon environment. Quantitatively, a 3.35 ps probe results in a bandwidth of 4.43 cm^{-1} based on a Gaussian fit of the Fourier transform of the time domain spectra (with a time-bandwidth product of $14.87 \text{ ps} \cdot \text{cm}^{-1}$).

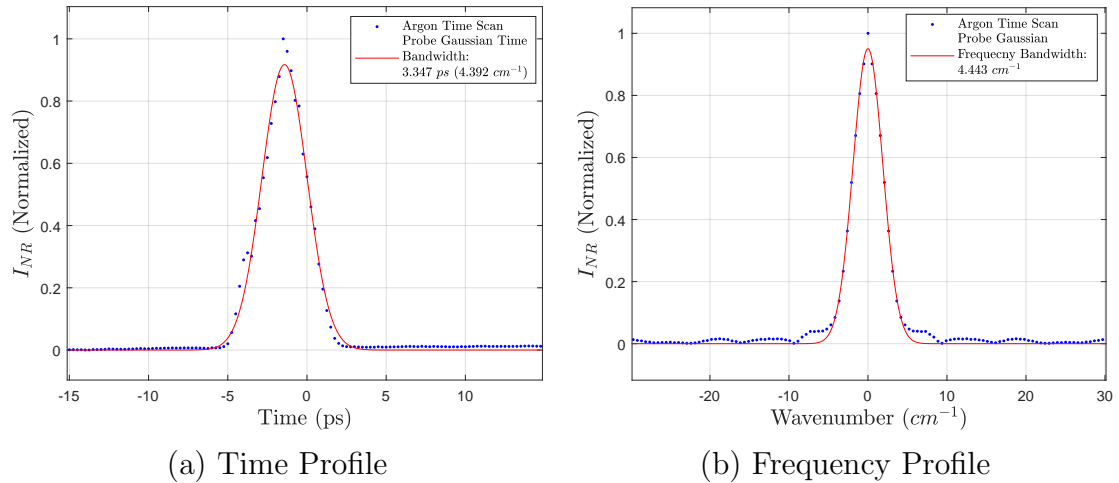


Figure 2.6: Experimentally measured SHBC probe profile with a Gaussian fit

2.3 Experimental Setup

2.3.1 Optical Layout

The experimental optical setup for the hybrid fs/ps CARS system is depicted in Fig. 2.7. A Ti:sapphire kHz-rate laser (Coherent Astrella) is used to generate a fs pulse which is split after pulse amplification. One part is directed towards a pulse compressor and then an optical parametric amplifier (Light Conversion TOPAS-Prime) that is used to produce the tunable pump pulse. The second part is directed to a separate pulse compressor and then split with one part used to produce the Stokes pulse (800 nm) and the second part towards the SHBC which generates a narrowband 400 nm ps probe pulse. Each of pump and Stokes lines contain delay stages used to ensure temporal overlap. The ps probe pulse is also routed through a motorized delay stage and the pulse timing is modified during the experiment to

suppress non-resonant background and achieve various probe delays to investigate pressure sensitivity. The beams are overlapped spatially and temporally at the center of the pressure cell. The CARS signal generated in the gas mixture is spatially filtered using an iris and focused into a 0.320 m spectrometer equipped with a 2400 line/mm grating (IsoPlane 320, Princeton Instruments) resulting in a nominal resolution of $\sim 0.0163 \frac{nm}{pixel}$. The spectra are recorded using an electron-multiplied charge-coupled device (EMCCD) camera (ProEM 1600 eXcelon 3).

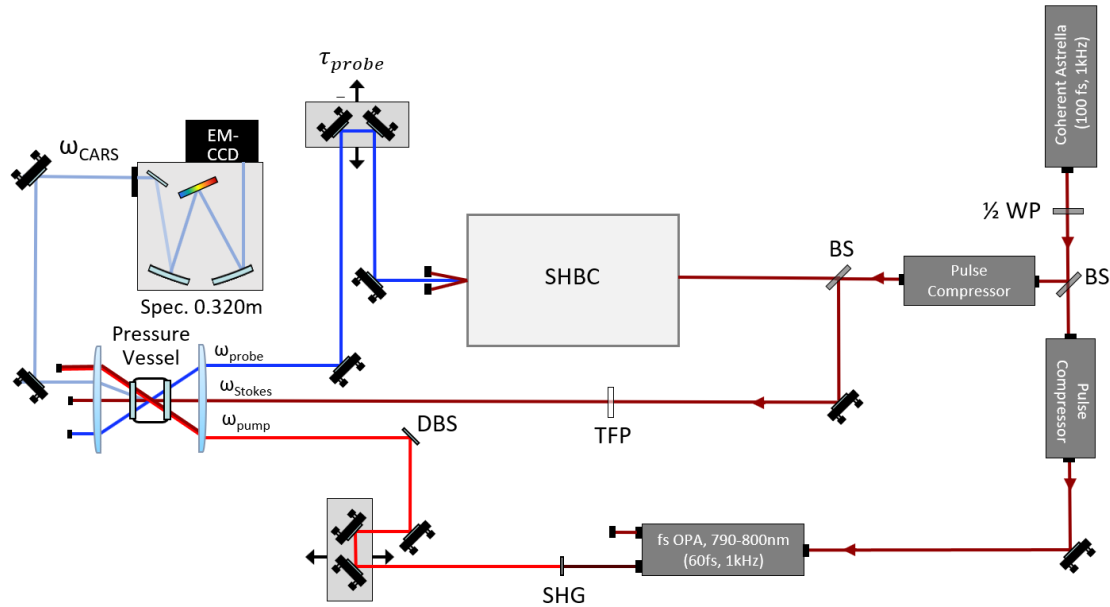


Figure 2.7: Experimental schematic of hybrid fs/ps CARS system in pressure cell. WP: waveplate, SHG: second-harmonic-generation crystal, BS: beamsplitter, EMCCD: electron-multiplied charge-coupled device camera.

2.3.2 High-Pressure Gas Cell

To simulate a high-pressure combustion environment, a custom pressure cell was utilized. A rendering of this gas cell is shown in Fig. 2.8. The cell has two-sided optical access through two AR-coated N-BK7 High Precision Windows (ThorLabs WG12012-A) limiting beam energy losses to a maximum of 0.75% in the range of 400 to 715 nm. The flanges supporting the transmission and collection windows lead to 1.610" of clear aperture ("E" in Fig. 2.8). The cell is equipped with a K-type thermocouple and a digital pressure gauge (with a 0.01 resolution) used to monitor temperature and total pressure respectively during the experiment.

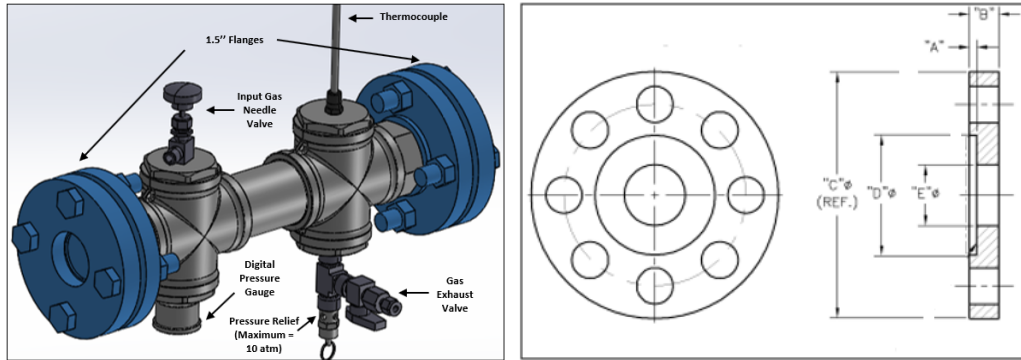


Figure 2.8: Pressure cell 3D view and flange cross section

Using the ideal-gas assumption, the cell is filled according to Dalton's law of partial pressures. For each binary mixture, the gases are filled according to Eq. 2.3 where (p_1, x_1) and (p_2, x_2) are the pressures and mole fractions of Gas 1 and Gas 2, respectively:

$$P_{Tot} = x_1 p_1 + x_2 p_2 \quad (2.3)$$

This was implemented by filling to the first gas pressure and then completing the process by filling the second gas until the total pressure is reached. This process uses a 4-needle-valve system that ensures the tubing at the gases input is purged and allows for a more accurate final composition. The gas cell was filled to a higher pressure than the desired measurement condition and then lowered by 1 bar to enhance mixing in the cell. The validity of the mixing uniformity assumption was investigated experimentally by comparing reverse gas-filling at the same molar composition.

2.4 CARS Spectral Modeling

Prior research has laid the groundwork for a comprehensive understanding of the wave equation when applied to light scattering processes, encompassing quantum, classical, and semi-classical approaches. This framework outlines the link between vibrational/rotational molecular transitions manifested in electromagnetic waves and the polarization field induced in molecules. This key principle is the foundation for the study of gas-phase molecules using Coherent anti-Stokes Raman scattering. The CARS signal exhibited in isotropic mediums such as gases can be expressed as the square of the sum of all the odd-ordered components of the polarization field as Eq. 2.4 shows:

$$I_{CARS}(\omega) \propto |P_{res}^{(3)}(\omega) + P_{nonres}^{(3)}(\omega)|^2 \quad (2.4)$$

The advantage of hybrid fs/ps CARS is the possibility of eliminating the $P_{nonres}^{(3)}(\omega)$ component of the CARS signal because Raman transitions are excited within a femtosecond time-scale while the probing of the molecular response occurs on the picosecond time-scale. Leveraging the hybrid nature of this process means the nonresonant signal can be suppressed by delaying the probe pulse appropriately so that the three waves (pump, Stokes and probe) are not exactly overlapped in time. This way nonresonant wave mixing is ensured to dephase quickly such that its contribution to the observed CARS signal is nearly zero. This allows for the CARS intensity to be expressed simply in the frequency domain as the resonant contribution [32] as shown in Eq. 2.5 [19]:

$$I_{CARS}(\omega) \propto |P_{res}^{(3)}(\omega)|^2 = \left| \epsilon_0 \chi_{CARS}^{(3)} E_1(\omega_1) E_2(\omega_2) E_3(\omega_3) \right| \quad (2.5)$$

The CARS signal is a function of ω_4 , the signal frequency. It depends on the intensity of the electric fields in the wave mixing process: pump (E_1), Stokes (E_2) and probe (E_3). More significantly, the signal depends on the CARS susceptibility which contains information on the molecular activity in a given parcel of gas. Therefore the variations in the CARS signal can be used to extract key thermodynamic parameters.

The CARS signal can also be expressed in the time domain as a function of the difference in population between the relevant states, the discrete energy difference between these states (or transition frequencies), the collisional linewidths, and the

Raman intensity as shown by Eq. 2.6 per Retter *et al.* [28] formulation:

$$I_{CARS} \propto E_3(t - \tau) \times R_4(t) \quad (2.6)$$

Including the explicit expression for the molecular response function $R_4(t)$ as per [33] yields Eq. 2.7:

$$I_{CARS} \propto E_3(t - \tau) \times \Delta N \times \sum_v \sum_J I_{v, J_i \rightarrow v+1, J_f}(T) \cdot \exp \left[\frac{t}{\hbar} \left(i\Delta E_{v, J_i \rightarrow v+1, J_f} - \frac{1}{2}\Gamma_{v, J_i \rightarrow v+1, J_f}(T, p) \right) \right] \quad (2.7)$$

In this context, v and J denote vibrational and rotational quantum numbers, respectively. The intensity of Coherent Anti-Stokes Raman Scattering (CARS) is influenced by the probe pulse, introduced at a delay of τ_{probe} . The key components of the CARS intensity equation include the number density (ΔN), often approximated using the ideal gas law ($\frac{p}{kT}$), the transition energy difference ($\Delta E_{i \rightarrow f}$), the Raman transition intensity ($I_{v, J_i \rightarrow v+1, J_f} \propto \frac{\partial \sigma}{\partial \omega}$), and the transition collisional linewidth ($\Gamma_{v, J_i \rightarrow v+1, J_f}$). In this work, the primary focus of the modeling effort will be on the transition collisional linewidth.

Additional comprehensive details regarding the fs/ps CARS code utilized in this thesis can be found in previous work [34, 35]. This study, in particular, will focus on the modeling aspects related to collisional linewidths to improve the accuracy of quantifying pressure using ro-vibrational spectral features.

2.5 Collisional Line Broadening and Linewidth Models

Early efforts to calculate linewidth (also called the scattering G- or S-matrix in early sources) relied on two widely used scaling laws for the N₂ Q-branch: power-law [36–38] and Exponential-Gap (EG) models [39, 40]. Model predictions have been improved from those early efforts by the introduction of the Modified Exponential Gap (MEG) model by Rahn and colleagues in 1986 [41]. Since then, it has undergone extensive evaluation with data from various sources, as reviewed by different authors [35, 42–44]. Furthermore, the Energy Corrected Sudden (ECS) collision model is another statistical model incorporating more insight on the state-to-state physics of transitions. ECS has a multitude of variants, and it is a subject of discussion in numerous scholarly works: the ECS-P law posits a power-law dependence, the ECS-E law assumes an exponential gap dependence and the ECS-EP model encompasses elements of both, each with its own distinctive variations.

For experimentalists, the choice of CARS spectra analysis methods varies based on experimental conditions, prior research, and data availability. Some researchers rely on established models and fitting parameters, while others devise their own linewidth calculation methodologies. In the context of this study, a form of the Modified Exponential Gap (MEG) model is used to model collisional Raman linewidths. To enhance the accuracy of spectral fits and minimize residuals when employing linewidth models, it is imperative to refine and optimize existing models utilizing experimental data across a broad temperature range. This section will discuss the physical and mathematical framework of the MEG model and improve-

ments will be covered in Chapter 3 within the context of a compilation of measured linewidths.

Rotational Raman spectral lines for nitrogen (N_2) and oxygen (O_2) are separated by approximately 8 cm^{-1} , and this spacing allows us to treat the lines as isolated, as substantiated by experimental findings [45] [46]. Consequently, this model operates under the assumption of perfectly isolated lines. The broadening of isolated rotational Raman lines primarily arises from inelastic collision-induced alterations in rotational states [47]. Doppler broadening can also exert an influence, especially at lower pressures and higher temperatures, so it must be accounted for in the analysis while recognizing that its contribution remains minimal. Thus, the simulated linewidths especially at low pressures must encompass both collisional and Doppler contributions. Now, the collisional linewidth of an isolated Raman transition is related to the rotational state-to-state relaxation rates. These rates are the off-diagonal elements of the relaxation matrix, known as the G-matrix as described by Koszykowski *et al.* [48]. This allows Γ_J to be expressed as:

$$\Gamma_J = \sum_{i \neq j} \Gamma_{i,j} = \sum_{i \neq j} 2\gamma_{i,j} \quad (2.8)$$

where j represents the rotational state of interest and i represents the other available rotational states. Here $\Gamma_{i,j}$ represents the FWHM (full width at half-maximum) linewidth, while $\gamma_{i,j}$ represents the HWHM (half width at half-maximum) linewidth. Some sources report their linewidths as a HWHM without including the $\times 2$ factor. Therefore, care must be taken when considering linewidth measure-

ments to avoid error. Furthermore, some results are approximations derived from Q-branch measurements. For vibrational Raman transitions, the selection rule is $\Delta J = 0$. Other results report direct S-branch measurements. For rotational Raman transitions, the selection rule is $\Delta J = \pm 2$. In this case, the sum in Eq. 2.8 is made only over the participating J levels, not over all of them.

2.5.1 Modeling Overview

Two primary categories of fitting models are commonly utilized in this field: dynamic physical models grounded in angular momentum scaling and statistical semi-physical models. The Modified Exponential Gap (MEG) model stands out as the foremost statistical model in this landscape. In the realm of dynamic physical models, the Energy Corrected Sudden (ECS) model is the dominant choice, offering various iterations, including ECS-EP. Nevertheless, ECS, despite its wealth of physical intricacies, demands substantial computational resources and lags behind the MEG model, especially in terms of aligning with experimental data, particularly at lower temperatures, as highlighted by Linne *et al.* in their work [44]. Consequently, this study places primary emphasis on the MEG model when investigating interactions with common combustion collisional partners, including N_2 , O_2 , and H_2 .

2.5.2 Modified Exponential Gap (MEG) Model

The Modified Exponential Gap (MEG) model serves the purpose of computing upward transition rates $\gamma_{i,j}$ from rotational state i to j , with the constraint that i is less than j [41]. Firstly, it constructs the lower-left portion of the Γ_J matrix, as follows:

$$\gamma_{j,i} = p\alpha \left(\frac{1 - e^{-m}}{1 - e^{-mT/T_0}} \right) \left(\frac{T_0}{T} \right)^n \left(\frac{1 + \frac{aE_i}{k_bT\delta}}{1 + \frac{aE_i}{k_bT}} \right)^2 \exp \left(\frac{-\beta\Delta E_{i,j}}{k_bT} \right) \quad (2.9)$$

In the context of this equation, where p represents pressure (typically measured in *atm*), k_b denotes the Boltzmann constant, and T signifies temperature, experimentalists often manipulate the parameter α (in units of $cm^{-1} atm^{-1}$) to achieve the appropriate scaling of decay rates. The temperature ratio, denoted as $\frac{T_0}{T}$ and raised to the power of the dimensionless parameter n , effectively encapsulates the observed linewidth results at moderately high temperatures. The temperature power law dependence here is scaled by a reference temperature T_0 , usually set to 295 K. Similarly, there exists another scaling term tailored for even higher temperature conditions. It incorporates the parameter m and adopts a population probability cumulative distribution function ratio form. The introduction of β is driven by the necessity to tailor the Arrhenius kinetic equation to empirically capture early J decay phenomena. Additionally, δ serves as a fitting parameter linked to energy scaling, while the constant factor a is usually set to 1.5 for interactions involving N_2-N_2 , O_2-O_2 , N_2-O_2 , and O_2-N_2 , as detailed in the work by Seeger *et*

al. [49]. This parameterization is associated with the specific bonds of interest, characterizing inter-nuclear separation distance, the collision interaction length, and the reduced mass.

Secondly, the model constructs the upper-left portion of the Γ_J matrix which pertains to downward transitions, as follows:

$$\gamma_{i,j} = \frac{2J_i + 1}{2J_j + 1} \gamma_{j,i} \exp\left(\frac{-\beta \Delta E_{i,j}}{k_b T}\right) \quad (2.10)$$

Finally, Martinsson and co-workers [50] introduce an approximation that became conventionally adopted in most MEG linewidth models. Its adoption stems from the symmetrical nature of the Raman intensities where the elastic isotropic Γ_J contributions do not vary much from the inelastic anisotropic contribution of Γ_{J+2} . This justification holds even more strongly at high temperature, and the total collisional linewidth Γ can be expressed based on a random phase approximation (RPA) formulation [50] [51] commonly used for Q-branch measurements.

$$\Gamma_{J''} = \frac{1}{2} (\Gamma_J + \Gamma_{J+2}) \quad (2.11)$$

The measurement of Raman linewidth through direct analysis of individual rotational transitions yields greater accuracy when contrasted with Q-branch approximations. Determining S-branch Raman linewidths involves evaluating the rate of coherence decay by systematically introducing delays to the probe pulse and monitoring the Rotational Coherent Anti-Stokes Raman Scattering (CARS) signal, as detailed in multiple references [52], [53], [54], [55], and [56]. Applying

this widely established technique is followed by fitting an exponential decay function to the time trace, yielding the coherence decay time constant ($\tau_{CARS,J''}$). The rotational Raman Lorentzian linewidth (FWHM) can then be extracted using Eq. 2.12, where c represents the speed of light:

$$\Gamma_{J'} = \frac{1}{2\pi c \tau_{CARS,J'}} \quad (2.12)$$

2.6 Pressure Broadening

Fs/ps CARS is dependent upon pressure through collisional linebroadening. The linewidth of isolated transitions is inversely related to the dephasing rate of each transition as shown in Eq. 2.12 and scales with pressure as given by Eq. 2.13 [30, 57]:

$$\Gamma_{J'}(p) = p \Gamma_{J'}(p = 1 \text{ atm}) \quad (2.13)$$

Extending this measurement technique to reacting flows, however, requires knowledge of the major species concentration in the dynamic, reacting environment. This is due to the fact that line broadening of a particular species depends not only upon pressure but also on the collisional partners present within the sample. For example, for a mixture of N_2 , O_2 , and CH_4 , the full collisionally broadened linewidth of N_2 as described by [30] is given by:

$$\Gamma_{tot,N_2} = x_{N_2} \Gamma_{N_2-N_2} + x_{O_2} \Gamma_{N_2-O_2} + x_{CH_4} \Gamma_{N_2-CH_4} \quad (2.14)$$

where x_i represents the mole fraction of each species and Γ_{N_2-i} represents the line broadening contribution of N_2 due to collisions with species i . Therefore, the relative concentration of major species must be known to accurately quantify pressure using fs/ps CARS in a reacting gas.

2.7 Proposed Dual-Probe CARS Setup

The proposed dual-probe CARS setup employs the same two femtosecond (fs) pulses described previously in addition to two probes. One probe employed at an early delay (0-5 ps) is used to measure temperature and one at later probe delay, selected based on the Raman dephasing time of the species observed as well as the pressure range of interest, is used to quantify pressure. Because both probe pulses are generated using the same incident pulse, temperature, species, and pressure may be quantified “instantaneously” with a temporal precision of ~ 100 ps.

In order to create the second probe, a stimulated Raman scattering (SRS) process is explored. Using SRS, one could obtain wavelengths that are directly not obtainable with conventional commercial lasers. Pumping non-linear solid-state materials such as diamond, nitrates, and tungstates with a high-power picosecond (ps) pulse allows the laser wavelength (532 nm in our case) to be converted based on discrete and specific Raman Shifts (Ω_R, cm^{-1}) that is determined by the Raman spectra generated in a given non-linear crystal.

Examining the most effective commercially accessible options for Raman Shifting Crystals, including Barium Nitrate ($Ba(NO_3)_2$), Potassium Gadolinium Tungstate

($\text{KGd}(\text{WO}_4)_2$ - KGW), Barium Tungstate (BaWO_4), Strontium Tungstate (SrWO_4), and Strontium Molybdate (SrMoO_4), in the context of achieving efficient stimulated Raman scattering (SRS), this discussion explores various frequency conversion possibilities. The integral cross section for spontaneous Raman scattering for each crystal material is outlined in Table 2.2. The spontaneous integral Raman cross section serves as a proportional indicator of the expected SRS intensity, offering a basis for comparison among crystals under identical dimensions and pumping conditions. To facilitate a direct comparison, the Raman gain coefficient is reflected in peak intensity measurements, with diamond serving as the benchmark ($\Sigma_{int} \equiv 100$).

Crystal Material	Raman Shift (Ω_R, cm^{-1})	Integral Cross Section ($\Sigma_{int}, a.u.$)	Peak Intensity ($\Sigma_{peak}, a.u.$)	Reference
Diamond	1332.9	100	100	[58]
$\text{Ba}(\text{NO}_3)_2$	1048.6	21	63	[58]
CaNO_3	1086	54	25	[59]
$\text{KGd}(\text{WO}_4)_2$	901	50	35	[58]
$\text{KGd}(\text{WO}_4)_2$	768	59	37	[59]
$\text{Ba}(\text{WO}_4)_2$	925	52	64	[59]
SrMoO_4	921	50	41	[59]
LiIO_3	821	54	25	[59]

Table 2.2: Spontaneous Raman scattering parameters of relevant crystals

As Basiev *et al.* [58] and later Černý *et al.* [59] pointed out, $\text{Ba}(\text{NO}_3)_2$ is the crystal with one of the highest Raman gain coefficients (normalizing with respect

to diamond with $\Sigma_{int} = 100 \text{ a.u.}$ and $\Sigma_{peak} = 100 \text{ a.u.}$). The trade-off for a high output intensity is the high thermal effects and low damage threshold for $\text{Ba}(\text{NO}_3)_2$ (25 times smaller than KGW). Therefore, KGW is preferred also due to its optimality for ultrashort ps pulse compared to $\text{Ba}(\text{NO}_3)_2$ which performs better with ns pulses. The output wavelengths observed experimentally when pumping with a 532 nm Nd:YAG (30ps, 10Hz) and an energy of 40mJ are shown in Table 2.3. The efficiencies are estimated based on information provided by the manufacturer (EKSMA Optics).






Wavelength (nm)	Color	Raman Shift (cm^{-1})	Maximum Efficiency
507 nm		Anti-Stokes	30%
558 nm		1st Stokes	70%
588 nm		2nd Stokes	40%
621 nm		3rd Stokes	15%
658 nm		4th Stokes	>10%

Table 2.3: KGW output wavelengths

Preliminary experimental testing showed that the KGW produces concentric ring-shaped beams at five discrete wavelengths. This presents an experimental challenge due to the high divergence angle that the beams exhibit. Separation was not possible using a Pellin–Broca prism. However, filtering out all the wavelengths except for the first and second Stokes and then using another filter to separate those two showed promise. Again, the beams are still unusable without a proper collimation method. Alternatively, using the rings is possible by employing a USED CARS phase matching configuration. Ultimately, the goal for multi-color

generation is producing high-energy ps probe pulses that can be deployed at varying time delays, enabling measurement of T , x_i and p simultaneously. Thanks to the differences in wavelength, the wave-mixing CARS process will create frequency-separated signals that can be detected using a single spectrometer and camera setup.

2.8 Chapter Summary

This chapter covers theoretical framework for Q-branch fs/ps CARS. It shows the modeling approach and presents experimental methods pertaining to pressure measurements in a static pressure cell as well as providing a framework for future dual-probe experiments.

3 Impact of Gas Pressure on Q-branch fs/ps CARS

3.1 Expanding the Collisional Linewidth Model for fs/ps CARS Simulations

To improve the accuracy of the MEG model as a means to simulate collisional linewidths at variable temperatures, a non-linear least-squares Levenberg-Marquardt algorithm [60] is used to optimize the parameters of the model while considering experimental data for a wide range of temperatures. This approach replaces the ad hoc parameter manipulation sometimes performed by researchers. As a reminder, the MEG model equation (Eq. 3.1) is as follows:

$$\gamma_{j,i} = p\alpha \left(\frac{1 - e^{-m}}{1 - e^{-mT/T_0}} \right) \left(\frac{T_0}{T} \right)^n \left(\frac{1 + \frac{aE_i}{k_b T \delta}}{1 + \frac{aE_i}{k_b T}} \right)^2 \exp \left(\frac{-\beta \Delta E_{i,j}}{k_b T} \right) \quad (3.1)$$

In this investigation, collisions involving diatomic molecules are considered. The species-specific constant factor a initially determined for N_2 is based on the effective collision duration, which is proportional to the reduced mass of the colliding molecules and the square of the closest approach distance [61]. It has been observed that linewidths predicted using the MEG model show limited sensitivity to variations in the value of a [62]. As a result, a value of 1.5 has been customarily used for N_2 - N_2 [62, 63], N_2 - H_2O [62], O_2 - O_2 [49, 63], O_2 - N_2 [63] and CO - CO [49] collisions. However, in some studies, a value of 1.67 has been assigned to it for

O₂-O₂ collisions [64] and 2 for N₂-CH₄ collisions [65]. The remaining parameters— α , β , δ , m , and n —were allowed to vary during model optimization. In this study, a is generally fixed at 1.5 and a reference temperature (T_0) of 295 K is utilized.

A comprehensive literature review is conducted to compile lists of linewidth datasets covering as wide range of temperatures as possible to the extent of the available data. This includes Q-branch measurements (which are approximations) and S-branch direct measurements. These datasets span a wide range of temperatures, with some experiments repeating similar temperatures, particularly N₂-N₂ linewidths at ambient temperature has been reported in different forms at least in seven sources. To determine optimal model parameters. The current analysis encompasses the following datasets spanning 31 temperatures for N₂-N₂ linewidths, 26 temperatures for O₂-O₂ linewidths, 9 temperatures for N₂-O₂ linewidths and 11 temperatures for N₂-H₂. The algorithm aims to minimize the sum of squared residuals (SSQ) between the experimental datasets and predictions (Eq. 3.2) calculated using the MEG model to determine the best-fit parameters.

$$e_{resid} = \Gamma_{J_i, J_f}^{meas.} - \Gamma_{J_i, J_f}^{model} \quad (3.2)$$

$$SSQ = e_{resid}^2.$$

3.1.1 N₂-N₂

The N₂-N₂ experimental linewidth measurements used in this work are summarized in Table 3.1. Both S-branch and Q-branch results measured at 1 atm were included. To the author’s knowledge, this is a complete list of S-branch N₂-N₂

linewidths measured using time-domain collisional decay rates reported in the literature to date. Additionally, a selection of Q-branch indirect measurements are included. Rahn and Palmer’s N₂ Q-branch linewidths measured by inverse Raman spectroscopy are included here because their work was the foundation for the MEG model [41]. Direct state-to-state energy transfer rate measurements by Sitz & Farrow at 298 K were excluded because they are shown to fit better with the statistical polynomial energy-gap model (SPEG) model [66] compared to the MEG model. Furthermore, six other measurements at ambient temperature including more accurate S-branch measurements are preferred to use as an initial benchmark for this temperature condition.

The pressure-broadened Raman linewidths have contributions from inelastic energy transfer between rotational states, re-orientation phase shifts due to collision-induced changes in the direction of the molecular axis, and vibrational dephasing [51] as shown in Eq. 3.3. However, the MEG model only accounts for inelastic collisional broadening [48], yielding some inherent errors especially at low J' .

$$\Gamma_{J_i, J_f} = \Gamma_{J_i, J_f}^{inelastic} + \Gamma_{J_i, J_f}^{reorient.} + \Gamma_{J_i, J_f}^{vib} \quad (3.3)$$

The strategy for optimization presented here starts with the objective of running an initial iteration that allows all parameters to vary. The goal is to identify four optimal parameters for each of the 31 datasets independently and determine if any of the parameters have a temperature dependence. This approach entails optimizing the MEG fit parameters for each linewidth dataset separately and aims to

Table 3.1: N₂-N₂ linewidth datasets used in this work

Dataset (Method)	Temperatures [K]	Citations
1	80	Retter <i>et al.</i> (2022) [67]
2	120	Retter <i>et al.</i> (2022) [67]
3	160	Retter <i>et al.</i> (2022) [67]
4	200	Retter <i>et al.</i> (2022) [67]
5	294	Retter <i>et al.</i> (2022) [67]
6	294	Kliewer <i>et al.</i> (2012) [54]
7	295	Meißner <i>et al.</i> (2019) [52]
8 (Q-Branch)	295	Rahn & Palmer (1986) [41]
9	298	Miller <i>et al.</i> (2011) [55]
10 (Q-Branch)	300	Haller & Varghese (2020) [46]
11	395	Kliewer <i>et al.</i> (2012) [54]
12	495	Kliewer <i>et al.</i> (2012) [54]
13	500	Meißner <i>et al.</i> (2019) [52]
14 (Q-Branch)	500	Rahn & Palmer (1986) [41]
15	661	Kliewer <i>et al.</i> (2012) [54]
16 (Q-Branch)	730	Rahn & Palmer (1986) [41]
17	868	Kliewer <i>et al.</i> (2012) [54]
17	870	Meißner <i>et al.</i> (2019) [52]
18	1000	Meißner <i>et al.</i> (2019) [52]
19 (Q-Branch)	1000	Rahn & Palmer (1986) [41]
20	1116	Kliewer <i>et al.</i> (2012) [54]
21	1200	Meißner <i>et al.</i> (2019) [52]
22	1400	Meißner <i>et al.</i> (2019) [52]
23	1466	Kliewer <i>et al.</i> (2012) [54]
24 (Q-Branch)	1500	Rahn & Palmer (1986) [41]
26	1650	Meißner <i>et al.</i> (2019) [52]
27 (Q-Branch)	1700	Lavorel <i>et al.</i> (1994) [68]
28	1750	Meißner <i>et al.</i> (2019) [52]
29	1900	Meißner <i>et al.</i> (2019) [52]
30 (Q-Branch)	2080	Lavorel <i>et al.</i> (1994) [68]
31 (Q-Branch)	2400	Lavorel <i>et al.</i> (1994) [68]

avoid conflating uncertainties and systemic errors from different literature sources employing different experimental techniques and modeling methodology. This ap-

proach offers insights into the optimal parameters across a range of temperatures.

For this analysis with n set to -0.5. The results demonstrate minimal variation in the values of δ and m as shown in Fig. 3.1. Consequently, these parameters are assigned their average values (Eq. 3.4) with the reported uncertainties here being two standard deviations determined from each fit matrix containing 31 values.

$$\begin{aligned}\bar{\delta} &= 1.37797 \pm 0.992 \\ \bar{m} &= 0.13643 \pm 0.00266\end{aligned}\tag{3.4}$$

In contrast, the parameter α varies with temperature following a power law dependence, with a coefficient of determination (R^2) value of 0.99. An empirical power law in the form of $\alpha = a \left(\frac{T_0}{T}\right)^b$ may be used to model this relationship. The parameter β also shows a moderate temperature dependence, supported by a power law fit that yields a lower R^2 value of 0.427. These parameter fits are visualized in Fig. 3.1. After fixing m and δ to the averages reported previously and incorporating the $\left(\frac{T_0}{T}\right)^b$ temperature dependence of α into n , α takes in the coefficient of the fit and n becomes as follows (Eq. 3.5):

$$\begin{aligned}\alpha &= 0.02132 \\ n &= 0.409542\end{aligned}\tag{3.5}$$

After modifying n , re-optimization shows that only the parameter β varies with temperature, and it is best described by either of the three statistical relationships in Eq. 3.6 depending on which dataset is considered as “truth” for ambient

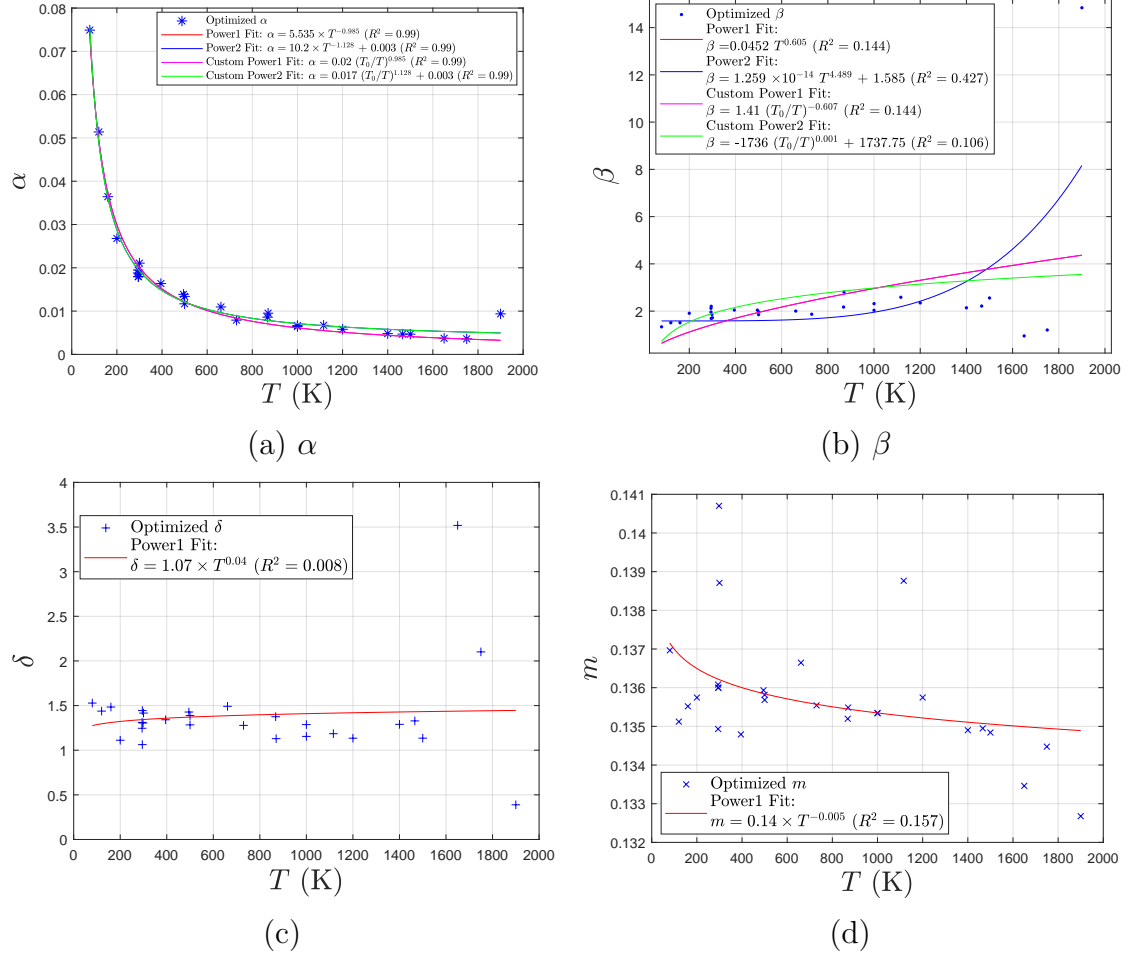


Figure 3.1: Initial MEG model parameter optimization (α , β , δ , and m) with fixed: $n = -0.5$, $a = 1.5$, and $T_0 = 295\text{K}$

temperatures (295 – 300 K) N₂-N₂ linewidths. Regardless of which relationship is used, the goodness of the fit remains similar, ranging from an R^2 of 0.85 to 0.92. The power law fit in the form of $a \cdot T^n + c$ is used to better encompass the steep increase in β from 80 K to around 295 K as described by Eq. 3.6 and illustrated in Fig. 3.2 where the fit with the highest R^2 is shown.

$$\begin{aligned}\beta &= -13.04 \times T^{-0.596} + 2.288 \\ \beta &= -12.43 \times T^{-0.5902} + 2.269 \\ \beta &= -9.51 \times T^{-0.511} + 2.352\end{aligned}\tag{3.6}$$

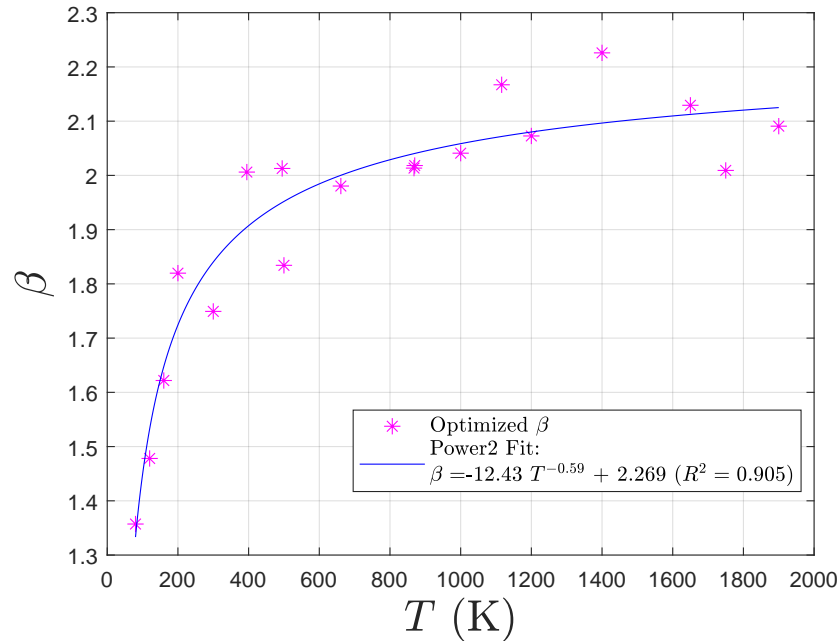


Figure 3.2: Optimized β , with the rest of the parameters fixed

In the last step of the optimization analysis, only S-branch data and one care-

fully selected Q-branch linewidth dataset acquired at ambient temperature (295-300 K) were considered for the purpose of conducting the β fitting procedure. This particular selection was made in light of substantial disparities observed in the reported Q-branch data, which deviate significantly from other experimental measurements. The omission of data from Lavorel *et al.* and high temperature data from Rahn & Palmer was primarily motivated because they fit rotational linewidths within the Q-branch spectra. When compared to the fitting of purely rotational linewidths, this approach inherently results in larger error. This methodological difference led to average disagreement of up to 20% when contrasted with more recent S-branch measurements. For instance, when examining two similar temperature conditions (1750 K as measured by Meißner *et al.* and 1700 K by Lavorel *et al.*), significant discrepancies of over 100% are apparent for specific J levels. These discrepancies, while varying in magnitude between J , consistently exhibit a high level of disparity, and led to sub-par MEG optimization if included.

With the fitting procedure confined to this selection of linewidth datasets, a new model, referred to as the Modified Exponential Gap-Power Fit (MEG-PF) model, is proposed. This model presents an improved match to experimental linewidths across a range of temperatures. These results are illustrated across different temperature ranges in Figures 3.3a, 3.3b, 3.4a, 3.4b, 3.5a, and 3.5b. The error bars on these plots primarily reflect uncertainties from the published sources. In some instances, the authors estimate uncertainties globally for all the data, often within the range of 3-6%.

Fig. 3.3a displays a comparison between Retter *et al.*'s dataset and the MEG-

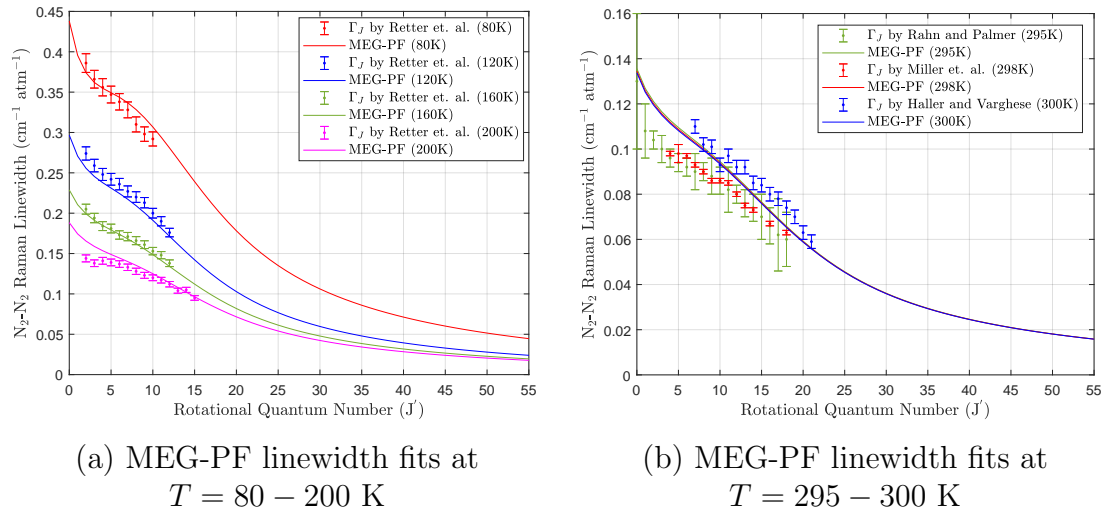


Figure 3.3: Examples of MEG-PF linewidth fits at cold and ambient temperatures

PF model, revealing the model's good performance at low temperatures. Figure 3.3b showcases a set of fits at ambient temperature. This exhibits a notable deviation from Miller *et al.*'s data, where the curve falls completely outside their reported error. In fact, it is essential to emphasize that, particularly at ambient temperature, discrepancies among the six analyzed datasets are primarily due to the unclear methodology for calculating or estimating uncertainties. Such ambiguity hinders the formation of conclusive statements regarding the validity of each measurement. Additionally, it should be noted that this discrepancy in N_2-N_2 collisional linewidths at 294 K has long been recognized within the scientific community [44] because of issues pertaining to the temperature correction ratio ($\frac{T}{T_0}$) approaching 1. Consequently, it is advisable to consider employing 300 K as opposed to 294 K with the new model when considering ambient conditions to attain better agreement, as exemplified in Figure 3.3b, rather than relying on a cus-

tomized model solely tailored to address issues at 294 K as some other researchers suggest.

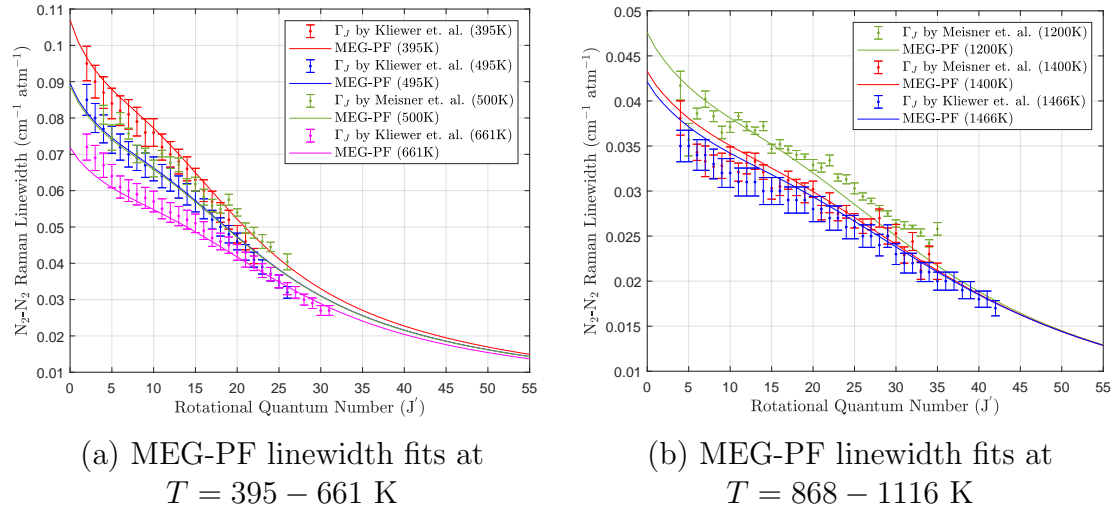


Figure 3.4: Examples of MEG-PF linewidth fits at mid-range temperatures

Fig. 3.5b and Fig. 3.5a show a comparison between MEG-PF and linewidth measurements reported by Meißner *et al.* and Kliewer *et al.* at higher temperatures, good agreement is observed with an average difference, between model and experimental data at each rotational state, of around 5.5%. However, noise in the Meißner *et al.* data seen in the 1900 K linewidths (Fig. 3.5b), especially at low J , is expectedly not captured by MEG-PF.

The variation in linewidth error as a function of temperature is shown in Fig. 3.6. The error is defined based on the average absolute difference between experimental data and model predictions for each J as per Eq. 3.7. This disagreement

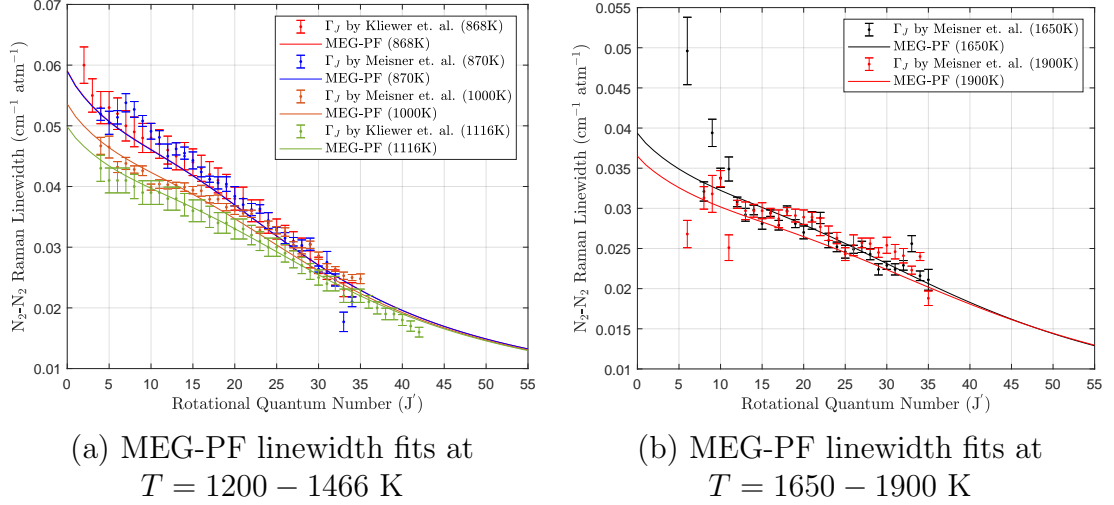


Figure 3.5: Examples of MEG-PF linewidth fits at elevated temperatures

is presented as a percentage by normalizing by the experimental data.

$$\overline{\Delta\Gamma_J} = Avg\left[\frac{|\Gamma_J^{MEG-PF} - \Gamma_J^{Exp}|}{\Gamma_J^{Exp}}\right] \quad (3.7)$$

Use of the new model generated in this work generates an average disagreement with the data ($\overline{\Delta\Gamma_J}$) that falls below the experimental uncertainty of the majority of linewidths. Fig. 3.6 suggests that the error does not vary as a function of temperature. Only three ambient temperature linewidth datasets are shown here (the ones with <10% error) while the others are omitted because they show large errors (15-20%). This suggests that further work is necessary to validate which measurements are the "truth" at ambient temperature. For the rest of the temperatures, error seem to be independent of temperature, suggesting that MEG-PF captures the linewidths well within the uncertainty of the experimental data.

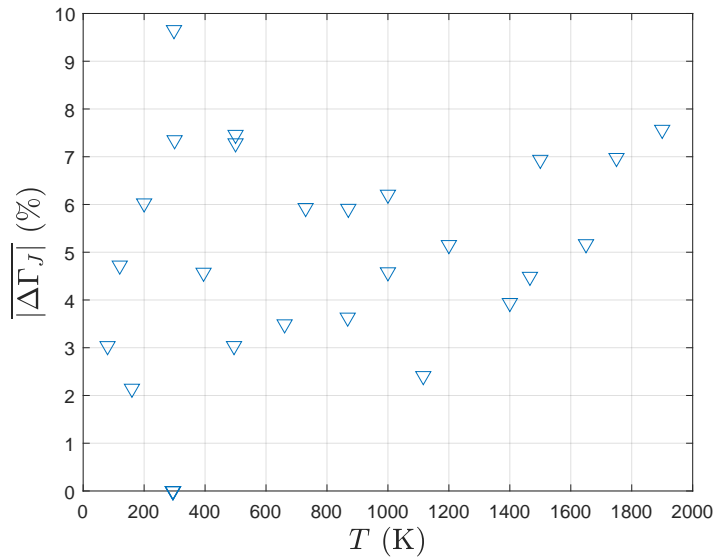


Figure 3.6: Disagreement between experimental data and MEG-PF in a sample of linewidth datasets

Table 3.2 contains a comparison between model results and experiments when using the model parameters in each row. The last column represent average percent disagreement in this work compared to that published by Linne *et al.* which only considered the dataset published by Kliewer et al [54]. Our newly implemented model shows a small increase in $\overline{\Delta\Gamma_J}$ likely due to the consideration of significantly more experimental linewidths.

The previous approach, which involves assigning a temperature-dependent function to β , has shown significant advantages over the alternative method of using a single set of parameters for all temperature conditions. In fact, a best-fit approach resulted in a higher average disagreement of 7.97%, and notable errors in certain instances, ranging from 8% to approximately 15%, as illustrated in Figure 3.7.

Table 3.2: MEG-PF model parameters summary for N₂-N₂ collisions

Citation	α	β	δ	n	m	$\overline{\Delta\Gamma_J}$
Linne et al. [44]	0.0283 ± 0.002	1.942 ± 0.03	1.259 ± 0.07	0.5	0.1360 ± 0.0001	3.3%
This work	0.02132 ± 0.00001	$-13.04T^{-0.596} + 2.288$	1.37798 ± 0.48	0.4095 ± 0.0001	0.1358 ± 0.0016	4.85%

This underscores the fact that using the same parameters for all temperatures or relying on previously reported MEG parameters, as other researchers have done, can lead to substantial error, particularly in the context of CARS thermometry and pressure measurements. Using 1.5 and 295 K for a and T_0 , respectively, the best-fit optimized parameters and the associated error determined when optimizing all of the linewidth datasets simultaneously are summarized in Fig. 3.7.

**Best Fit Optimized
MEG Parameters:**

- $\alpha = 0.01736$
- $\beta = 1.4644$
- $\delta = 1.575$
- $m = 0.9231$
- $n = 0.926$

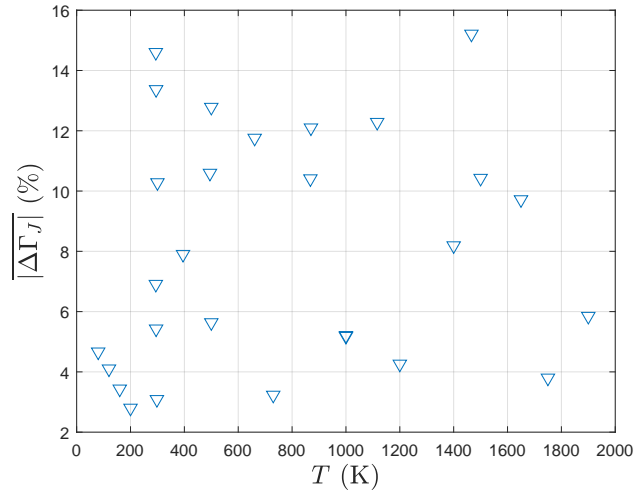


Figure 3.7: List of MEG parameters and the associated disagreement between experimental data and MEG model for the entire compilation of datasets

3.1.2 O₂-O₂

In addition to incorporating N₂-N₂ self-broadened linewidths, it is necessary to consider additional collisional partners and species, including O₂, for combustion environments. O₂ serves as a key indicator of the progress and efficiency of any combustion process. Similar to nitrogen (N₂), the ground electronic state of oxygen ($^3\Sigma g^-$) possesses electron spin angular momentum, enabling the description of linewidths based on the initial and final rotational state [69]. However, the O₂ data exclusively encompasses odd rotational levels, with the absence of even levels owing to the zero nuclear spin of the oxygen atom [69].

The O₂-O₂ linewidth sources considered in this study are summarized in in Table 3.3. The provided data include both S-branch and Q-branch experiments conducted under atmospheric pressure conditions and at various temperatures. To the best knowledge of the author, this compilation constitutes a comprehensive tabulation of Q-branch and S-branch O₂-O₂ linewidths documented in existing literature. Notably, until very recently, there was an absence of S-branch data for collisional O₂ self-broadening linewidths, with Miller *et al.* and Hölzer *et al.*'s work being the only exceptions. Researchers, up until recently, had to rely on Q-branch collisional parameters in lieu of S-branch data. In most instances, the S-branch Raman linewidth differ greatly from Q-branch data which has served as the standard thus far. Therefore, an improvement in temperature and concentration accuracy from CARS evaluations by application of the S-branch Raman linewidths is expected. In order to extract optimal parameters, Miller *et al.*'s and Hölzer *et*

Table 3.3: O₂-O₂ linewidth datasets used in this work

Dataset	Temperatures [K]	Citations
1	107	Bérard <i>et al.</i> (1983) [70]
2	115	Bérard <i>et al.</i> (1983) [70]
3	182	Bérard <i>et al.</i> (1983) [70]
4	207	Bérard <i>et al.</i> (1983) [70]
5	234	Bérard <i>et al.</i> (1983) [70]
6	293	Bérard <i>et al.</i> (1983) [70]
7	293	Nordstrom <i>et al.</i> (2015) [71]
8	295	Hölzer <i>et al.</i> (2021) [72]
9	295	Ouazzany <i>et al.</i> (1987) [73]
10	295	Millot <i>et al.</i> (1992) [74]
11	295	Jammu <i>et al.</i> (1966) [69]
12	298	Miller <i>et al.</i> (2011) [55]
13	338	Bérard <i>et al.</i> (1983) [70]
14	366	Bérard <i>et al.</i> (1983) [70]
15	377	Bérard <i>et al.</i> (1983) [70]
16	446	Millot <i>et al.</i> (1992) [74]
17	500	Hölzer <i>et al.</i> (2021) [72]
18	769	Millot <i>et al.</i> (1992) [74]
19	870	Hölzer <i>et al.</i> (2021) [72]
20	990	Millot <i>et al.</i> (1992) [74]
21	1000	Hölzer <i>et al.</i> (2021) [72]
22	1200	Hölzer <i>et al.</i> (2021) [72]
23	1317	Millot <i>et al.</i> (1992) [74]
24	1350	Millot <i>et al.</i> (1992) [74]
25	1400	Hölzer <i>et al.</i> (2021) [72]
26	1650	Hölzer <i>et al.</i> (2021) [72]
27	1750	Hölzer <i>et al.</i> (2021) [72]
28	1900	Hölzer <i>et al.</i> (2021) [72]

al.'s most recent work are primarily used for the current study [72], which present more accurate measurements compared to the earlier work by the same group [75].

Initial iterations allowed α , β , δ , m and n to change and compared when a was allowed to change or when it was fixed to either 1.5 or 1.67. The initial guess in

the algorithm was set based on Beyrau *et al.*'s suggested MEG parameters [64]. The optimization led to good agreement and an average error of under 10% except for the datasets at temperatures 1650 K and 1750 K which show errors in the range of 14–15%. This deviation is caused by variation in the experimental data and cannot be compensated for by adjusting a as demonstrated in Fig. 3.8 which shows the error when a is allowed to float and when a is set equal to 1.67. This has shown little difference in the overall linewidth error and the average disagreement for both is virtually the same ($\sim 9.3\%$).

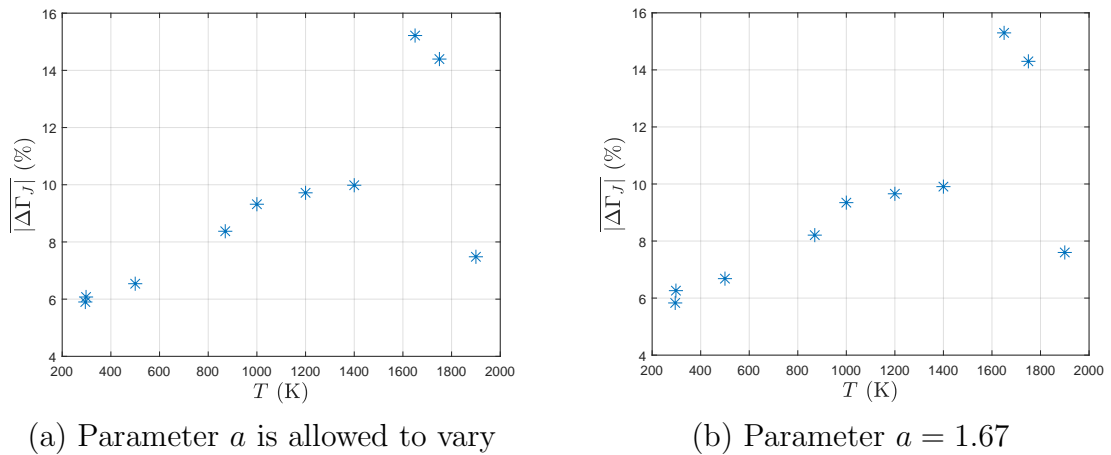


Figure 3.8: Disagreement plot comparison between fixed a vs. floating a in the NLSQ optimization

The linewidth fits generated using the parameters from the second row in Table 3.4 are visually represented in Figures 3.9a and 3.9b. The summarized results, detailed in Table 3.4, showcase the outcomes obtained with a fixed a value of 1.67 and a variable a . Despite efforts to enhance the fit by re-optimizing and excluding datasets at 1650 K and 1750 K, no substantial improvement was observed, and

therefore those results are not shown here.

The maximum disagreement between measurement—excluding the 1650 K and 1750 K datasets—and MEG model was approximately 10%, aligning with earlier findings where only the datasets at 1650 K and 1750 K exhibited an average disagreement exceeding 10%. The difficulty with fitting high temperature linewidths provided by Hölzer *et al.* might be due to their RCARS signal decay fitting strategy with respect to probe delay. Notably, their attempts to simultaneously fit fast decay regions (low temperature) and slow decay regions (high temperature) led them to logarithmize their data, applying a relative weight on their RCARS intensity at late delays. This is potentially the source of uncertainty and inconsistency in their high-temperature data. This further underscores the ongoing necessity for determining high-fidelity O₂-O₂ linewidth data, ideally using techniques other than RCARS for comparison. The inherent limitations posed by low signal-to-noise ratios at elevated temperatures necessitate exploring alternative measurement methods to achieve more accurate and reliable results.

Table 3.4: MEG model parameters summary for O₂-O₂ collisions

Results	α	β	δ	n	m	a	$\overline{\Delta\Gamma_J}$
Opt. Param. 1	0.01472	1.32409	2.11748	0.10682	0.36727	0.54266	9.3%
Opt. Param. 2	0.01679	1.5971	1.32469	0.1153	0.3859	1.67	9.31%

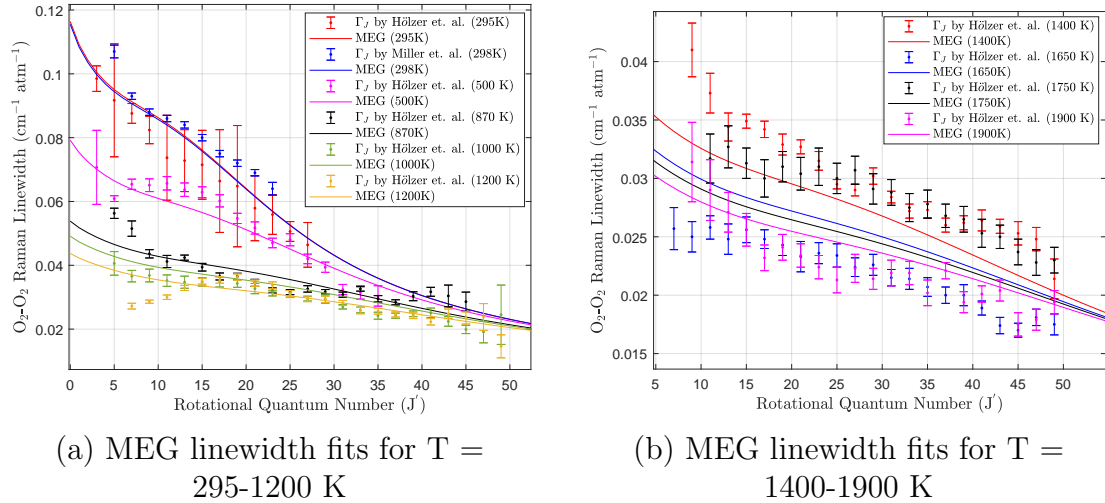


Figure 3.9: MEG linewidth fits for Hölzer *et al.* and Miller *et al.* measurements ($a = 1.67$)

3.1.3 N₂-O₂

While combustion processes entail a substantial consumption of O₂ within the reaction zone, the role of O₂ as a collision partner in shaping the N₂ Raman linewidth is sometimes overlooked in scaling law models. This omission occurs when computing theoretical spectra using only the self-broadened N₂-N₂ Raman linewidth and can lead to inaccuracies in temperature assessments. This concept extends to fuel molecules such as CH₄, C₂H₄, or H₂ (discussed in the following section). In air-fed processes, O₂ is potentially an influential molecule affecting N₂, given its initial presence at a concentration of approximately 21%, although to a lesser degree than H₂. As of the current date, Meißner *et al.* and Retter *et al.* are the only works that have quantified the N₂-O₂ S-branch Raman linewidths, with the latter focusing on measurements at sub-atmospheric temperatures, as

summarized in Table 3.5. Incorporating these linewidths into the MEG model holds the potential of enhancing the accuracy of CARS when utilizing nitrogen as a marker molecule for thermometry.

Table 3.5: N₂-O₂ linewidth datasets used in this work

Dataset	Temperatures [K]	Citations
1	80	Retter <i>et al.</i> (2022) [67]
2	120	Retter <i>et al.</i> (2022) [67]
3	160	Retter <i>et al.</i> (2022) [67]
4	200	Retter <i>et al.</i> (2022) [67]
5	294	Retter <i>et al.</i> (2022) [67]
6	295	Meiβner <i>et al.</i> (2019) [52]
7	500	Meiβner <i>et al.</i> (2019) [52]
8	870	Meiβner <i>et al.</i> (2019) [52]
9	1400	Meiβner <i>et al.</i> (2019) [52]
10	1650	Meiβner <i>et al.</i> (2019) [52]
11	1900	Meiβner <i>et al.</i> (2019) [52]

However, using a compilation of reported linewidths from different sources to extract accurate MEG model parameters poses a challenge again due to measurement discrepancies particularly observed at low J' . For example, examining linewidths reported by Meiβner *et al.* and Retter *et al.* at similar temperatures (295 K and 294 K respectively) show significant disagreement not fully contained within the reported uncertainties ranges. Consequently, lumping all of the 11 datasets together for the optimization process to determine one set of parameters can automatically lead to sub-optimal parameters as the algorithm will favor providing the best fits for most of the data. Using all the 11 N₂-O₂ S-branch linewidth datasets, the optimization process yields parameters that, when applied, result in an average error of 6.87%. The scatter of the disagreement for each individual

dataset along with the optimal parameters is shown in Fig. 3.10. The resultant fits are shown in Fig. 3.11a and 3.11b.

**Best Fit Optimized
MEG Parameters:**

- $\alpha = 0.01543$
- $\beta = 1.384$
- $\delta = 1.6381$
- $m = 1.023$
- $n = 0.9121$

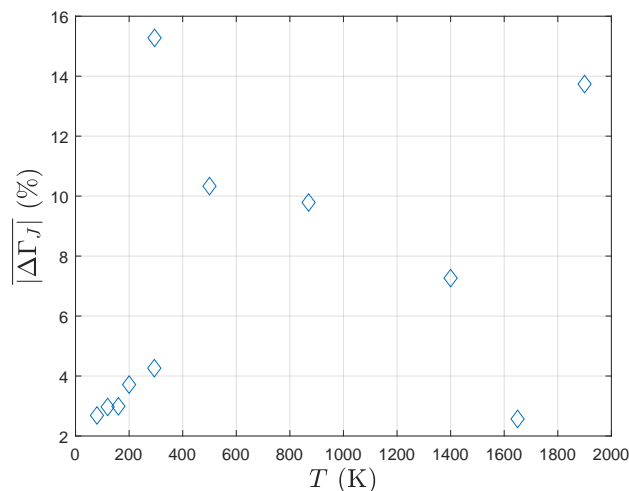
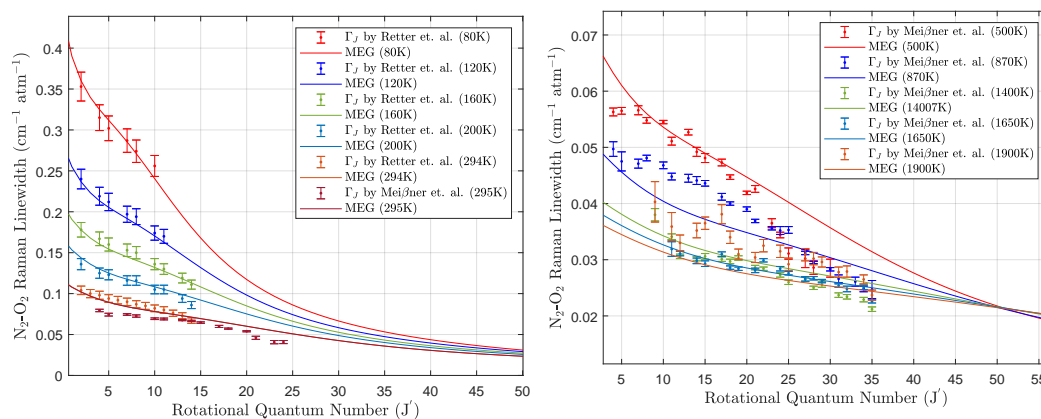


Figure 3.10: List of MEG parameters and the associated errors for the full dataset



(a) MEG linewidth fits for cold and ambient temperatures (80-295 K)

(b) MEG linewidth fits for elevated temperatures (500-1900 K)

Figure 3.11: MEG linewidth fits for the full dataset

Using only the N₂-O₂ S-branch linewidths reported by Meißner *et al.*, the opti-

mization process yields a disagreement of 7.4%. Using the same dataset excluding excluding the 1900 K (exhibiting a non-physical increase in line-broadening coefficients at $J' = 15$ and 17), optimization yields a disagreement of 5.45%. The optimized parameters and the associated errors are summarized in Tab. 3.6.

Table 3.6: MEG model parameters summary for N₂-O₂ collisions ($a = 1.5$)

Results	α	β	δ	n	m	$\overline{\Delta\Gamma_J}$
Full Dataset	0.01543	1.3839	1.6381	1.0227	0.91215	6.87 %
Mei β ner <i>et al.</i>	0.01492	1.64593	1.451151	1.551	0.94431	7.4 %
Mei β ner <i>et al.</i> (Ex. 1900 K)	0.01475	1.73505	1.34857	0.0638	0.21077	5.45 %

3.1.4 N₂-H₂

In the pursuit of developing an accurate linewidth model for the application of CARS thermometry and pressure measurements in a combustion environment, particularly for studying H₂/Air flames, careful consideration of N₂-H₂ line-broadening coefficients is imperative as they vary significantly from N₂-N₂ and N₂-O₂ linewidths. The inclusion of N₂-N₂, N₂-O₂, and N₂-H₂ interactions collectively will significantly enhance the accuracy of the calculated Raman linewidths. This improvement is anticipated based on previous research, which demonstrated an approximately 2% increase in predicted temperatures when analyzing N₂ Rotational CARS spectra obtained from the product gases of a fuel-rich 20% H₂ flame [76]. Notably, this increase was attributed to the inclusion of N₂-H₂ collisions.

Furthermore, Bohlin *et al.* notes that neglecting the effects on the N₂ spectral lines in an environment dominated by collisions with H₂ could result in an underes-

timation of predicted temperatures from N₂ RCARS by 6%–7% [77]. Consequently, this section aims to expand the linewidth model to capture these contributions. We base this work on existing experimental data from literature, similar to the previous sections. The experimental line-broadening experimental datasets measured at various temperatures are summarized in Table 3.7.

Table 3.7: N₂-H₂ linewidth datasets used in this work

Dataset	Temperatures [K]	Citations
1	77	Joubert <i>et al.</i> (2008) [78]
2	294	Bohlin <i>et al.</i> (2012) [77]
3	298	Joubert <i>et al.</i> (2022) [78]
4	395	Bohlin <i>et al.</i> (2008) [77]
5	440	Joubert <i>et al.</i> (2008) [78]
6	495	Bohlin <i>et al.</i> (2012) [77]
7	580	Joubert <i>et al.</i> (2008) [78]
8	661	Bohlin <i>et al.</i> (2012) [77]
9	868	Bohlin <i>et al.</i> (2012) [77]
10	1116	Bohlin <i>et al.</i> (2012) [77]
11	1466	Bohlin <i>et al.</i> (2012) [77]

N₂-H₂ line-broadening coefficients have been calculated by multiple groups in the past, notably using the semiclassical Robert–Bonamy model as reported by Dhyne *et al.* [79]. The calculations determined isotropic Q-branch and anisotropic S-branch linewidths. However, few tabulated experimental measurements are published. Among those are one experimental Q-branch set of coefficients reported by [80] for 77 K and 298 K. The same group expanded their work in [81] to add measured linewidths at 440 K and 580 K. Here, the compiled dataset published by Joubert *et al.* [78] is considered. Unfortunately, these linewidths measured by stimulated Raman loss spectroscopy exhibit large error bars and non-physical be-

havior. Gómez *et al.* attributed the substantial error bars observed at the lowest and highest J' values to the low signal intensity and poor signal-to-noise ratio. Specifically, reported error bars reach up to 20% at low temperatures and low J' levels, with some instances showing error bars as high as 90% at elevated temperatures (440 and 580 K). Therefore, to ensure the reliability of our analysis, this analysis exclusively utilize S-branch measurements available in the work of Bohlin *et al.* [77].

The optimization process yields an average error of 2.2% by comparing the MEG model with the Bohlin *et al.* experimental dataset. The total disagreement for each temperature and the optimal MEG model parameters are shown in Fig. 3.12 and the fits are shown in Fig. 3.13.

**Best Fit Optimized
MEG Parameters:**

- $\alpha = 0.016475$
- $\beta = 1.5381$
- $\delta = 1.1658$
- $m = -0.0232$
- $n = -0.05552$

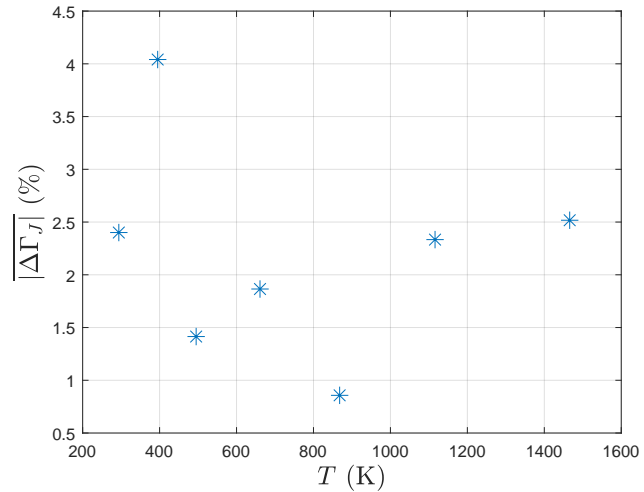


Figure 3.12: List of MEG parameters and the associated disagreement using Bohlin *et al.* measurements

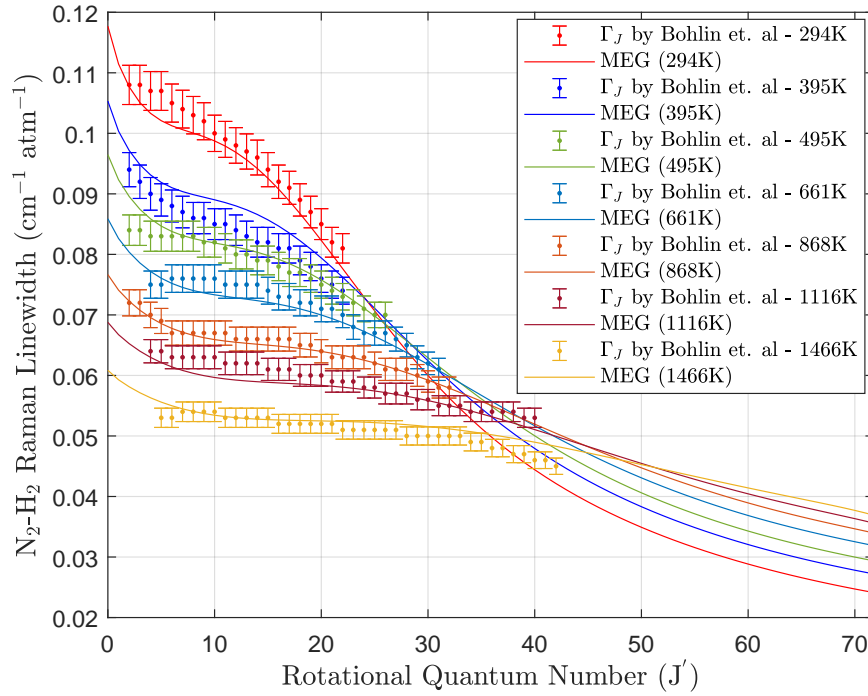


Figure 3.13: MEG linewidth fits for Bohlin *et al.* measurements

3.1.5 Total N₂ Collisional Linewidths

Following this work, the final fs/ps CARS spectral model now includes N₂-N₂, N₂-O₂, and N₂-H₂ line broadening effects calculated with the new MEG model parameters. The total N₂ collisional linewidth is determined using a species-specific weighted linear combination to determine the total N₂ collisional linewidth (Eq. 3.8), where x_i refers to the species mole fraction and $\Gamma_{J,J'}^{N_2-X}$ is the associated line broadening coefficient matrix:

$$\Gamma_{J,J'}^{N_2} = x_{N_2} \cdot \Gamma_{J,J'}^{N_2-N_2} + x_{O_2} \cdot \Gamma_{J,J'}^{N_2-O_2} + x_{H_2} \cdot \Gamma_{J,J'}^{N_2-H_2} \quad (3.8)$$

This modified collisional linewidth calculation method for N_2 was used to investigate Q-branch CARS sensitivity to pressure as well as to simulate the CARS spectral response for a hydrogen/air diffusion flame in the following sections.

3.2 Ro-vibrational fs/ps CARS Sensitivity to Pressure and Species Concentration

To accurately quantify pressure in a reacting flow, a sensitivity analysis is necessary to examine the impact of varying probe delay across an extensive pressure range (1-12 bar). This strategy entails integrating O_2 and N_2 spectral features in frequency, determining the relative intensity and then investigating the change in the ratio at different pressures and probe delays. This exploration is conducted on a controlled binary mixture of nitrogen (N_2) and oxygen (O_2), with respective mole fractions of $x_{N_2} = 0.785$ and $x_{O_2} = 0.215$. The simulation leverages the improved MEG model, as detailed in the previous section, to enhance the fs/ps CARS code accuracy. The ensuing analysis reveals noteworthy features, underscoring the interplay between the influence of pressure and that of probe delay on CARS signal characteristics.

Figure 3.14 shows simulated spectra corresponding to various pressures at both early and late probe delays. The timing of the probe is coordinated with the pump/Stokes pulses to avoid overlap at time zero, preventing the generation of a pronounced non-resonant background signal through the interference of the non-resonant four-wave mixing process. The $\tau = 3-5$ ps interval establishes a virtual minimum for an early probe to ensure a collision-free environment [82]. This tim-

ing choice also effectively eliminates the non-resonant background contributions, thereby enhancing the resonant signal associated with molecular transitions—a key advantage of the hybrid CARS technique.

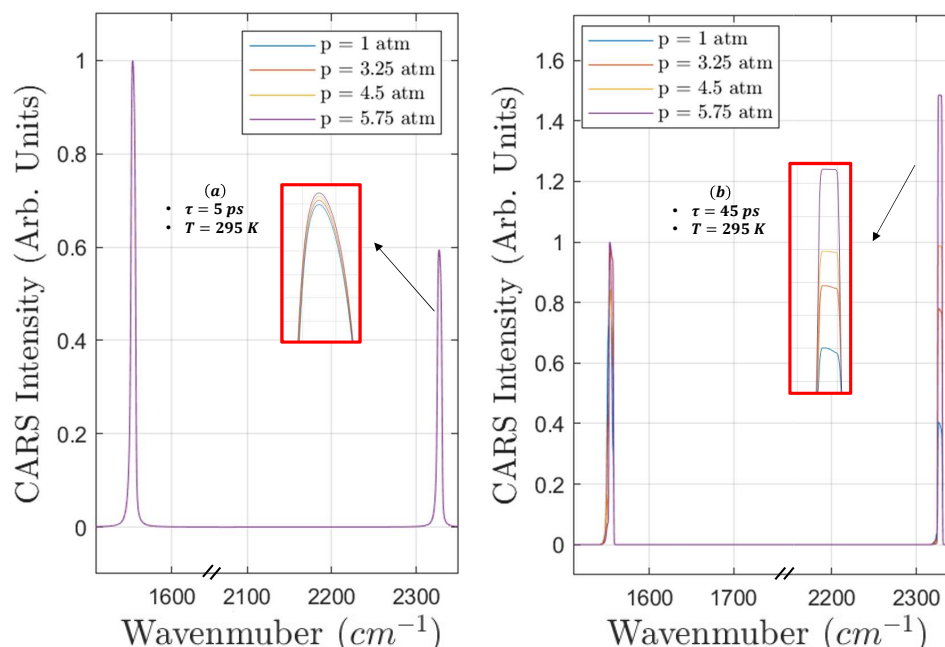


Figure 3.14: Vibrational Q-branch of N_2 and O_2 Raman spectra simulated at a sample of low- and high-pressures (a: at $\tau = 5$ ps — b: at $\tau = 45$ ps)

At $\tau = 5$ ps, the spectra display minimal changes with varying pressure (Fig. 3.14-a). In contrast, at $\tau = 45$ ps (Fig. 3.14-b), a consistent trend emerges, revealing an increase in the N_2 peak intensity with rising pressure (spectra normalized with respect to O_2). This behavior can serve as a marker for local pressure quantification in an N_2 - O_2 gas mixture. On a fundamental physical level, this trend suggests that similar variations in peaks can be anticipated in other mixtures involving fuels and combustion product molecules. The exploration of such variations

in other gas mixtures will be the focus of experimental investigations in Chapter 4.

Figure 3.15 shows a simulation of I_{O_2}/I_{N_2} ratio for an N_2 - O_2 gas mixture at a constant temperature of 295 K. The highest signal sensitivity to pressure is observed within the 40–55 ps probe delay range. This is illustrated by the sharp gradient in the contour plots: one displaying the absolute intensity ratio (Fig. 3.15a) and one the logarithmic intensity ratio (Fig. 3.15b) of O_2 to N_2 . The logarithmic-scale plot demonstrates that over this range of pressures the ratio of CARS signal intensities spans multiple orders of magnitude, indicating clearly a strong sensitivity to pressure. Additionally, it's worth noting that discernible pressure effects are observed as early as the 30 ps probe delay.

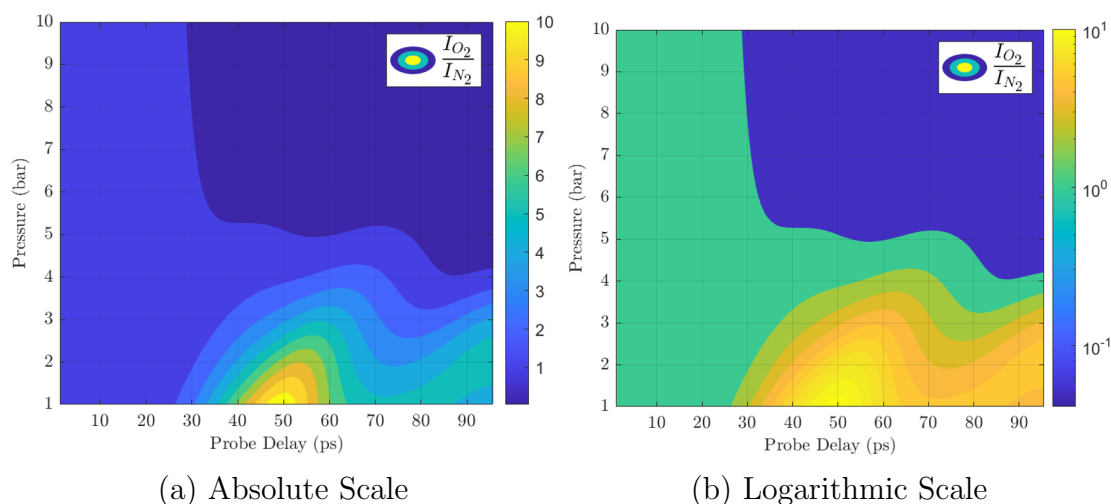


Figure 3.15: VCARS summed peak ratio ($\frac{I_{O_2}}{I_{N_2}}$) vs. pressure and probe delay for a constant N_2 - O_2 mixture at $T = 295$ K

The CARS signal response with pressure for a subset of probe delays is included

in Fig. 3.16. At an early probe delay of 5 ps, the CARS signal demonstrates virtually no sensitivity to collisional effects. Even at a 20 ps probe delay, only a minor variation in the $\frac{I_{O_2}}{I_{N_2}}$ ratio is observed from 1 to 4 bar. In contrast, the 30 and 45 ps probe delays exhibit substantial sensitivity to pressure variations. Both of these probe delays would be effective for capturing pressure variation within this pressure range, contingent upon the abundance of CARS signal. Furthermore, increasing probe delay indefinitely does not always provide a better pressure sensitivity as exemplified by the pressure dependence at $\tau = 90$ ps which shows significantly less of pressure response compared to the optimal 45 ps probe delay. It also displays an inflection point near $p = 2$ bar which introduces complications in interpreting experimental data using a probe delay of 90 ps instead of 45 ps.

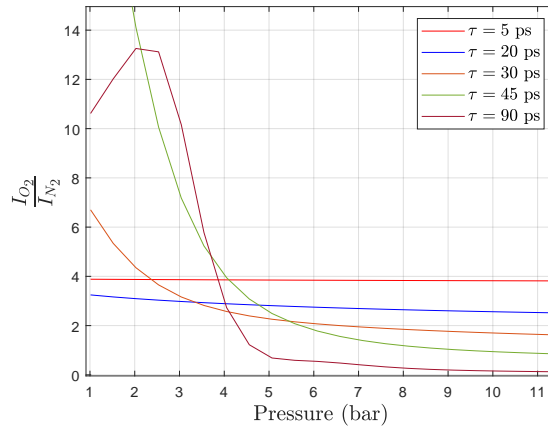


Figure 3.16: Variation of relative intensity CARS signal ($\frac{I_{O_2}}{I_{N_2}}$) for a probe delay sample (5, 20, 30, 45 and 90 ps)

The investigation, initially conducted at ambient temperature, is extended to explore a high-temperature scenario in Fig. 3.17 using the thermodynamic condi-

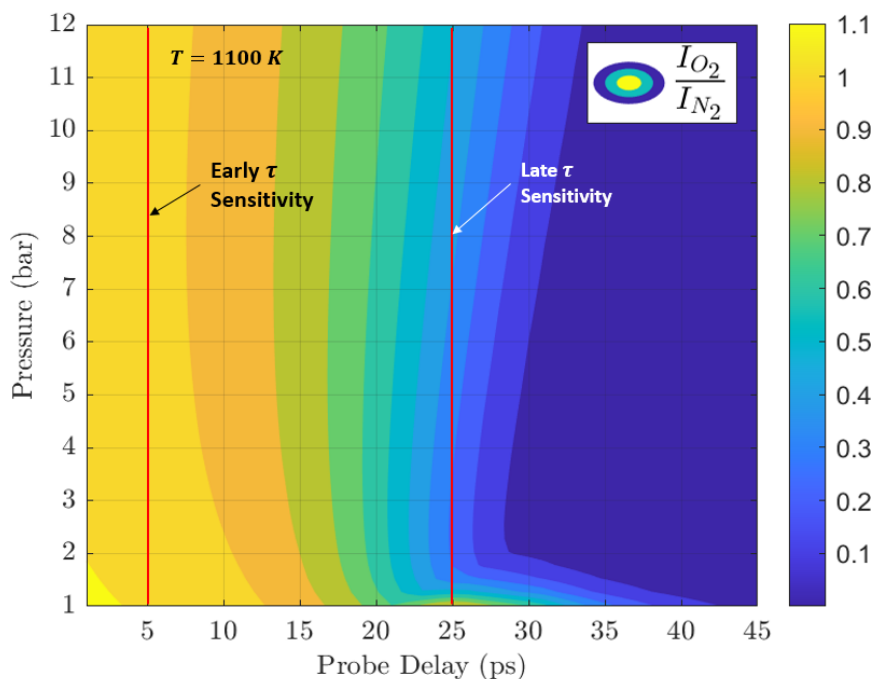


Figure 3.17: VCARS summed peak ratio variation ($\frac{I_{O_2}}{I_{N_2}}$) vs. pressure and probe delay for a constant N₂-O₂ mixture at $T = 1100\text{K}$

tions near the reaction zone of a diffusion flame. Simulating CARS spectra across a pressure range of 1-12 bar and at a temperature of 1100 K reveals a maximum pressure sensitivity at an earlier probe delay (25 ps) in comparison to ambient conditions (approximately 50 ps). This finding underscores the importance of judiciously selecting τ_{probe} , particularly in highly dynamic environments where gas temperature may span hundreds of Kelvins over a few millimeters, as observed across the reaction zone of a thin diffusion flame. Consequently, in addition to selecting an early probe delay (around 5 ps) for collision-free temperature and species measurements, several late probe delays spanning the range of 15–45 ps

should be selected if experimentally feasible to accommodate the expected range of temperatures. This selection strategy (one early and multiple late τ) becomes particularly pertinent for applications demanding precise pressure and temperature quantification in dynamic thermally fluctuating environments.

In addition to studying a constant concentration condition, the pressure sensitivity for a variety of N_2/O_2 concentrations was also explored. The results of this investigation at a temperature of 1100 K are shown in Fig. 3.18. The left panel, simulated at 5 ps, not only confirms a lack of pressure sensitivity at early probe delay but also demonstrates the capability for quantifying relative mole fraction. In contrast, the right panel of Fig. 3.18 highlights the high pressure sensitivity at late probe delays for various N_2 and O_2 mixtures. It exhibits a monotonic increase in $\frac{I_{O_2}}{I_{N_2}}$ starting from around 2 bar onward.

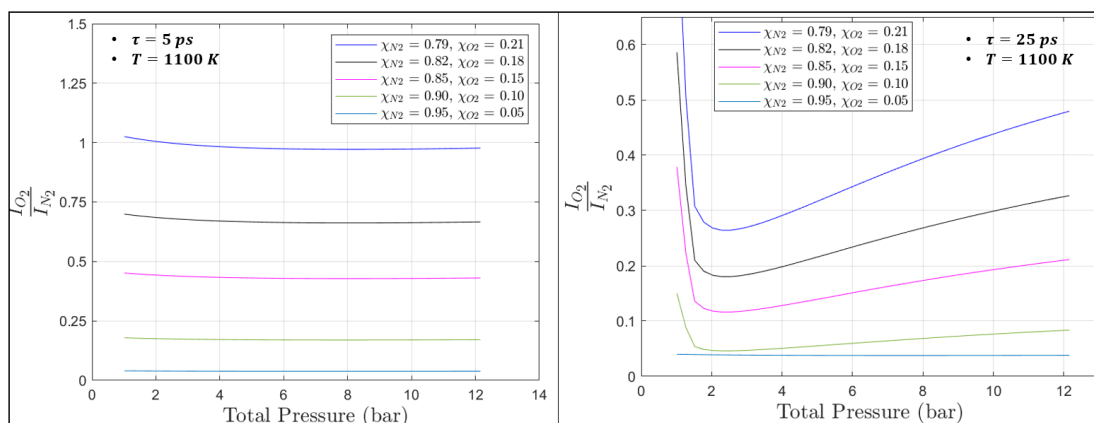


Figure 3.18: $\frac{I_{O_2}}{I_{N_2}}$ variation for a selection of N_2 - O_2 compositions

It is crucial to acknowledge, however, that the near-complete consumption of O_2 within a reaction zone prompts exploration into alternative molecules for mea-

suring pressure. This exploration forms the motivation for the experimental work presented in Chapter 4. For example, the relationship between N_2 and CH_4 Q-branch CARS features ($\frac{I_{CH_4}}{I_{N_2}}$) as a function of pressure is investigated for use in a fuel-rich reactant or product zone. Within the reaction or post-reaction zones, $\frac{I_{N_2}}{I_{CO_2}}$ or $\frac{I_{CO_2}}{I_{CO_2}}$ (comparing the two Fermi diad resonances) spectral feature ratios are considered.

3.3 fs/ps CARS Simulations Across a 1D Flame

To study the variations in spectral response across different locations in a combustion environment, a CH_4 /Air laminar flame with an initial fuel-side mole fraction of $x_{N_2} = 0.2$ and $x_{CH_4} = 0.8$, and an oxidizer-side composition of $x_{N_2} = 0.79$ and $x_{O_2} = 0.21$ was considered. The initial global strain rate is $450 \frac{1}{s}$. The pressure used is 2.5 atm. The Cantera simulation using the GRI 3.0 kinetic mechanism incorporates chemical kinetics, reactions, and transport processes along a 1-D axis spanning a length of 5.45 mm. At the center of Figure 3.19, the temperature and mole fraction results for this controlled flame are presented. The simulation involves 147 spectra corresponding to 147 locations along the flame axis, covering the 1-D line and incorporating all predicted N_2 and O_2 mole fractions. Sample spectra at six locations are shown in Fig. 3.19 displaying varying concentration and temperature conditions and set at a moderate pressure of 2.5 atm and utilizing a late probe delay of 25 ps to track pressure if local pressure within the flame varies. Furthermore, the CARS signal enables simultaneous experimental quantification of

temperature and mole concentration using another probe implemented at an early probe delay. The 1D simulation shown here may be used in the future to compare to experimental 1D CARS measurements at multiple probe delays in a counterflow diffusion flame at controlled pressures to demonstrate the use of Q-branch fs/ps CARS to quantify temperature, relative species, and pressure within a combustion environment.

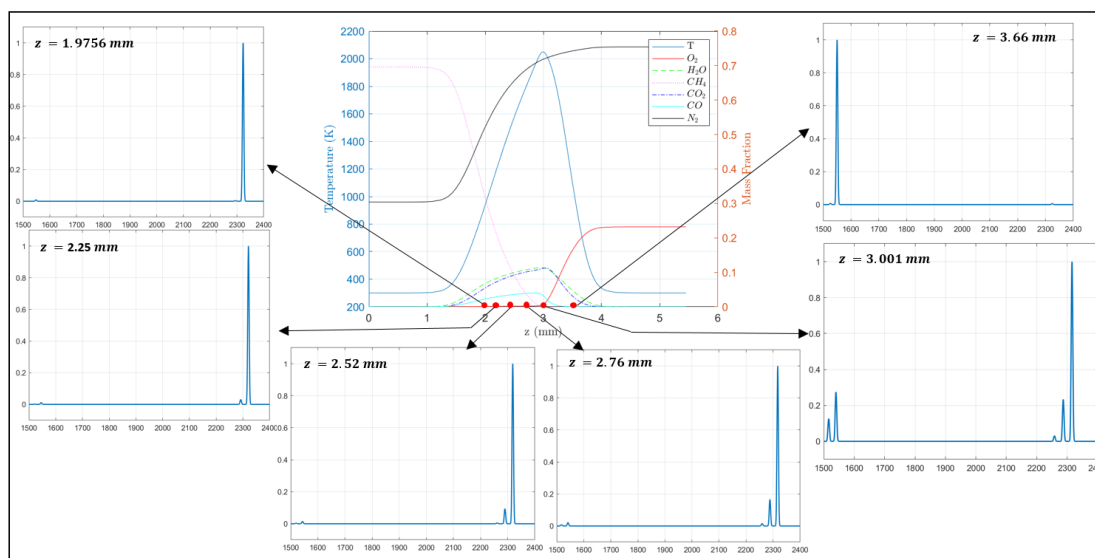


Figure 3.19: Vibrational CARS Raman Spectra of N_2 and O_2 at Various Locations in a Quasi One-Dimensional CH_4 /Air Diffusion Flame at $p = 2.5$ atm

3.4 Chapter Summary

In this chapter, the CARS spectral simulation code has been improved by refining and expanding the MEG collisional linewidth model with the goal of improving the accuracy of temperature and pressure measurements. The modifications entail

incorporating essential collisional partners for N_2 and O_2 simulations. The MEG-PF (MEG-Power Fit) model has been introduced to accommodate N_2 - N_2 collisions across both low and high-temperature regimes. Additionally, for collisions of O_2 - O_2 , N_2 - O_2 , and N_2 - H_2 , MEG model parameters were determined through optimization using a various experimental measurements from literature to ensure higher accuracy across a wide range of temperatures. Finally, the CARS spectra model has been integrated with the Cantera flame simulation to track pressure at variable temperature and species concentration.

4 Experimental Characterization of Q-branch fs/ps CARS at Elevated Pressures

This chapter presents experimental Q-branch fs/ps CARS measurements in a static high-pressure (1–10 bar) gas cell. Before the results are presented and discussed, the experimental approach, data processing details, and challenges encountered are first introduced.

4.1 Experimental Considerations

For an accurate conversion from the camera pixel to wavelength, the measurement resolution need to be quantified to distinguish between the various spectral features. Additionally, varying amounts of signal are anticipated due to the large changes required in probe delay and pressure conditions. To avoid camera sensor saturation in the cases of early probe delay and high pressure conditions, two signal attenuation techniques are explored: using neutral density filters (ND filters) and varying Stokes energy judiciously.

4.1.1 Measurement Resolution

To accurately identify the molecular vibrational transitions of each species investigated, it is necessary to calibrate the spectrometer's detection wavelength and

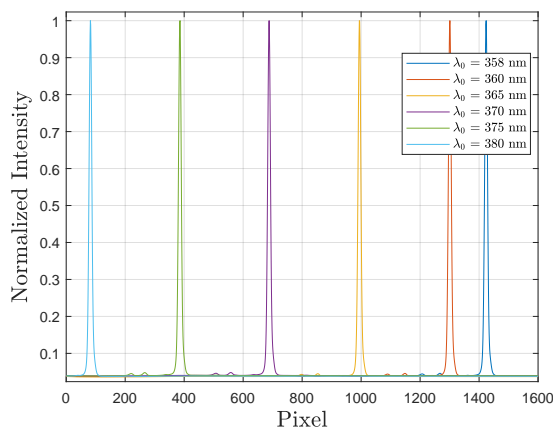


Figure 4.1: Raman Q-Branch N_2 spectra measured at variable λ_0

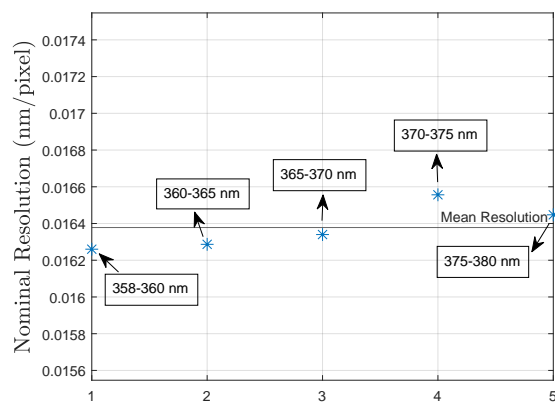


Figure 4.2: Calculated Experimental Resolutions

resolution used for fs/ps CARS detection (see Fig. 2.7 for more details). To accomplish this, the fundamental N_2 vibrational band centered at 2330 cm^{-1} was recorded at various spectrometer central wavelengths (λ_0)—358, 360, 365, 370, 375, and 380 nm—as illustrated in Figure 4.1. The highest resolution grating available (2400 grooves/mm) was employed. By shifting the spectrometer central wavelength by known amounts and observing the number of pixels the N_2 CARS vibrational band was displaced, the resolution could be determined across different wavelength ranges. Figure 4.2 shows the resulting resolutions and demonstrates, as expected, that resolution does not vary linearly with wavelength. The nominal resolution, $0.016378\frac{\text{nm}}{\text{pixel}}$, was used to estimate the wavelength axis for the current work. The wavelength axis (λ nm) was then converted to units of wavenumber to showcase the Raman shifts of the studied molecules. $\Delta\tilde{\nu}$ was calculated using the known probe pulse wavelength (λ_{probe}) as shown by Eq. 4.1. This step is important

for identifying peak positions for the different gas molecules.

$$\Delta\tilde{\nu} = 10^7 \cdot \left(\frac{1}{\lambda_{probe}} - \frac{1}{\lambda} \right) \quad (4.1)$$

4.1.2 Signal Attenuation

To accommodate for large changes over different pressures and probe delays, signal needs to be attenuated accordingly. Two methods are explored: using ND filters and varying Stokes energy.

4.1.2.1 Use of ND Filters

To address the stark difference in signal intensity at different pressures and probe delays, ND filters featuring variable optical densities were employed to attenuate the signal to avoid camera sensor saturation at times. However, this strategy proved ineffective due to the filters' transmission variability within a given wavelength range as shown in Fig 4.3 where the efficiency curves were measured using white-light source. Fig. 4.3 shows large variations in transmission for a spectrometer central wavelength of 375 nm. This poses a significant challenge, particularly in the context of comparing the relative intensity of CARS spectra from various molecules across a large bandwidth. The unequal impact of the variable filter efficiency across wavelengths introduces a significant source of errors and uncertainties unless the transmission for each filter is carefully accounted for, particularly when relying on peak ratios for precise pressure quantification.

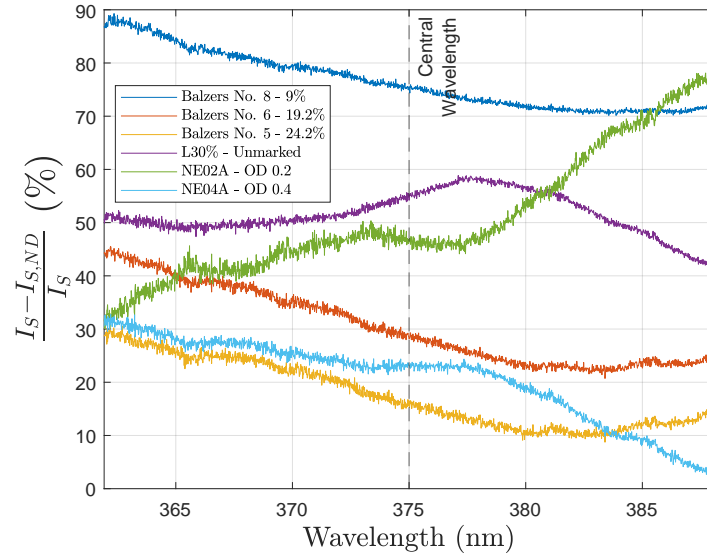


Figure 4.3: Measured ND Filter Transmission Centered at $\lambda = 375$ nm

4.1.2.2 Stokes Energy Variations

To circumvent uncertainty associated with the use of ND filters, the Stokes pulse energy was instead attenuated to account for the large change in absolute CARS signal intensity across the pressures and probe delays of interest. The Stokes beam line was equipped with a half-wave plate and a thin-film polarizer (TFP), as detailed in the experimental setup (Fig. 2.7), to allow for the continuous variation in Stokes energy. Throughout the experiment, the Stokes pulse was attenuated to avoid saturating the camera chip at early probe delays and high pressures. To ensure this method did not introduce uncertainty, the impact of various waveplate angles (66 to 300°) corresponding to various pulse energies on the CARS excitation bandwidth was explored. The results illustrate the effectiveness of this attenuation technique in modulating the excitation intensity as needed (Figure 4.4a), while

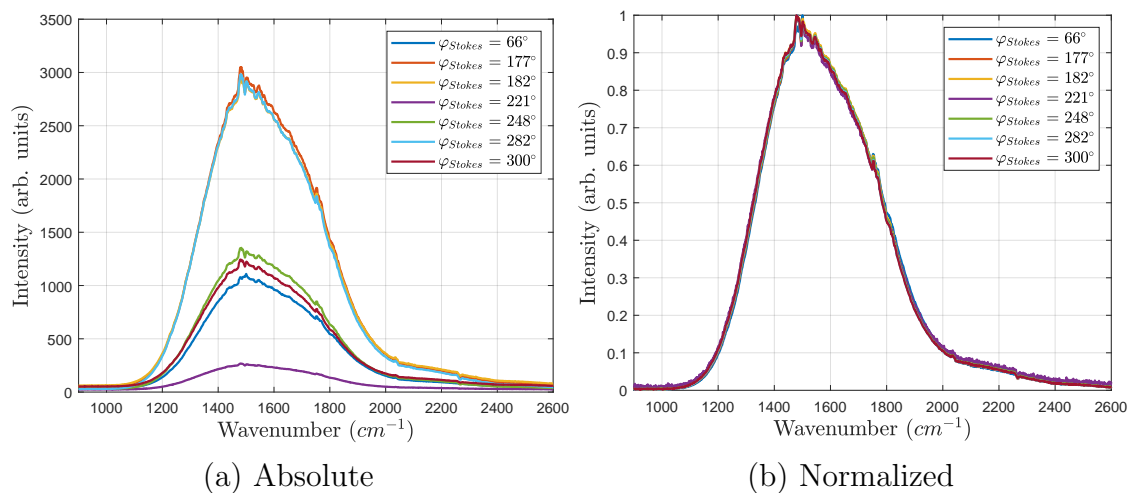


Figure 4.4: Excitation Intensity Variation at Variable ϕ TFP Adjustment

the normalized data presented in Fig. 4.4b reveals no impact on the excitation bandwidth. Therefore, this method of attenuation was selected for the CARS investigation discussed next.

4.2 Experimental Approach

The experimental approach entails selecting an optimal probe delay while maintaining a sufficient amount of signal. The analysis of the spectra requires careful background correction and consideration of excitation variations observed between laser shots and due to pressure variation.

4.2.1 Pressure Sensitivity: Probe Delay Discussion

As previously elucidated in Chapter 3, simulations of an N₂-O₂ mixture reveal a temporal range of 40 to 50 ps as an initial benchmark to attain optimal signal intensity for the specified species and achieve adequate pressure sensitivity simultaneously. Accordingly, in the upcoming experiments, a set of five probe delays are employed: one early delay at 5 ps, and four later delays (25, 35, 45, and 50 ps) strategically positioned in the proximity of the high-pressure sensitivity region. With the absence of a spectral model for CO₂ and CH₄, these probe delays are also used to infer the most sensitive ones for mixtures involving those species as an initial investigation.

4.2.2 Signal Intensity: Raman Dephasing Discussion

Variations in Q-branch CARS signal intensity among different species play a crucial role in extracting pressure from the relative CARS signal decay of different molecules. However, in general the CARS signal diminishes as the probe delay increases, presenting an experimental signal-to-noise challenge. To demonstrate this effect, preliminary experiments involving N₂-O₂, N₂-CH₄ and N₂-CO₂ static mixtures were conducted. Figures 4.5, 4.6, and 4.7 show the decay of the spectrally integrated time-domain response for various species and pressures that were measured by scanning the ps probe from -10 to 100 ps relative to the Raman excitation. Each data point represents an average from 1000 experimental spectra collected at a frequency of 1 kHz summed over the bands of the molecules of inter-

est. Further details on this time-domain molecular response function are detailed elsewhere [83]. The time-domain CARS response is shown for an air mixture ($x_{N_2} = 0.79$, $x_{O_2} = 0.21$) at pressures of 1.13, 3 and 6.99 bar, an N_2 - CH_4 mixture ($x_{CH_4} = 0.8$) at pressures of 1.07, 4.01 and 6.99 bar and N_2 - CO_2 mixture ($x_{CO_2} = 0.1$) at pressures of 1.08 and 6.03 bar.

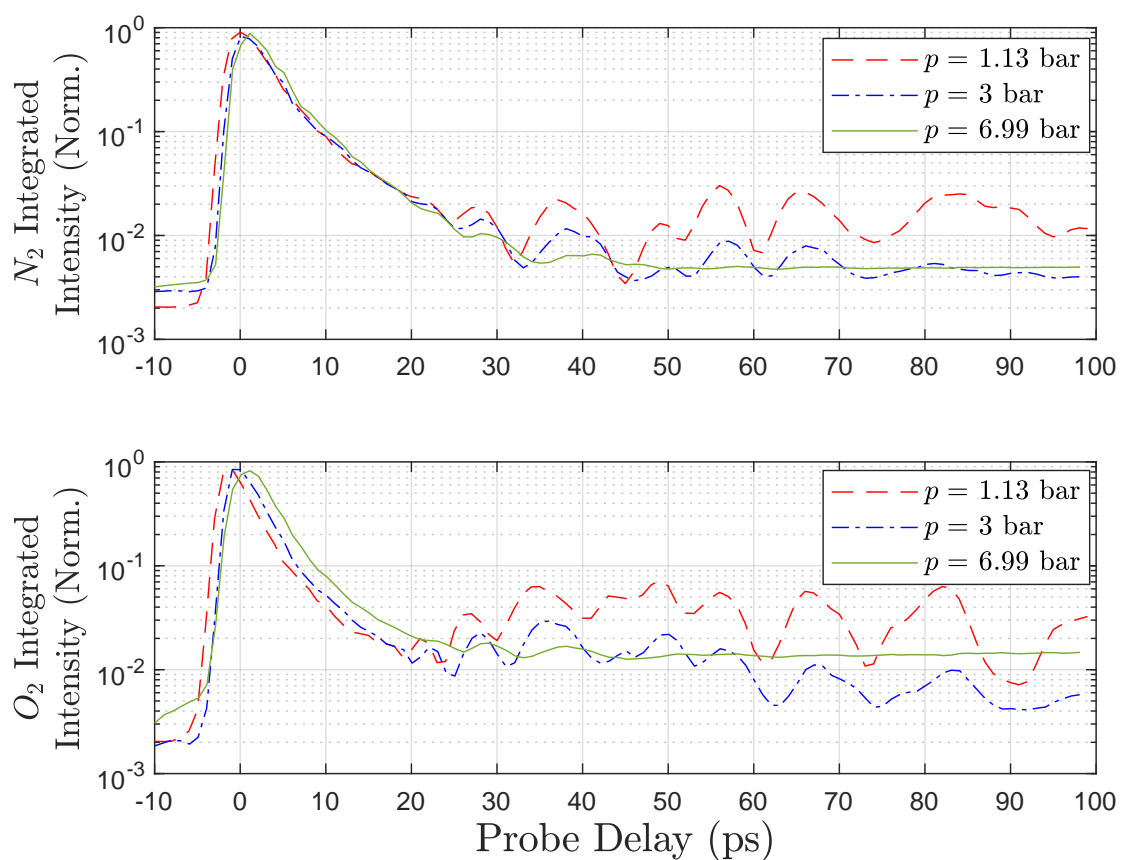


Figure 4.5: Experimentally-measured time-dependent response of fs/ps CARS for air

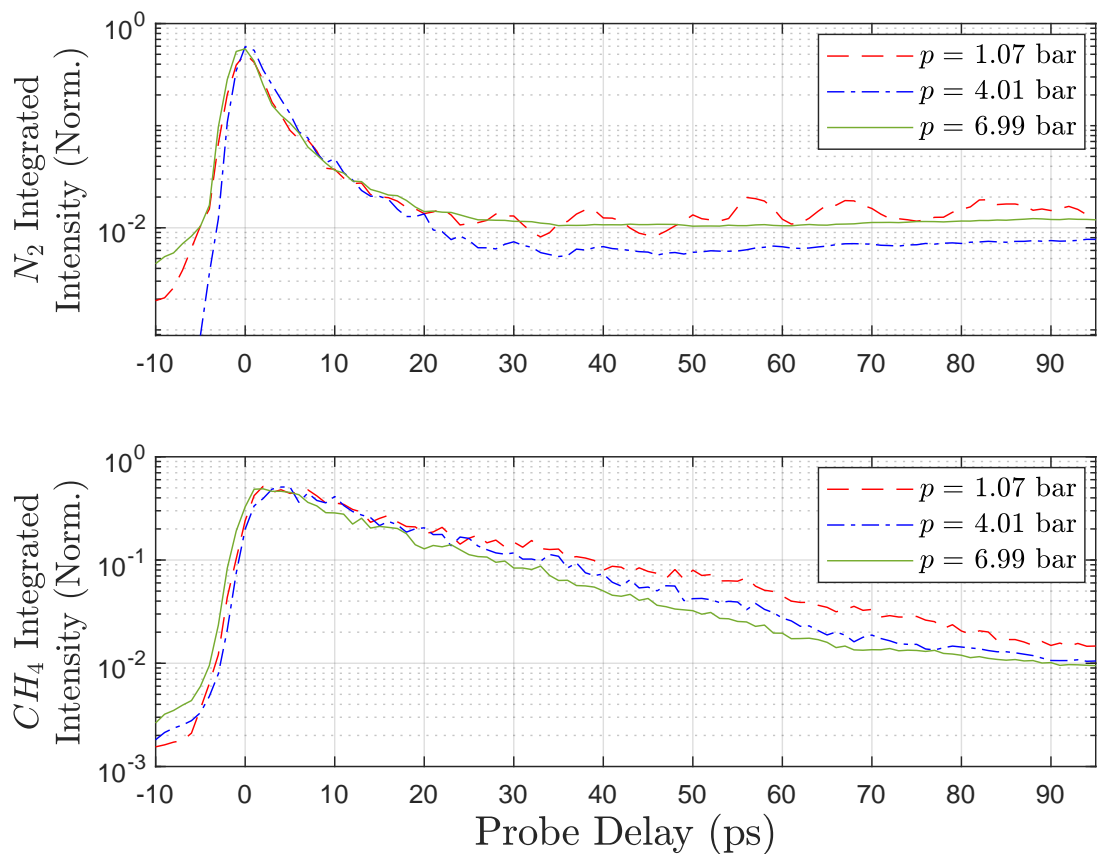


Figure 4.6: Experimentally-measured time-dependent response of fs/ps CARS for a N_2 - CH_4 mixture (80% CH_4)

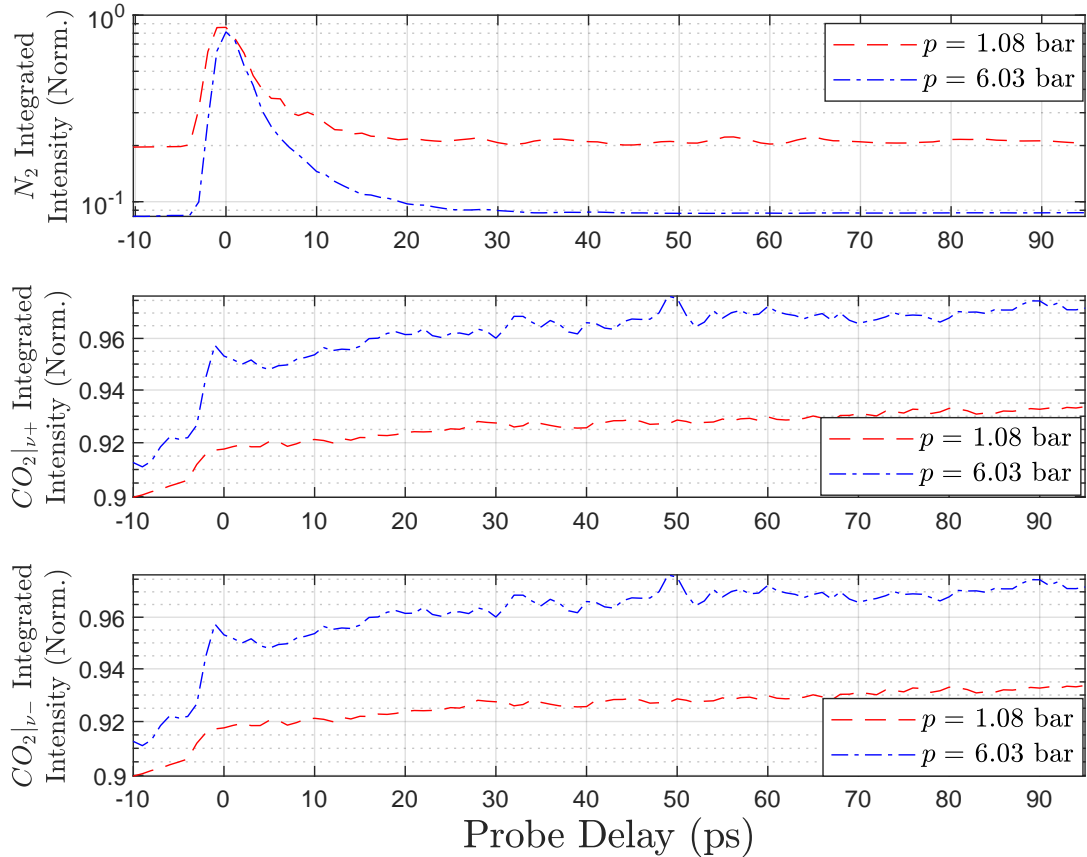


Figure 4.7: Experimentally-measured time-dependent response of fs/ps CARS for an N_2 - CO_2 mixture (10% CO_2)

A notable distinction between Fig. 4.5 and 4.6 lies in the behavior of N_2 in an O_2 environment. It demonstrates a gradual decay until approximately 25 ps, followed by periodic rephasing occurring every 6-7 ps. Conversely, in a CH_4 environment, N_2 experiences a significantly faster decay under equivalent pressures but N_2 revivals are still present, consistent with previous experimental findings by Engel *et al.* [30]. However, this rephasing is less pronounced when CH_4 is present,

likely due to the change in collisional environment. Furthermore, a consistently higher signal for CH₄ is observed throughout the entire time range (up to 100 ps). This dephasing phenomenon is influenced not only by gas composition but also by pressure. Fig. 4.5 and 4.6 show that revivals of N₂ and O₂ are significantly suppressed at high pressure ($p = 6.99$ bar) in both N₂-O₂ and N₂-CH₄ mixtures.

Differences in signal intensity can also be ascribed to differences in Raman cross-section. Specifically, for O₂, the cross-section is approximately equal to that of N₂ ($\frac{\partial\sigma}{\partial\Omega} \equiv 1.0$ [84]). In contrast, for CH₄ (2914 cm⁻¹), the cross-section is roughly 8.6 times that of N₂ [84] (multiple sources corroborate similar values, with $\frac{\partial\sigma}{\partial\Omega} \equiv 7.2$ [32], 8 [85, 86] and 8.4 [87]). In an environment where CO₂ is present, N₂ experiences virtually no revivals. However, its signal intensity remains consistently higher than when only O₂ is present. The absence of revivals is likely attributable to the collision mechanism with CO₂, rather than disparities in Raman cross-section, as the latter are comparable. The Raman cross-section for CO₂'s $\nu+$ is only 1.3 times that of N₂ [32] ($\frac{\partial\sigma}{\partial\Omega} \equiv 0.8$ [88]). Similarly, the Raman cross-section for CO₂ $\nu-$ is roughly 0.9 times that of N₂ [32].

CARS intensity exhibits a quadratic dependence on the Raman cross section: $I_{CARS} \propto \left(\frac{\partial\sigma}{\partial\Omega}\right)^2$. Consequently, the anticipated strength of the CH₄ signal is approximately 74 times greater than that of N₂, while the signals from CO₂ are expected to be comparable to that of N₂. To ensure optimal signal strength for the involved molecules, the excitation is strategically centered between the N₂ and CO₂ bands in a N₂-CO₂ mixture, and is biased towards N₂ in an N₂-CH₄ mixture. In scenarios where the concentration of N₂ significantly exceeds that of CO₂, the

excitation is adjusted closer to the CO₂ bands. In contrast, even if the N₂ concentration is much greater than that of CH₄, the excitation should still be biased towards N₂ due to the stark differences in Raman cross section.

In this context, the selection of 35, 45 and 50 ps as the experimental late probe delays appear initially to be optimal candidates for both good pressure sensitivity and signal strength. At least one of these particular probe delays should correspond to an intensity peak in the N₂-O₂ mixture time scan, and around 10% of the initial signal for the N₂-CH₄ mixture, providing sufficient signal for a meaningful comparison of the distinct spectral features of N₂ and CH₄.

4.3 Results: Spectral Analysis Considerations

In order to improve the accuracy of spectral analysis, care must be taken with regard to background correction to measure relative intensities and infer gas pressure accurately. Additionally, fluctuations in the excitation profile were examined to determine the possibility of using single-shot experimental data to measure pressure.

4.3.1 Background Correction

A set of averaged N₂ and O₂ spectra at various pressures without background subtraction are shown in Fig. 4.8a. A noticeable difference in the baseline becomes evident among spectra recorded at various pressures. Additionally, the baselines in the raw spectra do not align with the background spectra recorded at each re-

spective pressure obtained after blocking the Stokes beam, as shown in Fig. 4.8b. This discrepancy poses a challenge when comparing relative species signal intensities, as it results in an offset in the summed spectral intensity after background subtraction. While this may not be a significant concern when the primary spectral features of interest are significantly larger than the baseline, it introduces significant error when the signal of one or both of the studied spectral features is low.

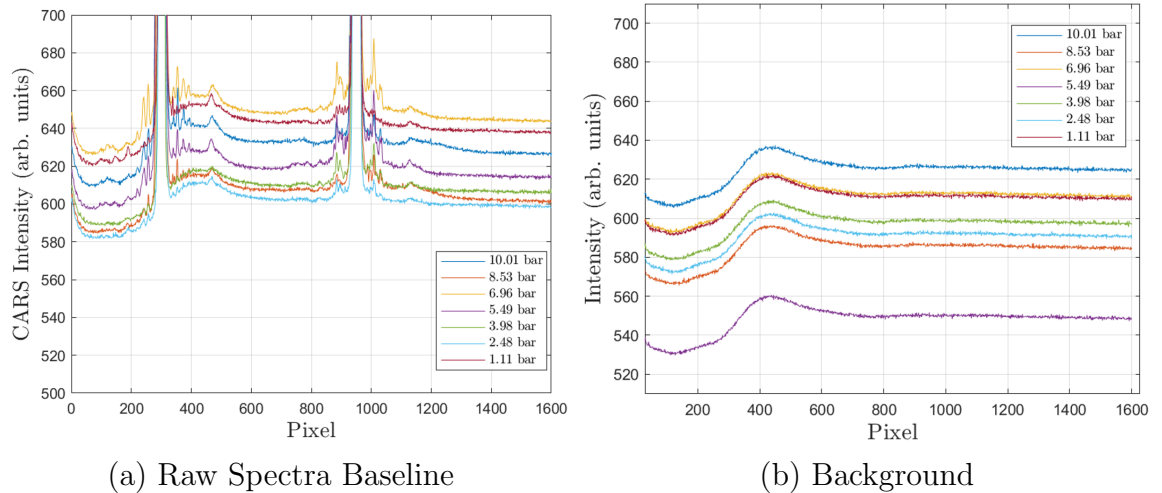


Figure 4.8: Experimental $\text{N}_2\text{-O}_2$ CARS Spectra Baseline at a Selection of Pressures (1.11-10.01 bar)

Consider, for instance, the case of N_2 and CO_2 , where the limited laser bandwidth inherently leads to certain spectral features of CO_2 having relatively low intensity—especially for low pressures at late probe delay. Additionally, a large difference in signal intensity is expected for mixtures where one species exists in a much higher concentration. In such instances, ensuring an accurate baseline becomes crucial for a meaningful and precise measurement of pressure.

This challenge was addressed by using an inferred background instead of the recorded backgrounds. This background is determined based on the minimum signal near the vicinity of the transitions of interest. Now after subtracting the inferred background and normalizing, the plots show a clean constant baseline as Fig. 4.9 illustrates with the spectra normalized with respect to the O₂ peak at each pressure. This improves accuracy when comparing spectral features in the upcoming analysis.

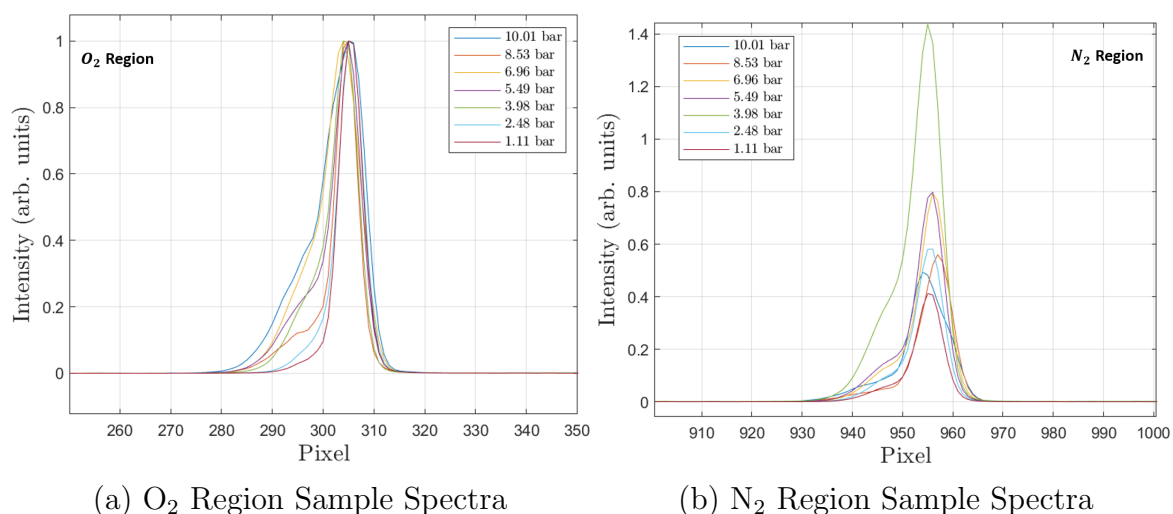


Figure 4.9: Post-Processing Background Correction For an N₂-O₂ Mixture at a Selection of Pressures (1.11-10.01 bar)

4.3.2 Shot-to-Shot Fluctuations in Raman Excitation

A typical broadband excitation spectrum is shown in Fig. 4.10. The spectral ranges corresponding to N₂ (blue region) and O₂ (red region) Q-branch peaks are also shown. This excitation spectrum corresponds to the nonresonant CARS sig-

nal recorded in pure Argon at near-atmospheric pressure. For this experiment, the excitation bandwidth was intentionally biased towards O_2 as clearly shown in the averaged profile in Fig. 4.10a. This is because O_2 has slightly faster molecular coherence dephasing compared to N_2 . More crucially, given that O_2 constitutes a maximum of 21% in an air-fed combustion scenario, enhancing the excitation of O_2 ensures sufficient signal as x_{O_2} decreases with oxygen consumption. Fig. 4.10b shows normalized Argon spectra on a shot-to-shot basis, revealing variability in excitation between laser shots. This variability poses a significant challenge, particularly when examining single-shot measurements in dynamic combustion environments.

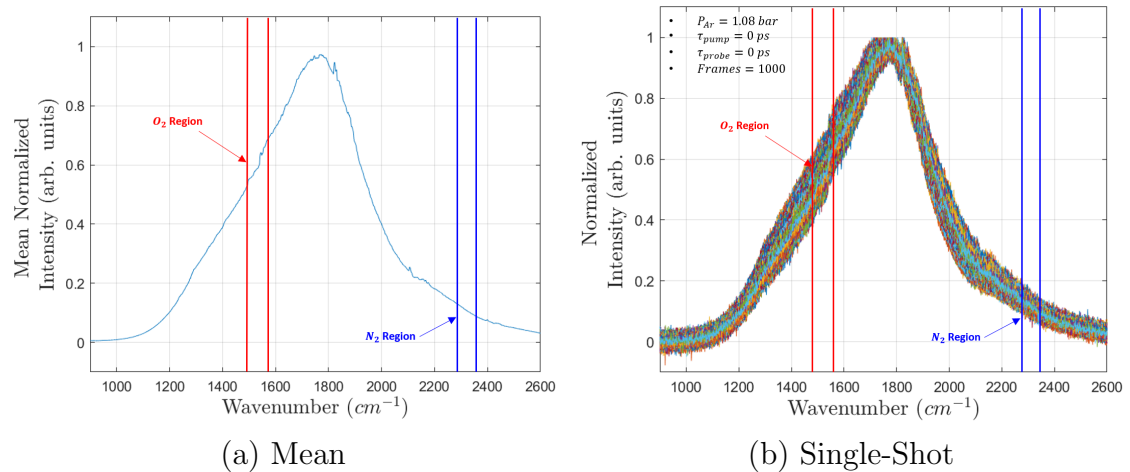


Figure 4.10: Experimental Excitation Profile: Pump-Stokes Convolution

To investigate the observed shot-to-shot excitation bandwidth shift, the correlation between excitation across the N_2 region and that across the O_2 region is analyzed. As illustrated in Fig. 4.11, a negative correlation is observed. This trend suggests that as N_2 experiences higher Raman excitation, the excitation of

the O₂ CARS Q-branch signal decreases, introducing significant uncertainty in “single-shot” measurements. This effect is not expected to significantly impact shot-averaged results. Despite the challenges posed by these variations, the Optical Parametric Amplifier (OPA) provides a sufficiently broad spectral bandwidth to impulsively excite the vibrational transitions in N₂-CO₂, N₂-CH₄, N₂-O₂ and N₂-O₂-CO₂ mixtures simultaneously. Therefore, the trends and conclusions drawn in the upcoming sections will primarily rely on spectra averaged over 1000 laser shots for all the mixtures to ensure the reliability of the results.

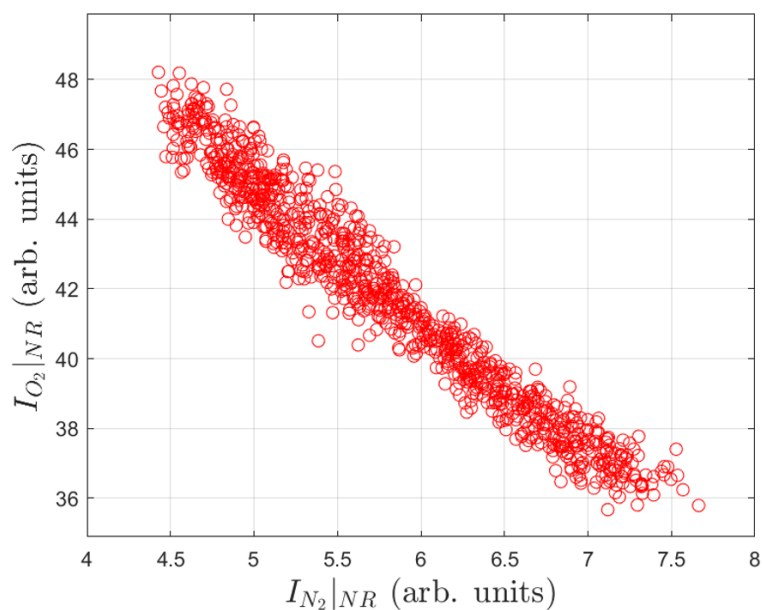


Figure 4.11: N₂ vs. O₂ Excitation

4.3.3 Excitation Variation at Elevated Pressures

The central wavelength of the excitation bandwidth was observed to change significantly at various static pressure cell pressures, an unexpected effect. This phenomenon became apparent when considering the nonresonant background observed when the probe and pump/Stokes pulses were overlapped in time during probe delay scans at three different pressures, shown in Fig. 4.12 and Fig. 4.13. The contour plots at various pressures show the time-and-frequency CARS response, where the resonant CARS features are narrow in frequency and persist at late probe delays. In contrast, the nonresonant signal is broad and frequency and is observed over ≈ 4 ps range. The spectrum at probe delays corresponding to the red line in each contour plot are overlaid to show how the nonresonant signal (indicating the Raman excitation) shifts in frequency as pressure is varied. The results shown in Fig. 4.12 and Fig. 4.13 were obtained on different days and show slightly different behavior.

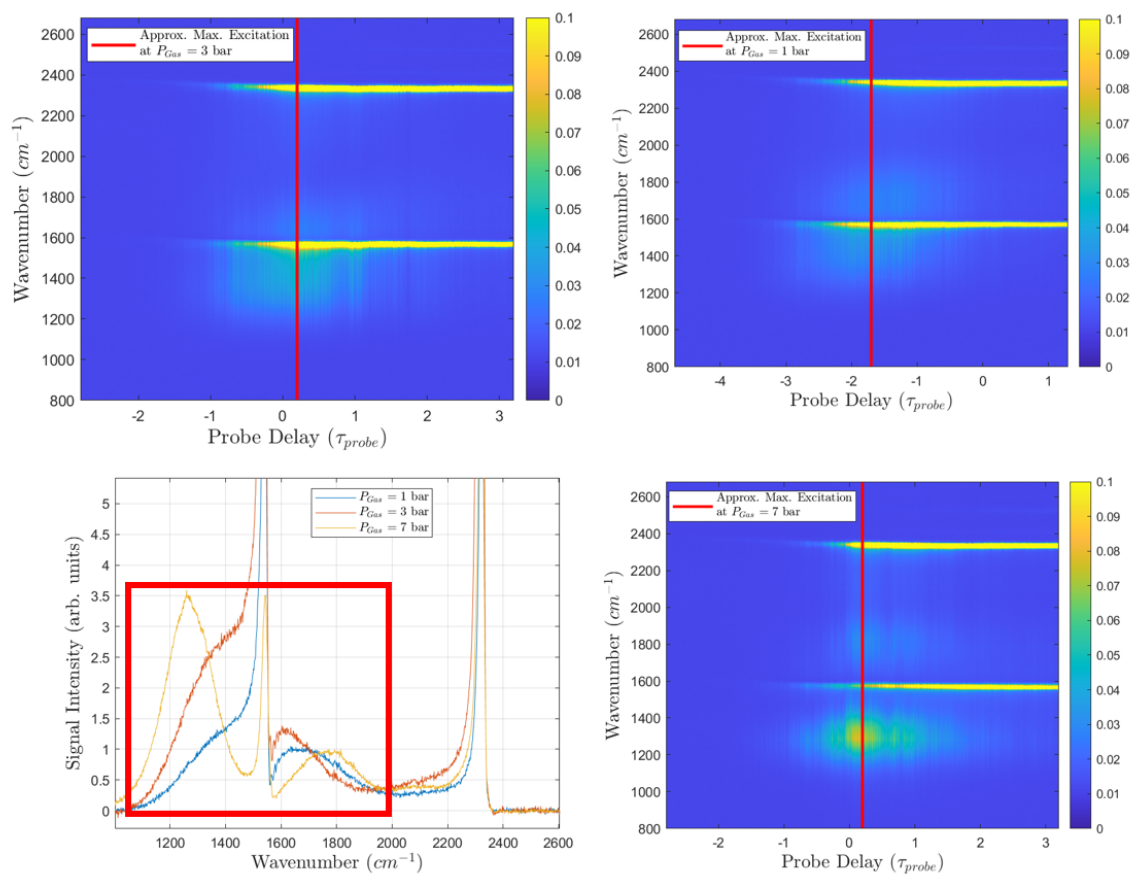


Figure 4.12: Air Mixture Time Scans and Averaged Spectra Near $\tau_{probe} = 0$ ps, Recorded at Pressures: 1, 3 and 7 bar (Early November 2023)

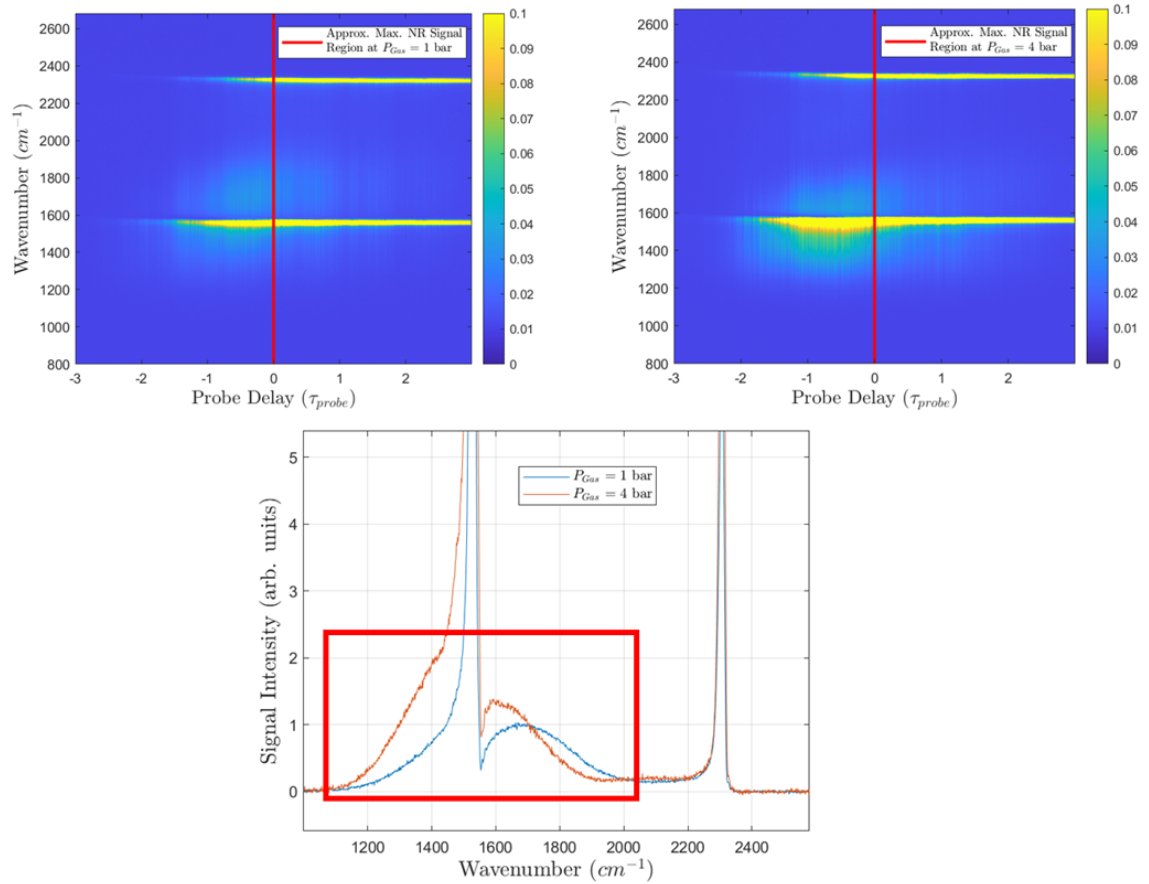


Figure 4.13: Air Mixture Time Scans and Averaged Spectra Near $\tau_{probe} = 0$ ps, Recorded at Pressures: 1 and 4 bar (Mid November 2023)

The data shown in Fig. 4.14 were obtained on an earlier data collection run and shows significantly less variation in excitation at different pressures, demonstrating how the spectral shift in excitation with increasing pressure is not consistent. Unfortunately, this implies that the variability cannot be mitigated through the use of averaged spectral data or by modeling the excitation at various pressures. Therefore, an alternative strategy was devised to address this significant exper-

imental challenge in order to achieve an accurate measurement of pressure in a dynamic combustion environment. The details of this approach are included in the forthcoming sections.

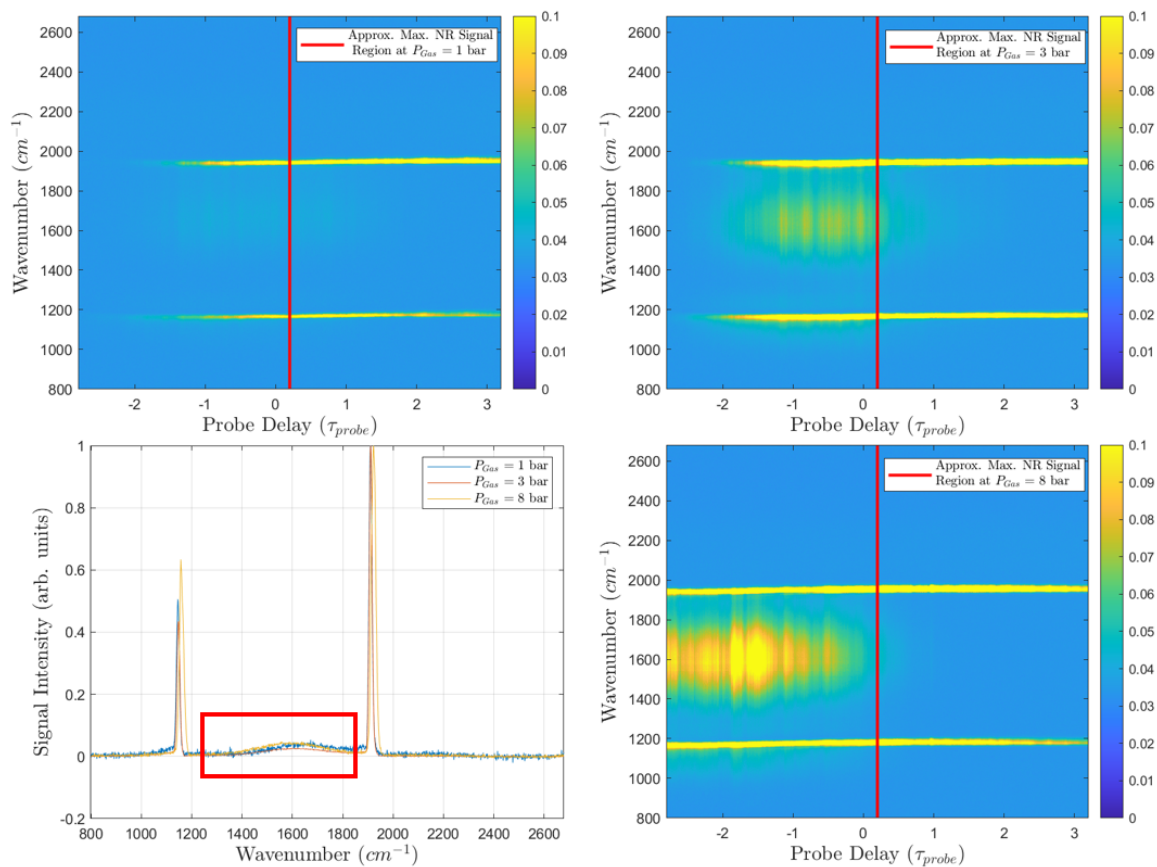


Figure 4.14: Air Mixture Time Scans and Averaged Spectra Near $\tau_{probe} = 0$ ps, Recorded at Pressures: 1 and 4 bar (July 2023)

4.4 Results: N₂-O₂ Gas Mixtures

A static gas mixture of N₂ and O₂ was examined under absolute pressures spanning a range of 1 to 10.5 bar in order to quantify the spectral response to changes in pressure. Four probe delays were chosen: one early at $\tau = 5$ ps (illustrated in Fig. 4.15a) and three late at $\tau = 25, 35$ and 45 ps (illustrated in Fig. 4.15b). Due to the shot-to-shot fluctuations in the Raman excitation described earlier, the single-shot data exhibited large error. Examining the averaged results shows a consistent, non-physical increase in spectral ratio until 4 bar and subsequent decrease superimposed over the data at every probe delay as shown in Fig. 4.16. This is due to the previously discussed variation in Raman excitation at different pressures. This issue is corrected by scaling the pressure-sensitive late probe delay spectra by the early probe pressure-insensitive spectra.

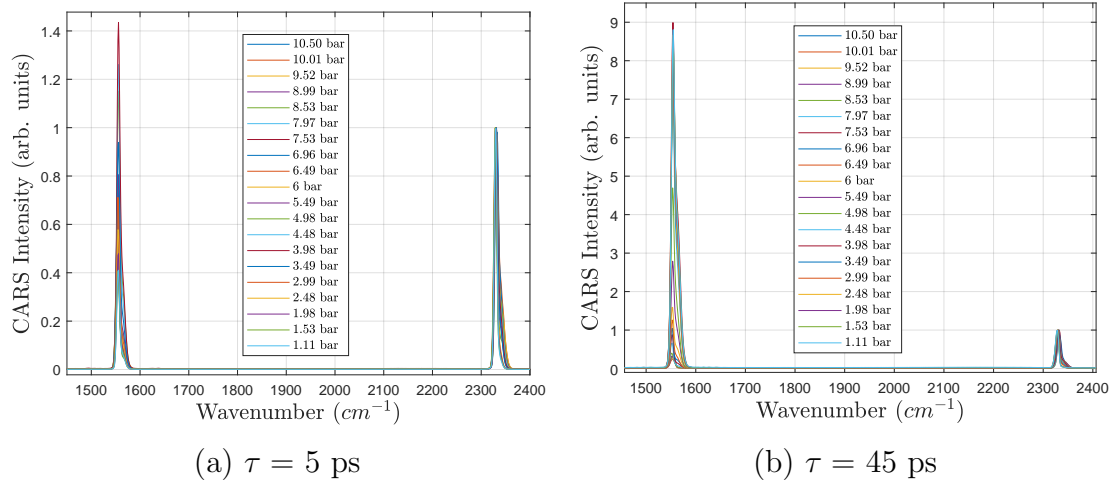


Figure 4.15: Q-branch Raman spectra of a N₂-O₂ gas mixture ($x_{O_2} = 0.21, x_{N_2} = 0.79$)

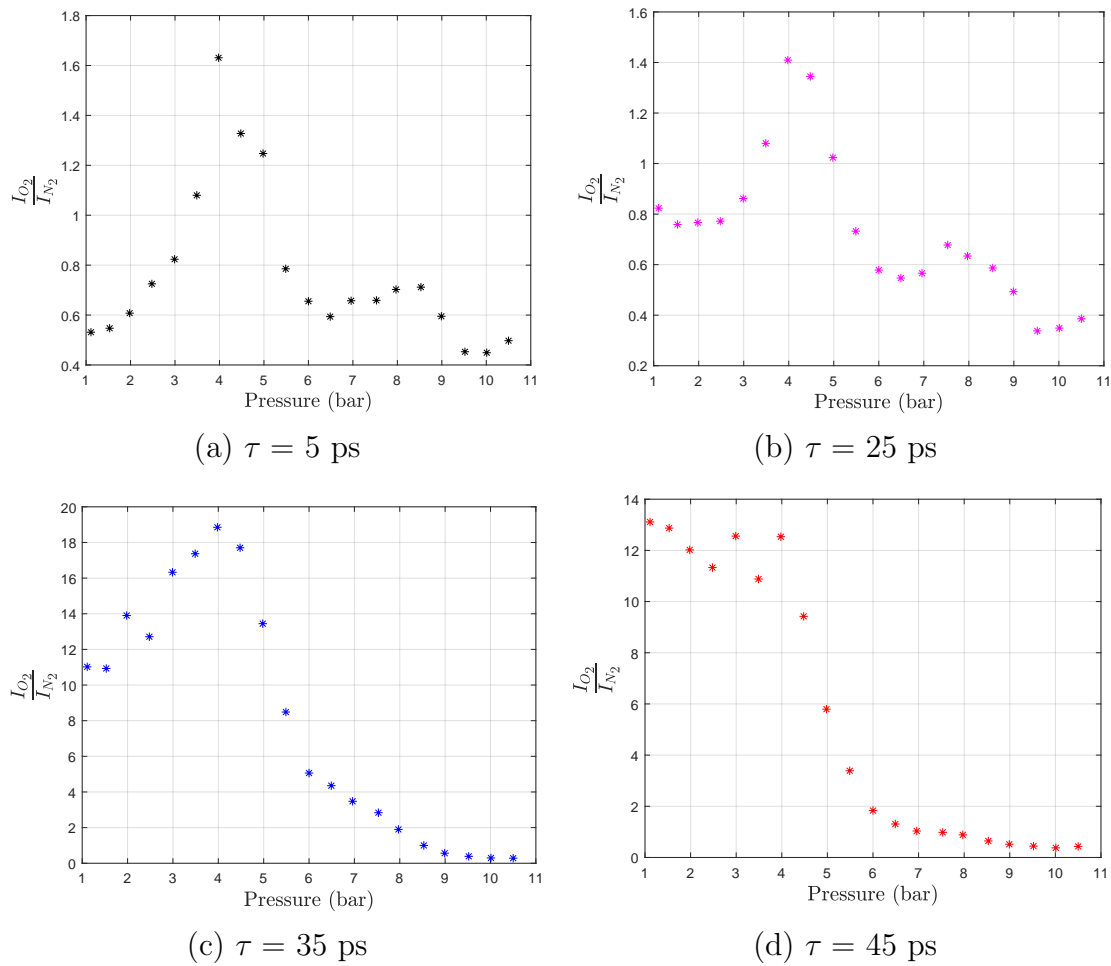


Figure 4.16: Experimental intensity ratio $\frac{I_{O_2}}{I_{N_2}}$ measured at absolute pressures from 1–11 bar and four ps probe delays.

Eliminating error due to the shifting Raman excitation at various pressures leads to a close match to simulation, as depicted in Fig. 4.17. This figure shows the spectral ratio at 45 ps scaled by the spectral ratio at the early delay (5 ps). Both simulation and experimental results have been normalized to values at a pressure p of 1 bar, and they show good agreement. By scaling CARS spectra acquired at late probe delay (45 ps) with those of early probe delay (5 ps), the change in experimental $\frac{I_{O_2}}{I_{N_2}}$ with respect to pressure follows the trend predicted by the fs/ps CARS model. This is in contrast with the non-scaled results shown in Fig. 4.16 that include non-physical changes with pressure due to uncertainty in the Raman excitation bandwidth. Therefore, the results shown in Fig. 4.17 demonstrate the powerful utility of this spectral analysis technique, enabling the determination of pressure using resonant CARS spectra acquired at two ps probe delays without correcting for changes in Raman excitation. This is explored further in Fig. 4.18, where the $\frac{I_{O_2}}{I_{N_2}}$ ratios are calculated using a range of variable pump and Stokes parameters while keeping probe parameters constant. Both simulation and experimental results are normalized to values at a reference pressure p of 1 bar. Notably, the simulated curves from five distinct sets of excitation parameters, as outlined in Tab. 4.1, show no difference. The experimental data align closely with this function.

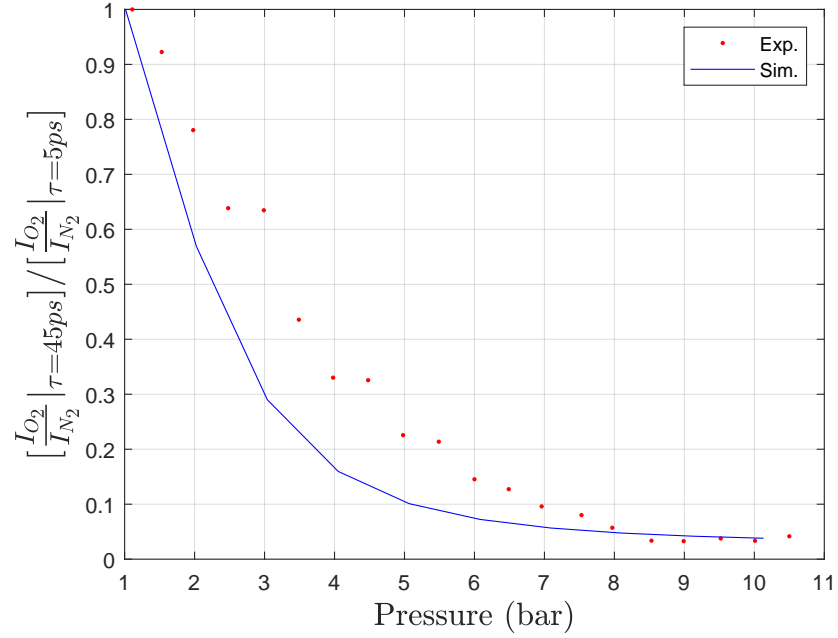


Figure 4.17: Pressure dependence using $\frac{I_{O_2}}{I_{N_2}}$ for an air mixture

Table 4.1: List of excitation parameters tested for a given set of probe parameters

Parameters	Probe	Pump	Stokes
1	$\lambda = 400 \text{ nm}$, $\Delta\nu = 1.1 \text{ cm}^{-1}$	$\lambda = 703.25 \text{ nm}$, $\Delta\nu = 400 \text{ cm}^{-1}$	$\lambda = 800 \text{ nm}$, $\Delta\nu = 400 \text{ cm}^{-1}$
2	$\lambda = 400 \text{ nm}$, $\Delta\nu = 1.1 \text{ cm}^{-1}$	$\lambda = 700 \text{ nm}$, $\Delta\nu = 400 \text{ cm}^{-1}$	$\lambda = 800 \text{ nm}$, $\Delta\nu = 400 \text{ cm}^{-1}$
3	$\lambda = 400 \text{ nm}$, $\Delta\nu = 1.1 \text{ cm}^{-1}$	$\lambda = 690 \text{ nm}$, $\Delta\nu = 470 \text{ cm}^{-1}$	$\lambda = 800 \text{ nm}$, $\Delta\nu = 470 \text{ cm}^{-1}$
4	$\lambda = 400 \text{ nm}$, $\Delta\nu = 1.1 \text{ cm}^{-1}$	$\lambda = 695 \text{ nm}$, $\Delta\nu = 500 \text{ cm}^{-1}$	$\lambda = 800 \text{ nm}$, $\Delta\nu = 480 \text{ cm}^{-1}$
5	$\lambda = 400 \text{ nm}$, $\Delta\nu = 1.1 \text{ cm}^{-1}$	$\lambda = 705 \text{ nm}$, $\Delta\nu = 400 \text{ cm}^{-1}$	$\lambda = 800 \text{ nm}$, $\Delta\nu = 430 \text{ cm}^{-1}$

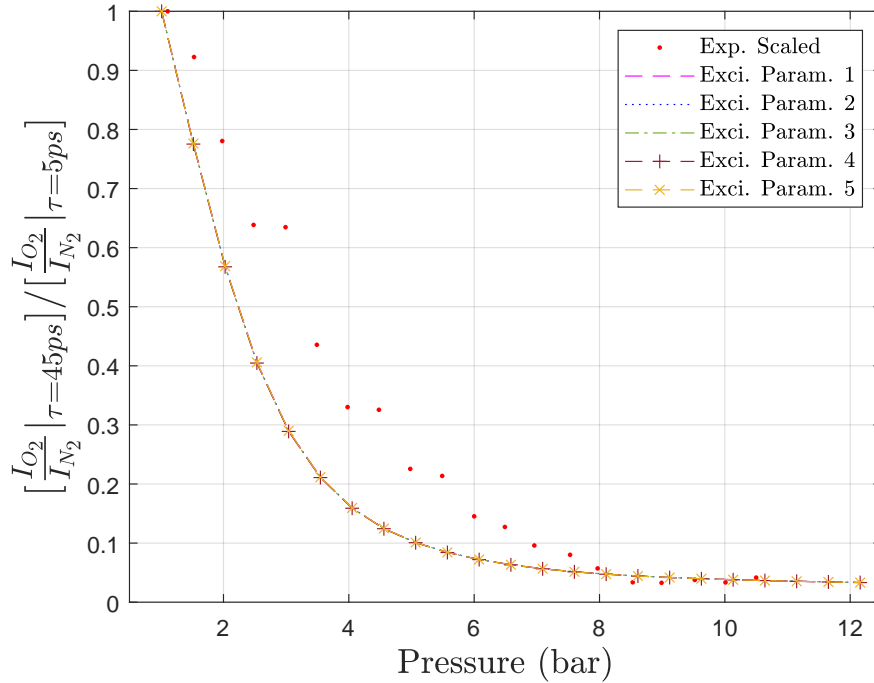


Figure 4.18: Experimental $\frac{I_{O_2}}{I_{N_2}}$ Pressure Dependence vs. Simulation Using Excitation Parameters from Table 4.1 for Air

The study also took into account the impact of uncertainty in modeling the ps probe pulse on the pressure-dependent $\frac{I_{O_2}}{I_{N_2}}$ ratio. To explore this influence, seven N₂-O₂ spectra were simulated across various probe bandwidths, employing the same set of excitation parameters (pump: $\lambda = 703.25$ nm, $\Delta\nu = 400$ cm⁻¹, Stokes: $\lambda = 800$ nm, $\Delta\nu = 400$ cm⁻¹). The simulated results, presented in Fig. 4.19, highlight the significant role that probe bandwidth plays in the rate at which the $\frac{I_{O_2}}{I_{N_2}}$ ratio decays. The technique exhibits heightened pressure sensitivity with a narrower bandwidth, a characteristic clearly illustrated by comparing the ratio decay with probe bandwidths of 10 cm⁻¹ and 0.8 cm⁻¹. This observation suggests

a potential means of tailoring sensitivity to pressure variations by adjusting probe bandwidth based on experimental objectives.

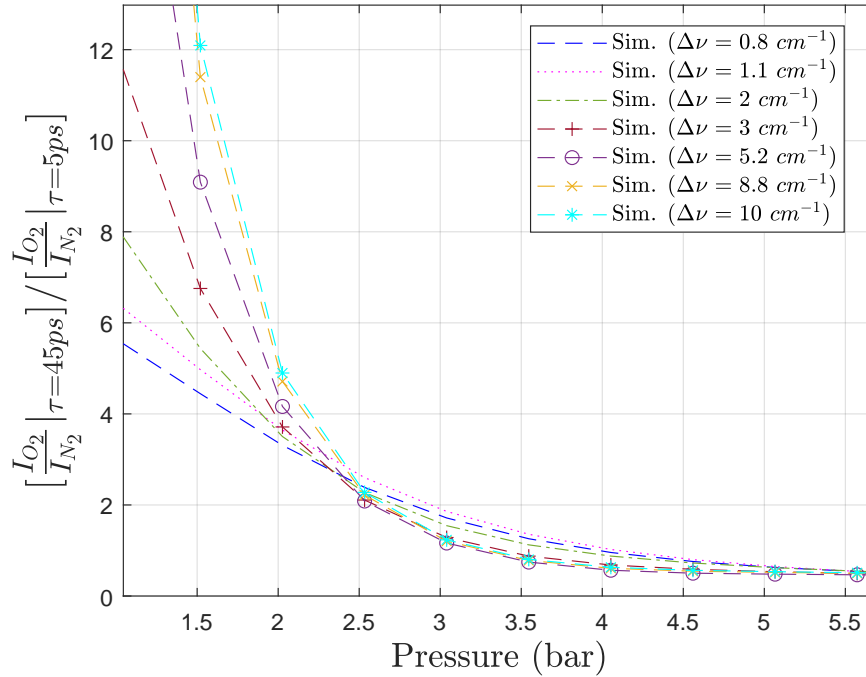


Figure 4.19: Simulated pressure dependence for variable N₂-O₂ Gas mixture using the scaled $\frac{I_{O_2}}{I_{N_2}}$ ratio and variable probe parameters ($\lambda = 400$ nm)

As previously discussed, the $\frac{I_{O_2}}{I_{N_2}}$ ratio depends on both species and pressure as illustrated in Fig. 4.20 for a ps probe delay of 45 ps. However, using the new spectral analysis method significantly reduces uncertainty due to variation in composition as demonstrated by the simulations at six different concentrations varying from 50% O₂ to 5% O₂ as shown in Fig. 4.21a. This behavior is confirmed by experimental spectra acquired at four different gas compositions as shown in Fig. 4.21b. Within the context of a dynamic combustion environment, characterized

by fluctuating concentrations of N_2 and O_2 —where N_2 is frequently introduced to either dilute the flow or stabilize the flame, while O_2 is actively consumed—the value of this method becomes evident. Its capacity shown to be largely unaffected by such variations provides a significant advantage. This implies its potential usefulness in tracking and measuring local pressure without the need for meticulous quantification of gas composition. While the demonstrated success has only been shown in binary controlled N_2 - O_2 mixtures, further exploration of this spectral analysis method is necessary to substantiate and validate these promising results.

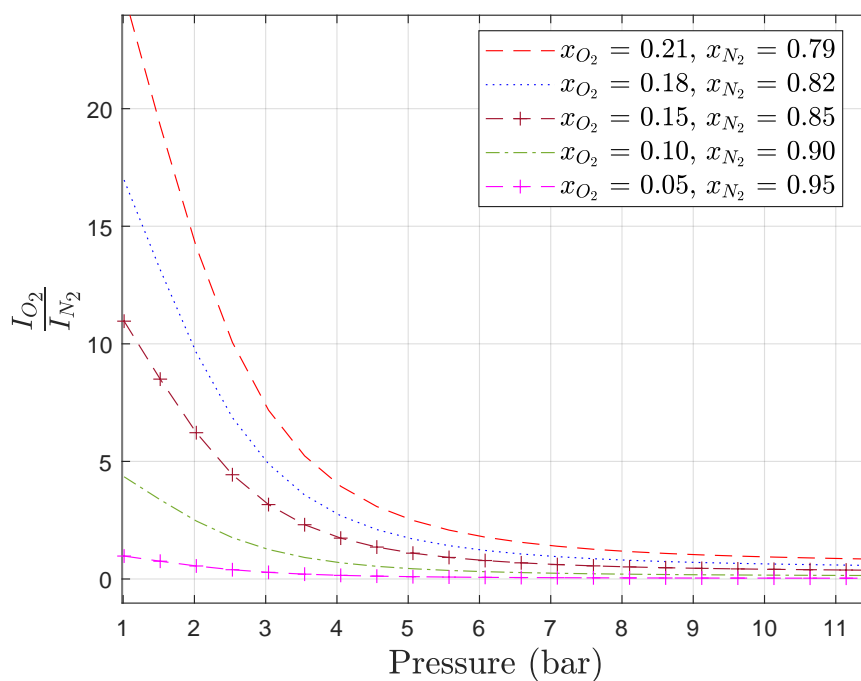


Figure 4.20: Simulated pressure dependence for variable N_2 - O_2 Gas mixture using the non-scaled $\frac{I_{O_2}}{I_{N_2}}$ ratio

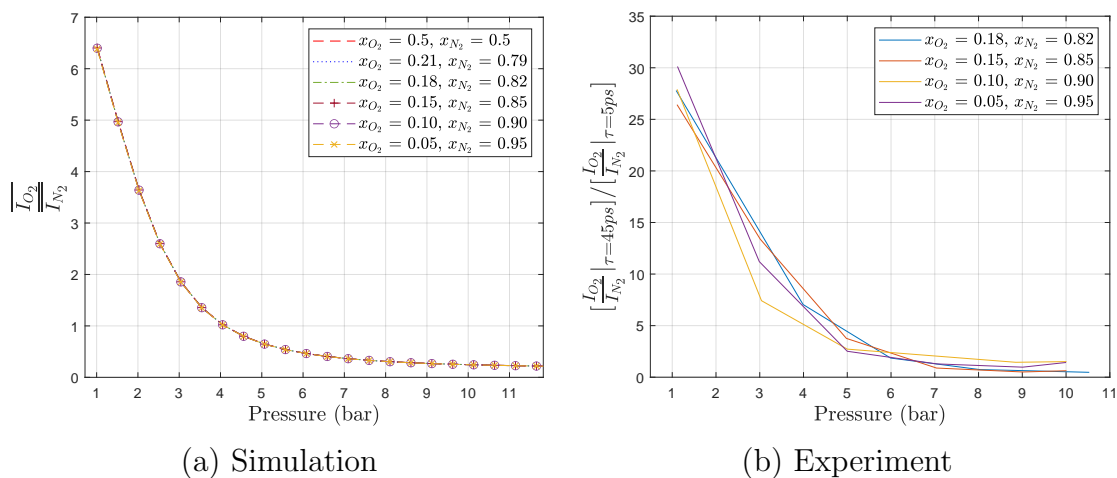


Figure 4.21: Pressure dependence in variable concentration N_2 - O_2 gas mixtures using the scaled $\frac{I_{O_2}}{I_{N_2}}$ Ratio

4.5 Results: N_2 - CH_4 Gas Mixtures

This methodology is applicable to various combustion-relevant expanded gas mixtures, as demonstrated by examining the pressure dependency of an 80% CH_4 -20% N_2 mixture representing a fuel-rich region in a combustor. In Fig. 4.22, the scaled experimental $\frac{I_{N_2}}{I_{CH_4}}$ ratio closely fits a power-law function in the form $a \cdot P^n$. This reinforces the versatility of the technique and its ability to capture the pressure-related effects using species other than N_2 and O_2 where O_2 may not be present in significant concentrations.

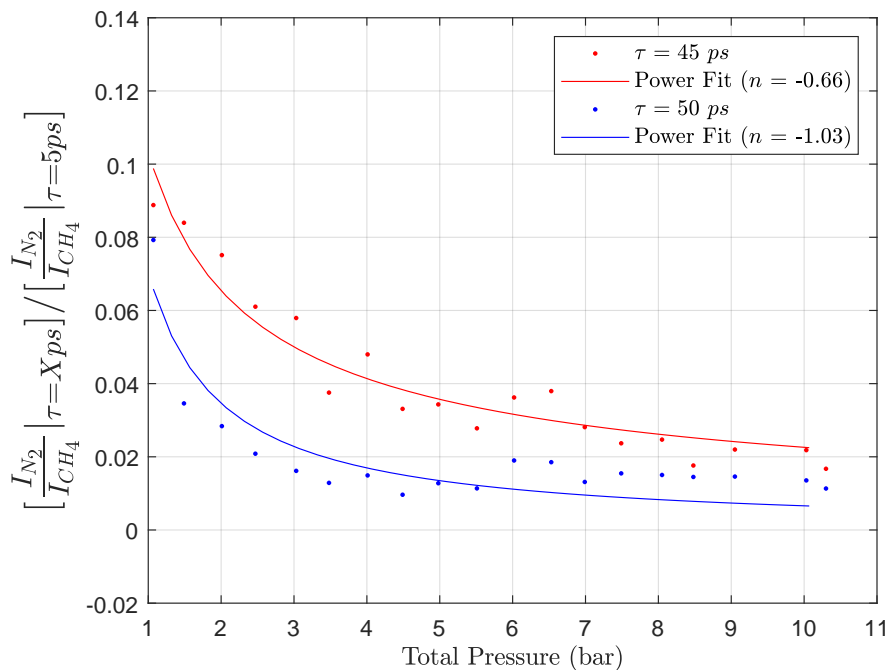


Figure 4.22: Experimental pressure dependence for one $\text{N}_2\text{-CH}_4$ gas mixture using the scaled $\frac{I_{\text{N}_2}}{I_{\text{CH}_4}}$ ratio at two late probe delays

4.6 Results: $\text{N}_2\text{-CO}_2$ Gas Mixtures

Only the ν_1 mode (1333 cm^{-1}) out of the four CO_2 vibrational modes is Raman-active. The experimental $\text{N}_2\text{-CO}_2$ Q-branch Raman spectra presents three strong vibrational bands as illustrated in Fig. 4.23. One is attributed to the vibrational mode of diatomic N_2 and the other two are the product of Fermi resonance [89] between the excited vibrational states of ν_1 and the first overtone of ν_2 ($2\nu_2 = 2 \times 667 = 1334\text{ cm}^{-1}$). ν_1 and ν_2 have nearly the same frequency and they perturb each other to produce a division that results in two peaks located at two opposite

sides of the ν_1 and ν_2 Raman shifts. This phenomena known as Fermi diad splitting creates the two higher and lower energy bands at 1388 cm^{-1} and 1283 cm^{-1} , labeled as ν_+ and ν_- respectively [89] observed at room temperature.

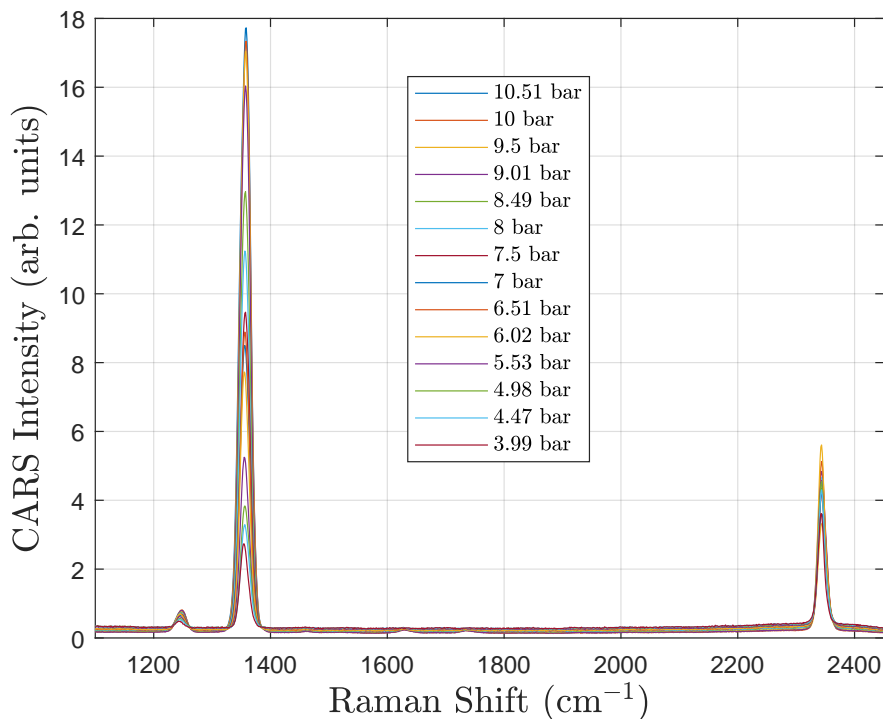


Figure 4.23: Q-branch Raman spectra of a $\text{N}_2\text{-CO}_2$ gas mixture ($x_{\text{CO}_2} = 0.1$, $x_{\text{N}_2} = 0.9$) at $\tau = 35$ ps spectra

After proper baseline subtraction, the ν_+ and ν_- transitions of CO_2 may be used for monitoring pressure. The linear correlation between their ratio and pressure, depicted in Fig. 4.24 at a late probe delay of 35 ps, underscores the potential of utilizing this dependence as an effective method for tracking the pressure field over a very large range of pressures. The use of the new method is not shown here due to the lack of available experimental data at early probe delay.

One surprising result is that the ratio of the ν_+ and ν_- transitions of CO_2 is sensitive to the CO_2/N_2 concentration, as shown by the two curves of different concentrations in Fig. 4.24. A possible explanation for why the Fermi dyads are sensitive to N_2 concentration is indirect as they depend on CO_2 density. As CO_2 density increases, the vibrational relaxation varies affecting the spectral profile of CO_2 [90]. Therefore, the amount of CO_2 present can influence line-coupling effects involved in the shaping of the ν_+ and ν_- bands due to rotational energy transfer, and this effect explains why the spectral ratio is impacted by the relative N_2 concentration.

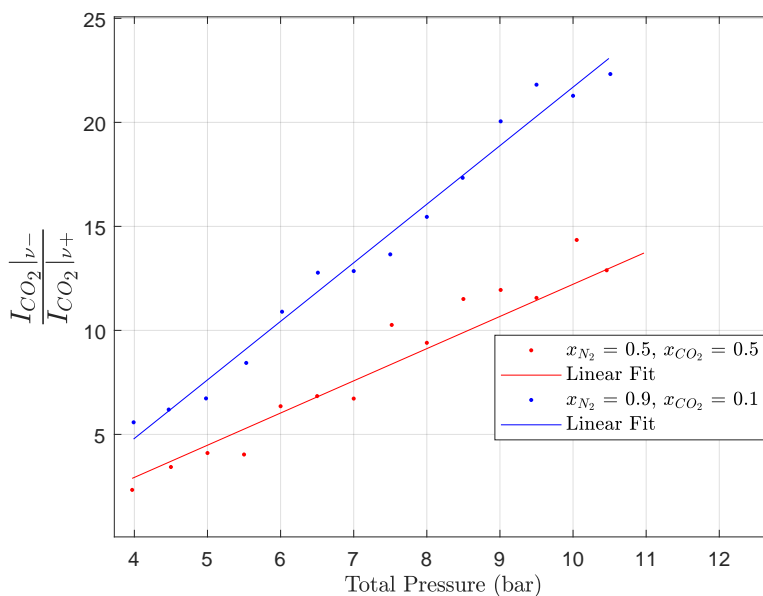


Figure 4.24: Experimental pressure dependence for one N_2 - CO_2 gas mixture using the non-scaled $\frac{I_{\text{CO}_2|\nu_-}}{I_{\text{CO}_2|\nu_+}}$ Fermi dyads ratio at $\tau = 35$ ps

Examining the ratio of CO_2 's ν_+ and N_2 bands (Fig. 4.25) at a late probe delay of 35 ps reveals an increasing trend with rising pressure. This ratio exhibits

a near-quadratic dependence when N_2 is the predominant gas ($x_{CO_2} = 0.1$, $x_{N_2} = 0.9$), while it demonstrates a nearly linear relationship when the two gases have an equal mole fraction ($x_{CO_2} = 0.5$, $x_{N_2} = 0.5$). Although, it is crucial to consider mole concentration, this dependency underscores the potential utility of the ratio in monitoring local pressure during combustion, given the consistent abundance of these gases in reaction and post-reaction zones. The application of the new method is not shown here due to the lack of available experimental data at early probe delay.

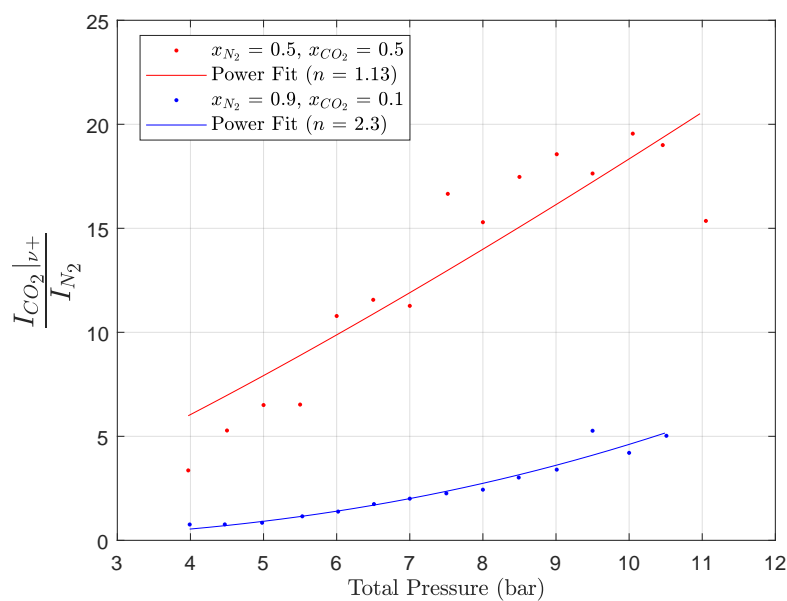


Figure 4.25: Experimental pressure dependence for two N_2 - CO_2 gas mixture using the non-scaled $\frac{I_{CO_2|\nu+}}{I_{N_2}}$ ratio at $\tau = 35$ ps

4.7 Chapter Summary

In summary, this chapter included an experimental investigation of Q-branch CARS response at elevated pressures in gas mixtures involving N_2 , O_2 , CO_2 , and CH_4 in a static pressure cell. It also presents a novel method for reducing uncertainty due to changes in Raman excitation by scaling the experimental spectra at late probe delay (pressure-sensitive) by those recorded at early probe delay (pressure-insensitive). This novel method also enables a measurement of pressure within a gas of unknown composition with significantly reduced uncertainty. N_2 - O_2 experimental results were compared to spectral simulations showing good agreement. Experimental results demonstrating strong pressure sensitivity within N_2 - CH_4 and N_2 - CO_2 mixtures were also presented.

5 Conclusions

5.1 Summary

Q-branch ro-vibrational hybrid femtosecond/picosecond coherent anti-Stokes Raman scattering (CARS) was explored for quantifying in-flow gas pressures. Initially, the investigation focused on analyzing the relative intensities of I_{O_2} and I_{N_2} across a pressure range spanning from 1 to 10 bar and a probe delay up to 100 ps. The primary objective was to identify probe delays exhibiting high pressure sensitivity, thereby determining the optimal probe delay for precise pressure quantification. Multiple probe delays and thermodynamic conditions were investigated efficiently by adapting the existing fs/ps CARS modeling code. Furthermore, this code was integrated with a Cantera solution to explore the CARS spectral response throughout a 1-D diffusion flame at various pressures. This allowed for the incorporation of temperature, pressure, and mole fraction information to predict the corresponding fs/ps CARS spectra along a 1-D probe volume.

Secondly, the CARS spectral simulation code has been improved by refining and expanding the collisional linewidth model, specifically the Modified Exponential Gap (MEG) model. These enhancements were aimed to improve the accuracy of temperature and pressure measurements by incorporating essential collisional partners for N_2 and O_2 simulations. The MEG-PF (MEG-Power Fit) model has been introduced to accommodate N_2 - N_2 collisions across both low and high-temperature

regimes. Additionally, for collisions of O_2 - O_2 , N_2 - O_2 , and N_2 - H_2 , MEG model parameters were determined through optimization using a various experimental measurements from literature to ensure higher accuracy across a wide range of temperatures. This effort increases the accuracy of the modeled linewidths included in the CARS spectral simulations, establishing a more reliable foundation for the investigation of pressure-sensitivity of ro-vibrational hybrid CARS spectroscopy.

Thirdly, this study included an experimental investigation of Q-branch CARS response at elevated pressures in gas mixtures involving N_2 , O_2 , CO_2 , and CH_4 in a static pressure cell. The experimental spectra of N_2 - O_2 were systematically examined at controlled concentrations and pressures ranging from 1–11 bar. Notably, a new method that consists of scaling late probe delay spectra by early probe delay spectra was employed to mitigate variability in excitation intensity, bandwidth, and shot-to-shot fluctuations. Moreover, this introduced method enables a pressure measurement with minimal uncertainty without quantifying gas composition. The effectiveness of this method was investigated through simulations and validated by experimental findings in binary N_2 - O_2 mixtures. Additionally, N_2 - CH_4 and N_2 - CO_2 mixtures were experimentally investigated. The ratio of CO_2 's ν_+ and N_2 in a N_2 - CO_2 mixture and the ratio of N_2 and CH_4 in a N_2 - CH_4 mixture show a power-law pressure dependence. Furthermore, the ratio of the CO_2 Fermi dyads exhibits a linear response over the range of pressures investigated, showing promise for pressure quantification over a large range. These outcomes offer a foundation for further application in more complex scenarios, such as high-speed and reacting flow environments.

The development of fs/ps vibrational CARS as a pressure measurement technique highlights several crucial areas that demand further investigation. These include extending the repetition rate beyond 1 kHz, a critical step to enhance the technique's utility in monitoring thermo-acoustic instabilities. Furthermore, there is a pressing need to increase probe power to enable 1D measurements while simultaneously narrowing the bandwidth, as narrower probes demonstrate a slower decrease in the relative O_2/N_2 signal, thereby effectively expanding the pressure sensitivity range at a fixed probe delay. Also, other species pairs should be investigated to find a more pronounced relative variation in spectral response with increasing pressure, enabling measurements within the operational ranges observed in modern gas turbine engines (up to 50 bar). Using other species for pressure tracking to enhance the dynamic range and applicability of this technique will require impulsive excitation of many species simultaneously using a broadband source such as a broadband super-continuum (example simulation shown in Fig. 5.1) generated by pumping a gas-filled hollow-core fiber with a fs-duration pulse.

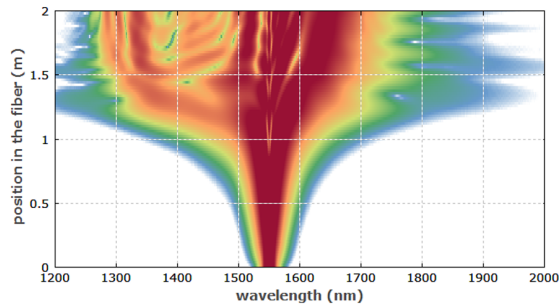


Figure 5.1: Evolution of the optical spectrum along a Hollow-Core Fiber pumped with an input fs pulse centered at $\lambda = 1550$ nm (From Dr. Paschotta, RP Photonics AG [11])

5.2 Future Work

Additionally, to quantify gas pressure in a fluctuating combustion environment, a dual-probe hybrid fs/ps CARS system must be developed. Overcoming the challenge of generating two collimated probes with a Raman-shifting crystal, as illustrated in Fig. 5.2, is necessary. Initial work demonstrated a large beam divergence for the light exiting the Raman shifting crystal. While employing a SHG crystal offers a potential solution, it introduces the complication of generating CARS signal at UV wavelengths, creating further alignment and implementation difficulties. Employing USED-CARS instead of BOXCARS phase-matching should be considered.

Once the obstacle of producing high-energy, coherent, two-color probe pulses is surmounted, the characterization of the probe designated for pressure measurement is necessary. This step is crucial to minimize uncertainties in predicting the I_{O_2}/I_{N_2} Q-branch CARS response with pressure, as demonstrated in Chapter 4. Multi-color probe pulse generation enables spectrally-isolated CARS signal generation for each probe delay, facilitating simultaneous measurements of species, temperature and pressure. The early probe delay may be used for temperature and species measurements, while the delayed probe may be used for quantifying

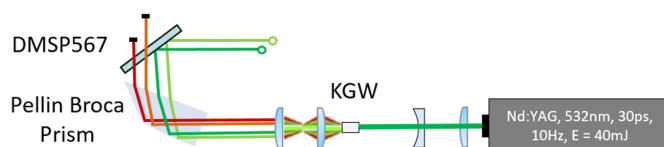


Figure 5.2: Preliminary Multi-Probe Generation Experimental Setup

pressure. Implementation of this approach is achievable with a single spectrometer/camera, as vibrational CARS signal from various molecules are well-separated in frequency.

Finally, the fs/ps CARS model must be expanded to include additional species for quantifying species and pressure in combustion systems. The inclusion of CO_2 and H_2 could significantly enhance the applicability of this method in real combustion scenarios, where CO_2/CO_2 , N_2/CO_2 and N_2/H_2 relative CARS intensities can be leveraged to quantify pressure.

The results reported in this thesis as well as the necessary future work outlined here will enable the simultaneous measurement of species, local pressure, and temperature in compressible reacting flows and practical high-pressure combustors. This measurement will further understanding of combustion at high pressures and highly compressible flow conditions to enable the design of efficient and effective power and propulsion systems and high-speed vehicles.

Bibliography

- [1] Dassault Aviation SA. Mirage iii: Origins, characteristics and performance data, 2023. <https://www.dassault-aviation.com/en/passion/aircraft/military-dassault-aircraft/mirage-iii/>.
- [2] Robert S Tranter, Kenneth Brezinsky, and D Fulle. Design of a high-pressure single pulse shock tube for chemical kinetic investigations. *Review of Scientific Instruments*, 72(7):3046–3054, 2001.
- [3] Doug Jackson. Pressure sensitive paint based on a paper originally written by doug jackson, Fall 1999. <https://aerospaceweb.org/design/psp/>.
- [4] Ulrich Doll, Eike Burow, Guido Stockhausen, and Christian Willert. Methods to improve pressure, temperature and velocity accuracies of filtered rayleigh scattering measurements in gaseous flows. *Measurement Science and Technology*, 27(12):125204, 2016.
- [5] AY Chang, BE Battles, and RK Hanson. Simultaneous measurements of velocity, temperature, and pressure using rapid cw wavelength-modulation laser-induced fluorescence of oh. *Optics Letters*, 15(12):706–708, 1990.
- [6] Zhengyong Li, Changrui Liao, Yiping Wang, Lei Xu, Dongning Wang, Xiaopeng Dong, Shen Liu, Qiao Wang, Kaiming Yang, and Jiangtao Zhou. Highly-sensitive gas pressure sensor using twin-core fiber based in-line mach-zehnder interferometer. *Optics express*, 23(5):6673–6678, 2015.
- [7] Karl Jousten, Gerardo Padilla-Viquez, and Thomas Bock. Investigation of tunable diode laser absorption spectroscopy for its application as primary standard for partial pressure measurements. In *Journal of Physics: Conference Series*, volume 100, page 092005. IOP Publishing, 2008.
- [8] Mark A Woodmansee, Robert P Lucht, and J Craig Dutton. Development of high-resolution n 2 coherent anti-stokes raman scattering for measuring pressure, temperature, and density in high-speed gas flows. *Applied Optics*, 39(33):6243–6256, 2000.

- [9] Sean P Kearney and Paul M Danehy. Pressure measurements using hybrid femtosecond/picosecond rotational coherent anti-stokes raman scattering. *Optics letters*, 40(17):4082–4085, 2015.
- [10] Chloe Dedic, Andrew D Cutler, and Paul M Danehy. Characterization of supersonic flows using hybrid fs/ps cars. In *AIAA Scitech 2019 Forum*, page 1085, 2019.
- [11] Rüdiger Paschotta. The software rp fiber power: Supercontinuum generation, Oct 2023.
- [12] Brian Dunbar. *NASA dryden fact sheets: X-15 hypersonic research program*, Aug 2015.
- [13] Wendell H. Stillwell. *X-15 Research Results With a Selected Bibliography*, chapter Chapter 5: Aerodynamic Characteristics of Supersonic-Hypersonic Flight. NASA Scientific and Technical Information Division, Washington, D.C, 1965.
- [14] Nettie Roozeboom, Jennifer K Baerny, David D Murakami, Christina Ngo, and Jessica M Powell. Recent developments in nasa’s unsteady pressure-sensitive paint capability. In *AIAA Scitech 2020 Forum*, page 0516, 2020.
- [15] Lucy Tang, Lawrence Hand, David Murakami, Nettie Roozeboom, and Marc Shaw-Lecerf. Unsteady pressure-sensitive-paint shot noise reduction. In *AIAA AVIATION 2021 FORUM*, page 2579, 2021.
- [16] Martin Boguszko and Gregory S Elliott. On the use of filtered rayleigh scattering for measurements in compressible flows and thermal fields. *Experiments in Fluids*, 38:33–49, 2005.
- [17] Ulrich Doll, Guido Stockhausen, and Christian Willert. Pressure, temperature, and three-component velocity fields by filtered rayleigh scattering velocimetry. *Optics letters*, 42(19):3773–3776, 2017.
- [18] Qingxu Yu and Xinlei Zhou. Pressure sensor based on the fiber-optic extrinsic fabry-perot interferometer. *Photonic Sensors*, 1:72–83, 2011.
- [19] Alan C Eckbreth, Gregory M Dobbs, John H Stufflebeam, and Peter A Tellex. Cars temperature and species measurements in augmented jet engine exhausts. *Applied Optics*, 23(9):1328–1339, 1984.

- [20] Paul M Danehy, James R Gord, Frédéric Grisch, Dmitry Klimenko, and Walter Clauss. Cars temperature and species measurements for air vehicle propulsion systems. In *RTO/AVT-124 Specialists Meeting on Recent Developments in Non-Intrusive Measurement Technology for Military Application on Model- and Full-Scale Vehicles*, number RTO-MP-AVT-124-Paper 5, 2005.
- [21] Sarah Tedder, Sean O’Byrne, Paul Danehy, and Andrew Cutler. Cars temperature and species concentration measurements in a supersonic combustor with normal injection. In *43rd AIAA Aerospace Sciences Meeting and Exhibit*, page 616, 2005.
- [22] Robert E Foglesong, Stephen M Green, Robert P Lucht, and J Craig Dutton. Dual-pump coherent anti-stokes raman scattering for simultaneous pressure/temperature measurement. *AIAA journal*, 36(2):234–240, 1998.
- [23] Luca Cantu, Emanuela Gallo, Andrew D Cutler, and Paul M Danehy. Dual-pump cars of air in a heated pressure vessel up to 55 bar and 1300 k. In *52nd Aerospace Sciences Meeting*, page 1098, 2014.
- [24] Sukesh Roy, Terrence R Meyer, and James R Gord. Time-resolved dynamics of resonant and nonresonant broadband picosecond coherent anti-stokes raman scattering signals. *Applied Physics Letters*, 87(26), 2005.
- [25] Alan C Eckbreth and Torger J Anderson. Dual broadband cars for simultaneous, multiple species measurements. *Applied optics*, 24(16):2731–2736, 1985.
- [26] Sukesh Roy, Terrence R Meyer, Robert P Lucht, Vincent M Belovich, Edwin Corporan, and James R Gord. Temperature and co₂ concentration measurements in the exhaust stream of a liquid-fueled combustor using dual-pump coherent anti-stokes raman scattering (cars) spectroscopy. *Combustion and Flame*, 138(3):273–284, 2004.
- [27] Chloe E Dedic and James B Michael. Thermalization dynamics in a pulsed microwave plasma-enhanced laminar flame. *Combustion and Flame*, 227:322–334, 2021.
- [28] Jonathan E. Retter, Matthew Koll, Chloe E. Dedic, Paul M. Danehy, Daniel R. Richardson, and Sean P. Kearney. Hybrid time–frequency domain

- dual-probe coherent anti-stokes raman scattering for simultaneous temperature and pressure measurements in compressible flows via spectral fitting. *Applied Optics*, 62(1):50–62, Jan 2023.
- [29] Daniel R Richardson, Sean P Kearney, and Daniel R Guildenbecher. Post-detonation fireball thermometry via femtosecond-picosecond coherent anti-stokes raman scattering (cars). *Proceedings of the Combustion Institute*, 38(1):1657–1664, 2021.
- [30] Sascha R Engel, Joseph D Miller, Chloe E Dedic, Thomas Seeger, Alfred Leipertz, and Terrence R Meyer. Hybrid femtosecond/picosecond coherent anti-stokes raman scattering for high-speed CH_4/N_2 measurements in binary gas mixtures. *Journal of Raman Spectroscopy*, 44(10):1336–1343, 2013.
- [31] Sean P Kearney and Daniel J Scoglietti. Hybrid femtosecond/picosecond rotational coherent anti-stokes raman scattering at flame temperatures using a second-harmonic bandwidth-compressed probe. *Optics Letters*, 38(6):833–835, 2013.
- [32] Alan C. Eckbreth. *Laser Diagnostics for Combustion Temperature and Species*. CRC press, London (UK), 1996.
- [33] David Escofet-Martin, Anthony O Ojo, Joshua Collins, Nils Torge Mecker, Mark Linne, and Brian Peterson. Dual-probe 1d hybrid fs/ps rotational cars for simultaneous single-shot temperature, pressure, and O_2/N_2 measurements. *Optics Letters*, 45(17):4758–4761, 2020.
- [34] Chloe Elizabeth Dedic. *Hybrid fs/ps coherent anti-Stokes Raman scattering for multiparameter measurements of combustion and nonequilibrium*. PhD thesis, Iowa State University, 2017.
- [35] Hans U Stauffer, Joseph D Miller, Mikhail N Slipchenko, Terrence R Meyer, Benjamin D Prince, Sukesh Roy, and James R Gord. Time-and frequency-dependent model of time-resolved coherent anti-stokes raman scattering (cars) with a picosecond-duration probe pulse. *The Journal of Chemical Physics*, 140(2), 2014.
- [36] Robert J Hall. Coherent anti-stokes raman spectroscopic modeling for combustion diagnostics. *Optical Engineering*, 22(3):322–329, 1983.

- [37] DA Greenhalgh, FM Porter, and SA Barton. A polynomial energy-gap model for molecular linewidths. *Journal of Quantitative Spectroscopy and Radiative Transfer*, 34(1):95–99, 1985.
- [38] B Lavorel, G Millot, J Bonamy, and D Robert. Study of rotational relaxation fitting laws from calculations of srs n2 q-branch. *Chemical physics*, 115(1):69–78, 1987.
- [39] Robert J Hall, James F Verdieck, and Alan C Eckbreth. Pressure-induced narrowing of the cars spectrum of n2. *Optics Communications*, 35(1):69–75, 1980.
- [40] JC Polanyi and KB Woodall. Mechanism of rotational relaxation. *The Journal of Chemical Physics*, 56(4):1563–1572, 1972.
- [41] LA Rahn and Rt E Palmer. Studies of nitrogen self-broadening at high temperature with inverse raman spectroscopy. *JOSA B*, 3(9):1164–1169, 1986.
- [42] B Lavorel, L Guillot, J Bonamy, and D Robert. Collisional raman linewidths of nitrogen at high temperature (1700–2400 k). *Optics letters*, 20(10):1189–1191, 1995.
- [43] Thomas Seeger and Alfred Leipertz. Experimental comparison of single-shot broadband vibrational and dual-broadband pure rotational coherent anti-stokes raman scattering in hot air. *Applied Optics*, 35(15):2665–2671, 1996.
- [44] Mark Linne, Nils T Mecker, Christopher J Kliewer, David Escofet-Martin, and Brian Peterson. Revisiting n2-n2 collisional linewidth models for s-branch rotational raman scattering. *Combustion and Flame*, 243:111928, 2022.
- [45] Joakim Bood, Per-Erik Bengtsson, and Thomas Dreier. Rotational coherent anti-stokes raman spectroscopy (cars) in nitrogen at high pressures (0.1–44 mpa): experimental and modelling results. *Journal of Raman Spectroscopy*, 31(8-9):703–710, 2000.
- [46] Timothy W Haller and Philip L Varghese. Measurements of pressure broadening of n2 in the anisotropic tensor component of spontaneous raman spectra. *Combustion and Flame*, 224:166–176, 2020.
- [47] Timothy A Brunner and David Pritchard. Fitting laws for rotationally inelastic collisions. *Advances in Chemical Physics*, pages 589–641, 1982.

- [48] ML Koszykowski, RL Farrow, and RE Palmer. Calculation of collisionally narrowed coherent anti-stokes raman spectroscopy spectra. *Optics letters*, 10(10):478–480, 1985.
- [49] T Seeger, F Beyrau, A Bräuer, and A Leipertz. High-pressure pure rotational cars: comparison of temperature measurements with o₂, n₂ and synthetic air. *Journal of Raman Spectroscopy*, 34(12):932–939, 2003.
- [50] Lars Martinsson, Per-Erik Bengtsson, Marcus Aldén, Stefan Kröll, and Jeanine Bonamy. A test of different rotational raman linewidth models: Accuracy of rotational coherent anti-stokes raman scattering thermometry in nitrogen from 295 to 1850 k. *The Journal of chemical physics*, 99(4):2466–2477, 1993.
- [51] Mikael Afzelius, P-E Bengtsson, Joakim Bood, Jeanine Bonamy, Frédéric Chaussard, H Berger, and T Dreier. Dual-broadband rotational cars modelling of nitrogen at pressures up to 9 mpa. ii. rotational raman line widths. *Applied Physics B*, 75:771–778, 2002.
- [52] Christian Meißner, Jonas I Hölzer, and Thomas Seeger. Determination of n₂-n₂ and n₂-o₂ s-branch raman linewidths using time-resolved picosecond pure rotational coherent anti-stokes raman scattering. *Applied Optics*, 58(10):C47–C54, 2019.
- [53] Yi Gao, Alexis Bohlin, Thomas Seeger, Per-Erik Bengtsson, and Christopher J Kliewer. In situ determination of n₂ broadening coefficients in flames for rotational cars thermometry. *Proceedings of the Combustion Institute*, 34(2):3637–3644, 2013.
- [54] CJ Kliewer, BD Patterson, P-E Bengtsson, and TB Settersten. Time-domain measurements of s-branch n₂-n₂ raman linewidths using picosecond pure rotational coherent anti-stokes raman spectroscopy. *Applied Physics B*, 108:419–426, 2012.
- [55] Joseph D Miller, Sukesh Roy, James R Gord, and Terrence R Meyer. Communication: Time-domain measurement of high-pressure n₂ and o₂ self-broadened linewidths using hybrid femtosecond/picosecond coherent anti-stokes raman scattering. *The Journal of chemical physics*, 135(20), 2011.
- [56] Thomas Seeger, Johannes Kiefer, Alfred Leipertz, Brian D Patterson, Christopher J Kliewer, and Thomas B Settersten. Picosecond time-resolved pure-

- rotational coherent anti-stokes raman spectroscopy for n₂ thermometry. *Optics letters*, 34(23):3755–3757, 2009.
- [57] Waruna D Kulatilaka, Paul S Hsu, Hans U Stauffer, James R Gord, and Sukesh Roy. Direct measurement of rotationally resolved h₂ q-branch raman coherence lifetimes using time-resolved picosecond coherent anti-stokes raman scattering. *Applied Physics Letters*, 97(8):081112, 2010.
- [58] Tasoltan T Basiev, Alexander A Sobol, Petr G Zverev, Vyacheslav V Osiko, and Richard C Powell. Comparative spontaneous raman spectroscopy of crystals for raman lasers. *Applied Optics*, 38(3):594–598, 1999.
- [59] Pavel Cerný, Helena Jelinková, Peter G Zverev, and Tasoltan T Basiev. Solid state lasers with raman frequency conversion. *Progress in Quantum Electronics*, 28(2):113–143, 2004.
- [60] Donald W Marquardt. An algorithm for least-squares estimation of nonlinear parameters. *Journal of the society for Industrial and Applied Mathematics*, 11(2):431–441, 1963.
- [61] J Bonamy, D Robert, JM Hartmann, ML Gonze, R Saint-Loup, and H Berger. Line broadening, line shifting, and line coupling effects on n₂-h₂o stimulated raman spectra. *The Journal of chemical physics*, 91(10):5916–5925, 1989.
- [62] ML Koszykowski, LA Rahn, RE Palmer, and ME Coltrin. Theoretical and experimental studies of high-resolution inverse raman spectra of molecular nitrogen at 1-10 atm. *Journal of Physical Chemistry*, 91(1):41–46, 1987.
- [63] T Dreier, G Schiff, and AA Suvernev. Collisional effects in q branch coherent anti-stokes raman spectra of n₂ and o₂ at high pressure and high temperature. *The Journal of chemical physics*, 100(9):6275–6289, 1994.
- [64] F Beyrau, A Datta, T Seeger, and A Leipertz. Dual-pump cars for the simultaneous detection of n₂, o₂ and co in ch₄ flames. *Journal of Raman Spectroscopy*, 33(11-12):919–924, 2002.
- [65] Timothy Y Chen, Christopher J Kliewer, Benjamin M Goldberg, Egemen Kolemen, and Yiguang Ju. Time-domain modelling and thermometry of the ch₄ ν_1 q-branch using hybrid femtosecond/picosecond coherent anti-stokes raman scattering. *Combustion and Flame*, 224:183–195, 2021.

- [66] GO Sitz and RL Farrow. Pump-probe measurements of state-to-state rotational energy transfer rates in n_2 ($v=1$). *The Journal of chemical physics*, 93(11):7883–7893, 1990.
- [67] Jonathan E Retter, Matthew Koll, Daniel R Richardson, and Sean P Kearney. Time-domain self-broadened and air-broadened nitrogen s-branch raman linewidths at 80–200 k recorded in an underexpanded jet. *The Journal of Chemical Physics*, 156(19), 2022.
- [68] B Lavorel, L Guillot, J Bonamy, and D Robert. Collisional raman linewidths of nitrogen at high temperature (1700–2400 k). *Optics letters*, 20(10):1189–1191, 1995.
- [69] KS Jammu, GE St John, and HL Welsh. Pressure broadening of the rotational raman lines of some simple gases. *Canadian Journal of Physics*, 44(4):797–814, 1966.
- [70] M Bérard, P Lallemand, JP Cebe, and M Giraud. Experimental and theoretical analysis of the temperature dependence of rotational raman linewidths of oxygen. *The Journal of Chemical Physics*, 78(2):672–687, 1983.
- [71] Emil Nordström, Ali Hosseinnia, Christian Brackmann, Joakim Bood, and Per-Erik Bengtsson. Raman linewidth measurements using time-resolved hybrid picosecond/nanosecond rotational cars. *Optics letters*, 40(24):5718–5721, 2015.
- [72] Jonas I Hölzer, Christian Meißner, and Thomas Seeger. Improvement of the coherent model function for s-branch raman linewidth determination in oxygen. *Applied Optics*, 60(15):C76–C83, 2021.
- [73] Y Ouazzany, JP Boquillon, and B Lavorel. Study of collisional broadening in oxygen lines by high-resolution coherent anti-stokes raman spectroscopy. *Canadian journal of physics*, 65(12):1588–1593, 1987.
- [74] G Millot, R Saint-Loup, J Santos, R Chaux, H Berger, and J Bonamy. Collisional effects in the stimulated raman q branch of o_2 and o_2-n_2 . *The Journal of chemical physics*, 96(2):961–971, 1992.
- [75] Jonas I Hölzer, Christian Meißner, and Thomas Seeger. Oxygen rotational raman linewidth determination considering nonmonoexponential decoherence behavior. *Journal of Raman Spectroscopy*, 50(9):1260–1267, 2019.

- [76] Alexis Bohlin, Fredrik Vestin, Pierre Joubert, Jeanine Bonamy, and Per-Erik Bengtsson. Improvement of rotational cars thermometry in fuel-rich hydrocarbon flames by inclusion of n₂-h₂ raman line widths. *Journal of Raman Spectroscopy: An International Journal for Original Work in all Aspects of Raman Spectroscopy, Including Higher Order Processes, and also Brillouin and Rayleigh Scattering*, 40(7):788–794, 2009.
- [77] Alexis Bohlin, Emil Nordström, BD Patterson, P-E Bengtsson, and CJ Kliwer. Direct measurement of s-branch n₂-h₂ raman linewidths using time-resolved pure rotational coherent anti-stokes raman spectroscopy. *The Journal of Chemical Physics*, 137(7), 2012.
- [78] Pierre Joubert, Jeanine Bonamy, Laura Gomez, and Dionisio Bermejo. N₂ h₂ isotropic raman q-branch linewidths: an energy-corrected sudden scaling law. *Journal of Raman Spectroscopy: An International Journal for Original Work in all Aspects of Raman Spectroscopy, Including Higher Order Processes, and also Brillouin and Rayleigh Scattering*, 39(6):707–710, 2008.
- [79] Miguel Dhyne, Muriel Lepère, and P Joubert. Semiclassical line broadening calculations, using an ab initio potential energy surface, in q-branch and s-branch of n₂ perturbed by h₂. *Journal of Raman Spectroscopy*, 43(12):2008–2014, 2012.
- [80] L Gomez, D Bermejo, P Joubert, and J Bonamy. Theoretical and experimental analysis of n₂-h₂ stimulated raman spectra. *Molecular Physics*, 104(12):1869–1878, 2006.
- [81] Laura Gómez, Raúl Z Martínez, Dionisio Bermejo, Franck Thibault, Pierre Joubert, Béatrice Bussery-Honvault, and Jeanine Bonamy. Q-branch linewidths of n₂ perturbed by h₂: Experiments and quantum calculations from an ab initio potential. *The Journal of chemical physics*, 126(20), 2007.
- [82] Joseph D Miller, Chloe E Dedic, Sukesh Roy, James R Gord, and Terrence R Meyer. Interference-free gas-phase thermometry at elevated pressure using hybrid femtosecond/picosecond rotational coherent anti-stokes raman scattering. *Optics express*, 20(5):5003–5010, 2012.
- [83] Hans U Stauffer, Joseph D Miller, Mikhail N Slipchenko, Terrence R Meyer, Benjamin D Prince, Sukesh Roy, and James R Gord. Time- and frequency-dependent model of time-resolved coherent anti-Stokes Raman scattering

- (CARS) with a picosecond-duration probe pulse. *The Journal of Chemical Physics*, 140(2):024316, jan 2014.
- [84] Johannes Kiefer, Thomas Seeger, Susanne Steuer, Stephan Schorsch, Markus Christian Weigl, and Alfred Leipertz. Design and characterization of a raman-scattering-based sensor system for temporally resolved gas analysis and its application in a gas turbine power plant. *Measurement Science and Technology*, 19(8):085408, 2008.
- [85] Jeffrey I Levatter, Richard L Sandstrom, and Shao-Chi Lin. Raman cross sections measured by short-pulse laser scattering and photon counting. *Journal of Applied Physics*, 44(7):3273–3276, 1973.
- [86] Klöckner H.W. Schrötter, Heinz W. Raman spectroscopy of gases and liquids. *Laser Physics at the Limits*, 1979.
- [87] J Burris, TJ McGee, and W Heaps. Uv raman cross sections in nitrogen. *Applied spectroscopy*, 46(6):1076–1076, 1992.
- [88] Y Gu, Y Zhou, H Tang, EW Rothe, and GP Reck. Pressure dependence of vibrational raman scattering of narrow-band, 248-nm, laser light by h₂, n₂, o₂, co₂, ch₄, c₂h₆, and c₃h₈ as high as 97 bar. *Applied Physics B*, 71:865–871, 2000.
- [89] Enrico Fermi. Über den ramaneffekt des kohlendioxyds. *Zeitschrift für Physik*, 71(3-4):250–259, 1931.
- [90] B Lavorel, G Millot, R Saint-Loup, H Berger, L Bonamy, J Bonamy, and D Robert. Study of collisional effects on band shapes of the $\nu_1/2\nu_2$ fermi dyad in co₂ gas with stimulated raman spectroscopy. i. rotational and vibrational relaxation in the $2\nu_2$ band. *The Journal of Chemical Physics*, 93(4):2176–2184, 1990.